WEATHER & CLIMATE

JOURNAL OF THE METEOROLOGICAL SOCIETY OF NEW ZEALAND (INC.)

VOLUME 41 • ISSUE 1 • 2021

WEATHER & CLIMATE

JOURNAL OF THE METEOROLOGICAL SOCIETY OF NEW ZEALAND (INC.)

VOLUME 41 ● ISSUE 1 ● 2021

ISSN 0111-5499

Weather and Climate is the official journal of the Meteorological Society of New Zealand (Inc.). Any opinions, statements or recommendations expressed in this journal are those of the respective author(s) and do not necessarily reflect the views of the Meteorological Society of New Zealand (Inc.).

Contributions to Weather and Climate are welcome on any meteorological or climatological subject, but preference will be given to contributions related to New Zealand and/or the Southwest Pacific.

Submissions can be made via Scholastica at: https://weather-and-climate.scholasticahq.com/ or by emailing the editor at: nava.fedaeff@niwa.co.nz

Published: December 2021

EDITORS Nava Fedaeff & Petra Pearce

COVER IMAGE Egils Baumanis

"This photo was taken on the second day of getting my very first camera - June 15th, 2021.The place was on a road from Wanaka to Rob Roy Glacier. I was going there for a hike. This is one of the most stunning sceneries I have seen in my life."

THE METEOROLOGICAL SOCIETY OF NEW ZEALAND (INC.)

The Meteorological Society of New Zealand (Inc.) was inaugurated in October 1979. The objects of the Society are to encourage an interest in the atmosphere, the weather and the climate, particularly in the New Zealand and South Pacific regions. Membership is open to all those with an interest in the objects of the Society. Membership comprises both professionals and amateurs including meteorologists, climatologists, geographers, hydrologists, yachting and tramping enthusiasts, glider pilots, people involved in aviation and marine industries, agriculturalists, professional weather forecasters, ecologists, economists, farmers, engineers and weather observers.

Membership fees:

Ordinary members	$40.00
Student members	$20.00
Institutional members	$120.00
Overseas postage surcharge	$15.00

All members receive copies of Weather and Climate and the quarterly Newsletter (which includes details of significant weather events in the previous period).

Correspondence:
The Secretary
Meteorological Society of New Zealand
PO Box 6523, Marion Square, Wellington, 6141, New Zealand
Web site: https://www.metsoc.org.nz/

WEATHER & CLIMATE

JOURNAL OF THE METEOROLOGICAL SOCIETY OF NEW ZEALAND (INC.)

VOLUME 41 ● ISSUE 1 ● 2021

Synoptic weather regimes over Aotearoa New Zealand

J. Williams[1] and J.Renwick[2]

[1]NIWA-Taihoro Nukurangi, 301 Evans Bay Parade, Ākautangi, Hātaitai, Wellington, Aotearoa New Zealand
[2]School of Geography, Environment and Earth Sciences, Victoria University of Wellington - Te Herenga Waka, Kelburn, Wellington, Aotearoa New Zealand

Correspondence: jonny.williams@niwa.co.nz

Key words: synoptic, regimes, clustering, reanalysis, Python.

This paper is dedicated to the memory of Dr Brett Mullan and to his contribution to weather and climate research in Aotearoa New Zealand.

Abstract

This work provides an updated set of 12 dominant geopotential height fields over Aotearoa New Zealand defined using NCEP/NCAR reanalyses and provides an initial analysis of the same using a state of the art dataset with increased temporal and spatial resolution; ERA5. These regimes were initially produced by Kidson (2000) and have provided the basis for many other subsequent studies. These maps provide a guide to the prevailing weather due to the strong relationships between circulation patterns and surface climate in New Zealand. The results presented here using the NCEP/NCAR reanalysis are broadly in agreement with previous work but with some important differences. The most notable of these differences is the need to average two regimes together to provide good agreement between this work and Kidson (2000). These differences are attributed to differences in software used, improvements to the underlying dataset itself and to the 'mixing' of statistically indistinguishable empirical orthogonal functions in different linear combinations. Using ERA5 data results in sets of weather types which are analogous in some ways to previous work but with some important differences, especially over mountainous regions. Use of ERA5 noticeably improves the ratio of intra- to inter-regime variance; a measure of the 'quality' of the cluster analyses. All data and code used in this work is publicly accessible and it is hoped that this will provide a catalyst for open discussions on this topic, particularly with relation to future perturbations to these regimes under climate change. The mathematical methods used in this study are widely used in the New Zealand weather and climate community and it is hoped that this work will prove useful as a resource for future studies.

1. Introduction

The world's meteorology and climatology is extraordinarily complex in its spatio-temporal variability. Because of this, simplifications and methodologies for reducing and communicating this complexity are essential if we are to understand it better. Examples are many and various; e.g. the Beaufort scale in wind speed, rainfall probability in a weather forecast, cloud clustering in climate models (Williams and Webb 2009), classification of El Niño or La Niña (e.g. Trenberth 1997 for a review) and the ubiquitous quasi-static approximation.

Submitted: 19 April 2021
Accepted: 8 October 2021

Although these methodologies are of course hugely different in their scope, they all have one fundamental thing in common; that of the reduction in the complexity of a system such that it can be better understood by the relevant audience. This study is limited only to the region surrounding New Zealand and to one meteorological variable, the 1000hPa geopotential height, *z*. Initially we use the data at 0000 and 1200 UTC as in Kidson (2000) before moving on to using the ERA5 dataset's results at 0000, 0600, 1200 and 1800 UTC.

The literature contains several examples of synoptic classification methods over New Zealand in addition to the most well known example: the 12 'Kidson types', which form the basis of the first part of this study. For example, in Jiang et al. (2004) and Jiang (2011) the authors use obliquely rotated T-mode principal component analysis and convergent K-means clustering to find 10 and 12 dominant weather regimes respectively. These regimes are analogous to those found in Kidson (2000) - hereafter K2K - but, as the author states, are not 'one to one'. Indeed, this foreshadows the work presented here by noting that '*... the convergent K-means clustering (in Jiang et al. 2004) did not change the (K2K) cluster centroid locations significantly, but redistributed the memberships of daily maps to form compact clusters.*'

Other authors have used self-organising maps - SOMs - for example as in Jiang et al. (2013) and Gibson et al. (2016). It is beyond the scope of this work to give a detailed explanation of the SOM generation procedure, but in brief it is a machine learning technique which produces two-dimensional representations - i.e. maps - from a higher dimensional input dataset. The aim is to preserve the essential structure of the input data whilst allowing it to be more easily interpreted. In this qualitative respect it is therefore analogous to the 'PCA + K-means' clustering approach of K2K. However, a key difference in the approaches is that SOMs add a means of topology conservation whereby the cluster means dynamically adjust - i.e. 'self organise' - throughout the process (Sheridan and Lee 2011).

There are two main motivations for this work; firstly to provide a pedagogical primer for how the widely used 'PCA + K-means' method is implemented in practice, and secondly to apply the method to the ERA5 dataset (Hersbach et al., 2020). ERA5 has 10 times the grid resolution of NCEP/NCAR (0.25° versus 2.5°) in addition to increased temporal resolution and is thus capable of a far more detailed analysis. It is, however, advantageous to use the same methodology as K2K here since it provides traceability with many previous studies and is implemented in not more than a few 10s of lines of Python code using modern software packages. We note however that methods such as SOMs and other machine learning approaches - for example Saavedra-Moreno et al. (2015) - are more rigorous in their derivations and better able to represent extremes. It is important to state at this point however that is it not the intention of this work to recommend a particular methodology for regime classification.

We have deliberately chosen to use the same variable - 1000hPa geopotential height - and domain of interest for the ERA5 analysis to maintain commonality with K2K. Other authors use clustering metrics at 850hPa (Sheridan et al., 2008), 700hPa (Michelangeli et al., 1995) and 500hPa (Moore and Dixon 2015) in their analyses. The use of variables further away from the surface has the advantage that the synoptic-scale circulation is less impacted by surface features. This is just one example of a potential extension to this work which we hope to motivate. We are not advocating that this method is superior to other methods such as SOMs, however it does have the advantage of being widely known, particularly in the New Zealand community.

The dataset used in the first part of this work is identical to that used in K2K, which uses 28,852 fields of *z* between

January 1958 and June 1997 to define 12 dominant synoptic weather types. These are frequently referred to as 'Kidson types' in their wide use in modern- (Parsons et al. 2014) and paleo-climate (Ackerley et al. 2011) studies. Similar methods have also been used to study weather regimes in other parts of the world such as South America (Solman and Menéndez 2003).

The synoptic weather types found in K2K grouped the tens of thousands of input data points into 12 types. These are further split into 3 regimes; 'trough', 'zonal' and 'blocking'. Together, these regimes express the dominant weather types over New Zealand. This is because of New Zealand's topography and exposure to strong wind streams, resulting in strong statistical relationships between synoptic-scale flows and surface climate.

It should be noted that the second level classification of the clusters into the three larger 'trough', 'zonal' and 'blocking' types is, by its nature, subjective and in our analysis of the NCEP/NCAR dataset here, we use the same overarching terms purely to promote ease of comparison. When we move on to the calculation of new clusters for the ERA5 data, we choose to dispense with these terms altogether and simply order them by their areal mean height. This is found by calculating an area-weighted mean of the final height clusters.

This study gives a more detailed account of the derivation of these synoptic types than given previously and provides an update to the types' occurrences compared to K2K, which itself builds on many other previous studies (Kidson 1999, Kidson 1997, Kidson 1994a, Kidson 1994b, Kidson and Watterson 1995 and Ward 1963). The new results presented are broadly in agreement with those from K2K, however there are some notable differences.

The K2K methodology is widely cited, however the available details on the types' calculation are somewhat opaque, particularly to those readers less familiar with statistical analysis and clustering techniques. To aid future work, the code used is freely available and a step by step guide is given below for:

- How the weather types themselves are calculated from a reference dataset, in this case the NCEP/NCAR reanalysis.

- How to assign a particular synoptic type to a new observation or model output of z.

- How to interpret the meaning and derivation of the types from mathematical and geometrical arguments.

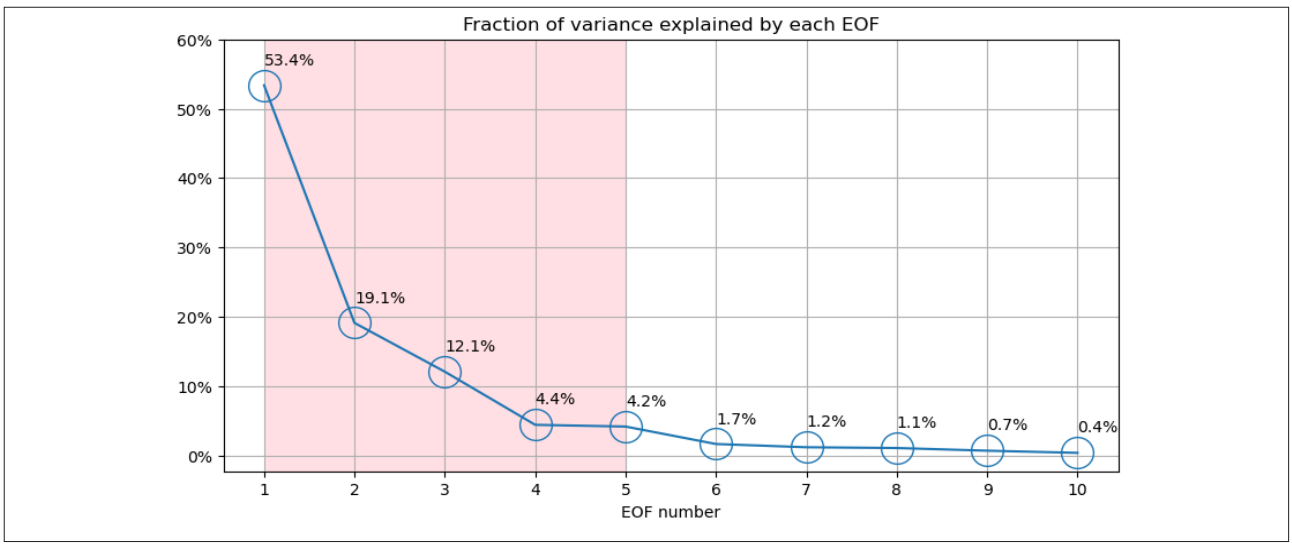

Figure 1: Fraction of variance explained by the first 5 EOFs in the time series of z_s. Although the first 10 EOFs are shown, only 5 are used in this analysis (shown by the shaded region).

2. Methodology

The most widely referenced work in the literature on this subject is K2K. This builds on earlier work (e.g. Kidson 1997 and Kidson 1994a) to construct 12 dominant synoptic weather regimes. This section gives a step-by-step guide to reproducing these weather types, i.e. Figure 2 in Kidson 2000 (and Figure 1 in Ackerley et al. 2011).

2.1 Data and software

We use the same input data as used in K2K, that is 1000hPa geopotential height data (z) from the NCEP/NCAR reanlysis (Kalnay et al. 1996) for January 1958 to June 1997 inclusive at 0000 and 1200 UTC.

We use the Python programming language exclusively for this work and make use of the open source eofs package (Dawson and Wales 2019, Dawson 2016) to calculate the principal components (PCs) and empirical orthogonal functions (EOFs). K-means clustering analysis is then carried out on the PCs to obtain the dominant weather regimes using the scikit-learn package (Pedregosa et al. 2011), which relies on NumPy (Harris et al. 2020) and SciPy (Virtanen et al. 2020) for its underlying operation and includes many more functions other than K-means clustering. A more detailed explanation of the mathematical basis of these packages and methods is beyond the scope of this paper.

2.2 Mathematical basis

Firstly, height anomalies are calculated by removing the time mean of the heights ($\overline{z}$):

$$z_s = z - \overline{z} \ . \tag{1}$$

Now the EOFs are calculated and the first 5 are retained. The fractions of variance explained by the first 5 EOFs are given in Figure 1 and together they account for 93.2% of the observed variability. The first 5 EOFs are shown in Figure 2. The cutoff of five EOFs was used for consistency with K2K.

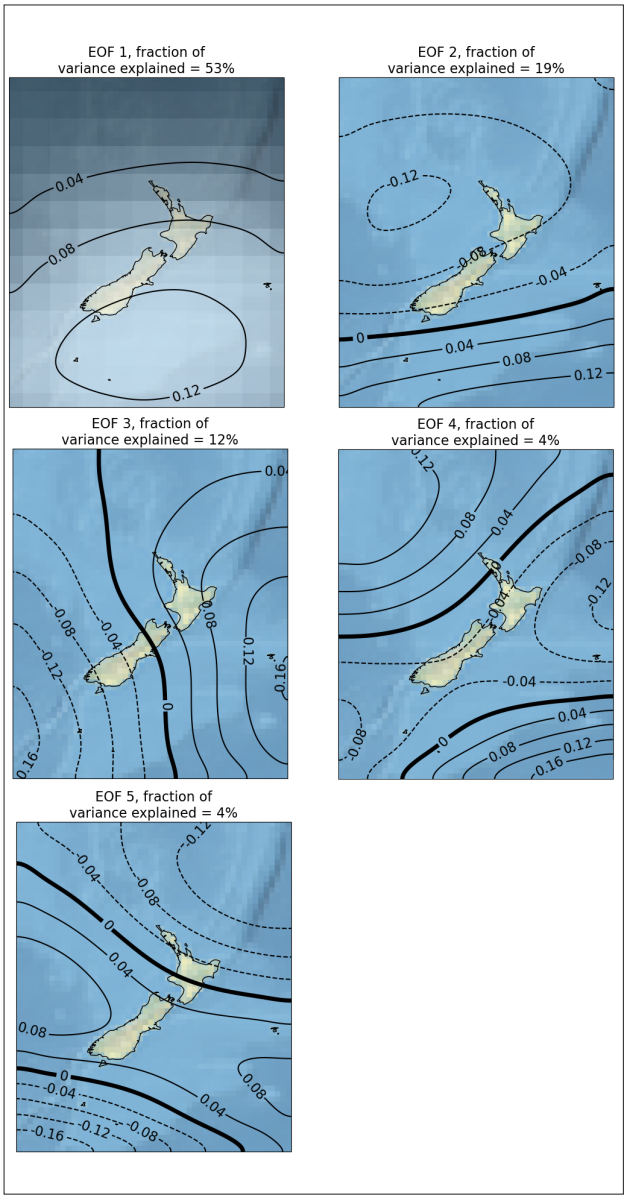

Figure 2: The first 5 EOFs, ε, of z_s. The contour lines are smoothed via linear interpolation between gridpoint values and the gridscale of the data used is shown in the subfigure for EOF 1. The background of the figures shows the local relief. The contour interval is 0.04 in all cases and varies from -0.16, to 0.16. The values are dimensionless. Positive contours are solid, negative contours are dashed and the zero line is thickened.

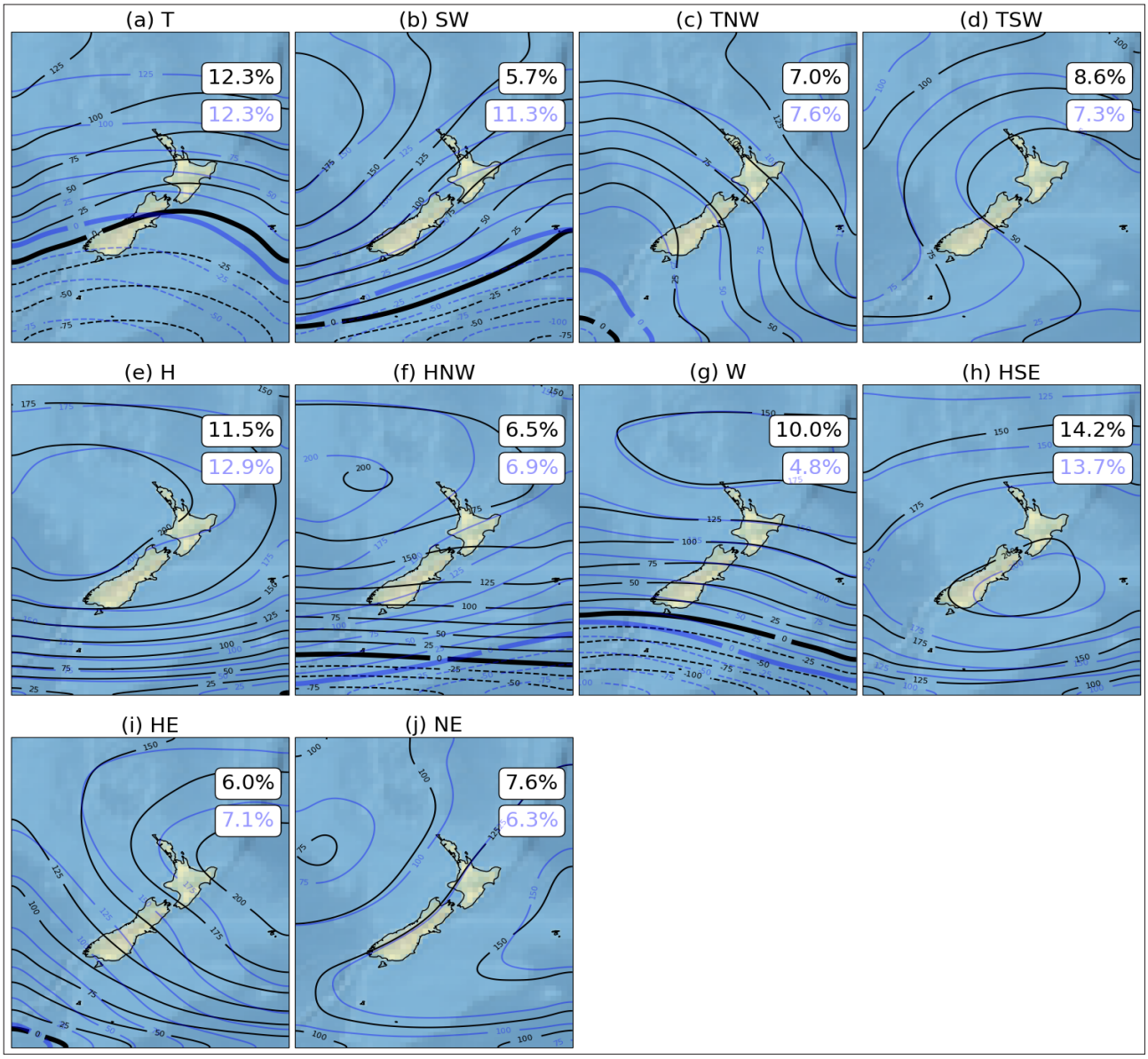

Figure 3: The 10 clusters which are deemed to be in close enough agreement with those of K2K to be assigned the same label (in black). Again the contour lines are smoothed and the original K2K clusters are shown in blue. The inset boxes show the fraction of time spent in each regime with the font colours matching the contour line colours. The background of the figures shows the local relief.

Next the PCs, P_n, are calculated, represening the amplitude of each EOF in a given height field. The fundamental operation here involves projecting the height field onto the EOFs and this is discussed further in the context of assigning regimes to arbitrary datasets in Appendix A. For the cluster analysis, the PCs are normalised to give:

$$\hat{P}_n$$

$$\hat{P}_n = \frac{(P_n - \overline{P_n})}{\sigma_{P_n}}, \qquad (2)$$

where σ_p is the standard deviation of P across time and $1 \leq n \leq 5$.

Now, the K-means clustering assigns each z_s field to one of 12 clusters. The K-means approach assigns the fields to an ever-reducing number of clusters, from an arbitrary starting point, to a final step of one cluster holding all observations. Our analysis has chosen to stop the clustering at 12 clusters, for consistency with K2K. This

order of these clusters is arbitrary and is chosen purely to match Kidson's original work. Once each z_s field has been assigned a value between 1 and 12, the final cluster means, C_z are the time mean of the z fields assigned to each cluster, that is,

$$C_{z,i} = \overline{z_i} \ , \tag{3}$$

where $1 \leq i \leq 12$.

The first 10 of these final clusters are shown in Figure 3, along with their equivalents from Kidson (2000). The associated winds from the same reanalysis product at the same twice daily sampling frequency are shown in Figure 4.

Although the agreement between the 2 analyses is generally good for the 10 clusters shown in Figure 3, the 2 remaining ones are not shown due to their pronounced differences with the HW and R blocking types from K2K. These differences are discussed in the next section.

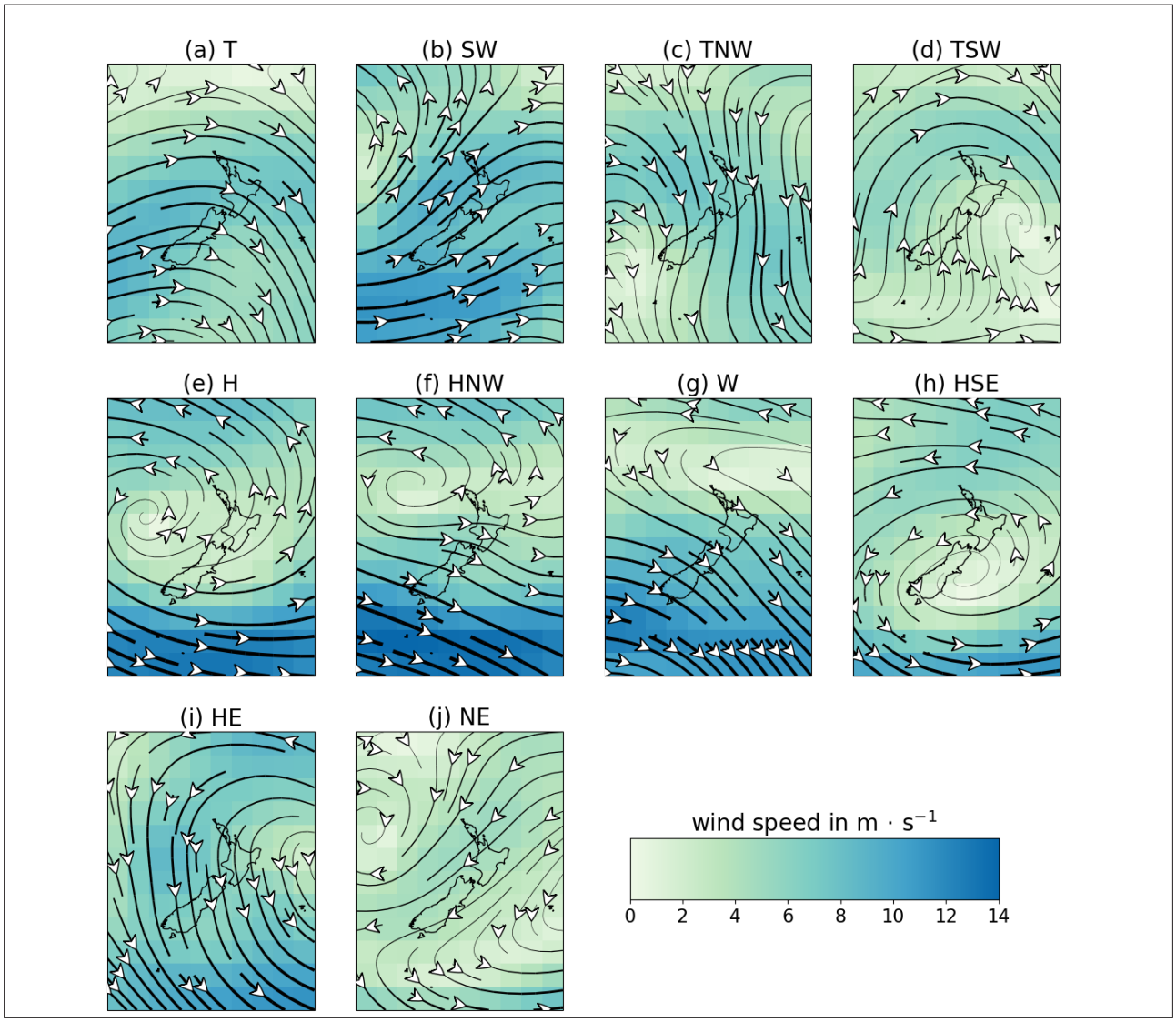

Figure 4: Wind streamlines and speeds (ms^{-1}) for the synoptic regimes shown in Figure 3. The colours show the windspeed at the gridscale. The thickness of the lines is proportional to the local speed and is consistent across subfigures.

3. How do the new synoptic types differ from Kidson's and why?

It is clear from Figure 3 that 10 of the synoptic types obtained here are generally in good agreement with those of K2K. That being said, the HNW regime is considerably more zonal in the new case, especially at southernmost latitudes. The SW regime from K2K is displaced north of the equivalent one from this analysis by approximately 100km and the opposite for W. This likely accounts for the factor of approximately 0.5 and 2 difference in occurrence frequency in the new case with respect to K2K.

There are however notable structural differences between the remaining two clusters obtained in this work and the HW and R blocking clusters in K2K. So much so in fact, that it is dubious to assign the same synoptic weather type in these cases. Figure 5 shows the HW and R blocking regimes from K2K along with the two remaining clusters from this work. The averages of the two remaining regimes are also shown.

The two new types shown in Figure 5 (a) and (b) are quite different to the HW and R regimes in K2K (Figure 5 (d) and (e)) yet their mean is strikingly similar, as is their combined fractional occurrence of 10.6% versus 10.1%.

As to why the new weather types found here are somewhat different to those of K2K, we have performed sensitivity analysis of the parameters used in the K-means clustering and have found the fractional occurrence of the regimes obtained here to be robust. For example, by default the K-means solver is run 10 times using different initial estimates and each of these estimates is iterated up to

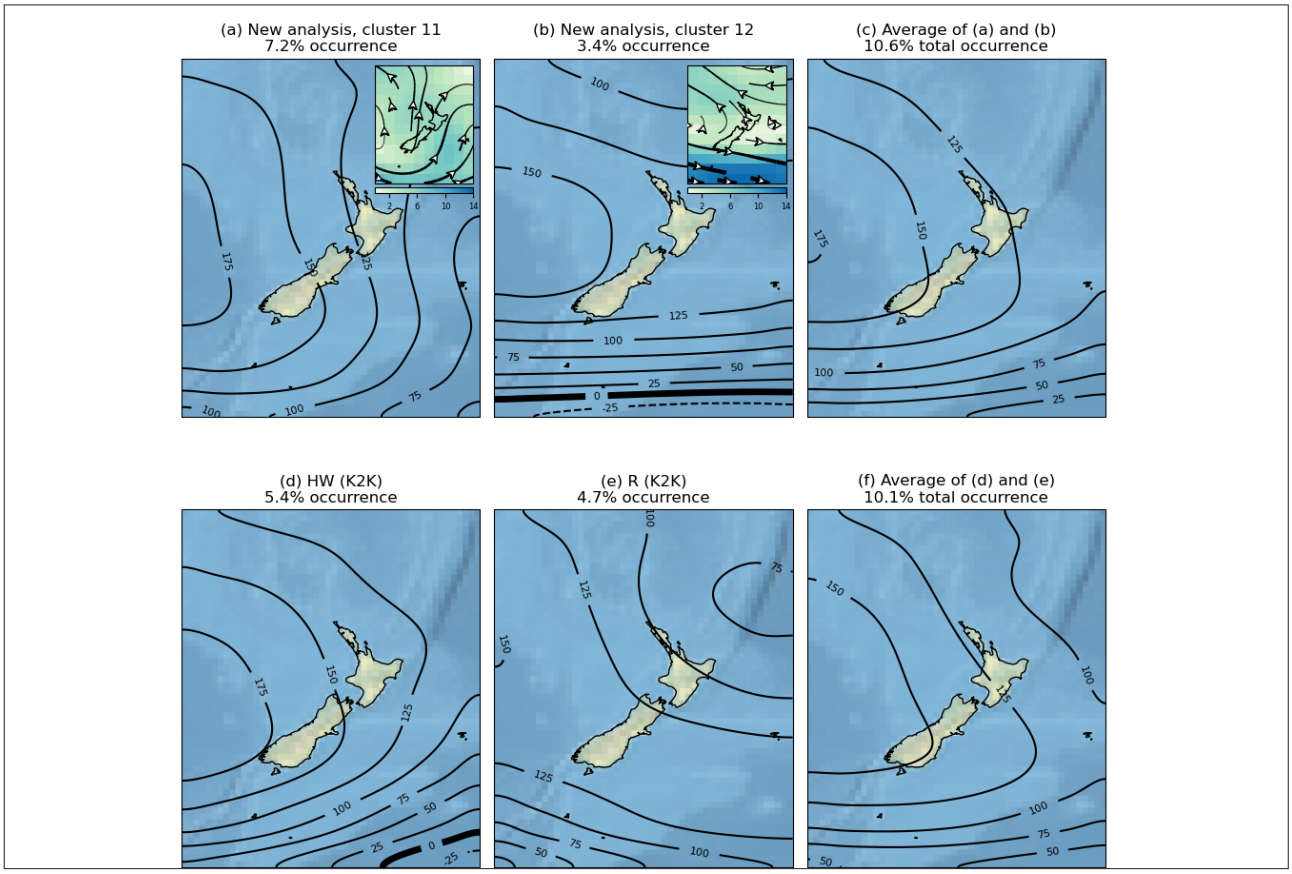

Figure 5: (a)-(b) The remaining two regimes from the new analysis which are not shown in Figure 3. Subfigures (a) and (b) also show the wind fields for the relevant cluster shown. The colour scale is the same as for Figure 4 and the horizontal density of the streamlines is halved to improve legibility. Subfigure (c) is the average of (a) and (b). (d)-(e) the HW and R regimes from K2K. Subfigure (f) shows the average of (d) and (e).

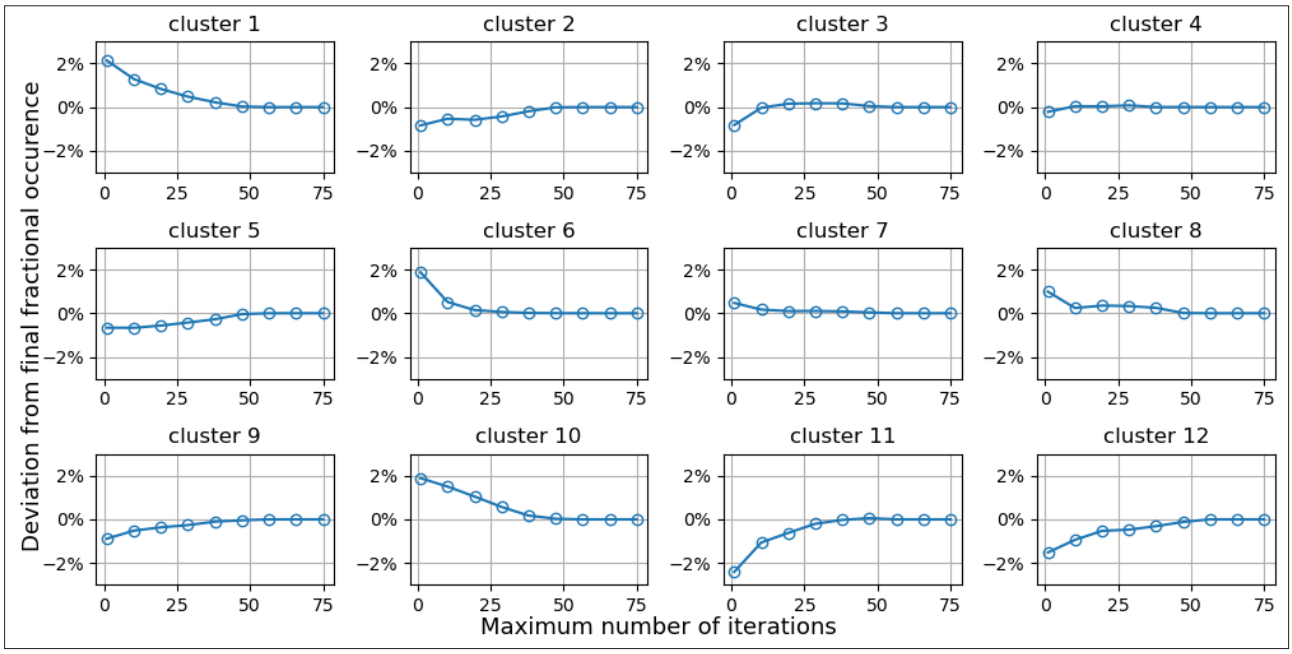

Figure 6: Deviation of the fractional occurrence of each regime as a function of the maximum number of iterations used in each pass of the K-means clustering algorithm. The largest difference is substantially smaller than the differences seen in Figure 3 (b) and (g) - which show the largest differences between the analyses - and therefore cannot account for the differences seen in the occurrence fractions.

300 times to ensure convergence. Figure 6 shows the relationship between the maximum number of iterations and the deviation of the final fractional occurrence of the regimes shown in Figures 3 and 5.

Figure 6 shows that the largest change in any of the cluster occurrences as the number of iterations is increased is approximately 2%. This therefore cannot account for the larger differences in the SW and W regimes found here compared to K2K (Figure 3 (b) and (g)). It is also possible that the dataset used in K2K was affected by the assimilation of incorrect pseudo-observations - or PAOBs - in early versions of the reanalysis (e.g. Kidson 1999).

It should also be acknowledged that no calculation is perfect and that different implementations of common algorithms will inevitably lead to some element of disagreement. This is noted in the documentation for the K-means software used here (Pedregosa et al., 2011): *"Given enough time, K-means will always converge, however this may be to a local minimum"*. For this reason - and also since the EOF/PCA methods are highly robust - we attribute the differences in the clusters obtained here predominantly to the K-means clustering method used. That said, the precise convergence criteria in K2K are not known (i.e. exacting details of the mathematical formalism or its application). Further discussion of cluster convergence is described in Michelangeli et al. (1995), using their concept of 'classifiability' indices.

The result shown in Figure 5 is reminiscent of the 'mixing' of EOFs or principal components subject to high sampling variability (e.g. Cheng et al., 1995). When the eigenvalues of consecutive EOFs are not statistically separate, different linear combinations of those EOFs can appear, as sample size changes. In this case, a similar thing seems to have occurred within the clustering algorithm and the definition of the cluster means.

At this stage, it is natural to ask if the new regimes obtained using ostensibly the same method are somehow more robust than those obtained in K2K. One way of doing this in a statistical fashion by comparing the ratio of intra- to inter-cluster variance in each of the analyses.

The intra-cluster variance for each cluster is calculated by calculating the variance through time at each gridpoint and then summing them. The inter-cluster variance is found in the same manner except that the dimension that the variance is calculated over is in 'cluster space' - i.e. over the 12 clusters - rather than in the time dimension. We then add the 12 intra-cluster variances together and divide by the inter-cluster variance to give one number for each analysis. By this method, the lower the ratio the better since decreased intra-cluster variance and increased inter-cluster variance indicate more 'distinct' clusters. Using this method, we find that the ratio in the new analysis is marginally 'better' than K2K but only by ≈ 0.4%; 8.74 for this analysis and 8.77 for K2K. Dividing by 12 to give these ratios on a 'per cluster' basis gives 0.728 and 0.731 respectively.

Although 10 of the 12 regimes found here are in close agreement with those from K2K - at least spatially - this is no guarantee that the two analyses put the same observations into the same category.

To investigate this further, it is instructive to construct a contingency table showing how the regimes assigned in K2K compare to those from this analysis. Figure 7 shows this table which compares the types assigned to every individual 12-hourly observation in the NCEP/NCAR dataset to the same classifications from this work.

Along with Figure 3 we can immediately see that simply because - for example - regime T occurs 12.3% of the time in both analyses, this is not because they both assign the same observations to the same cluster. In fact in this example we see that there are significant contributions to the T regime in this work from observations assigned to TSW, TNW and SW regimes in K2K.

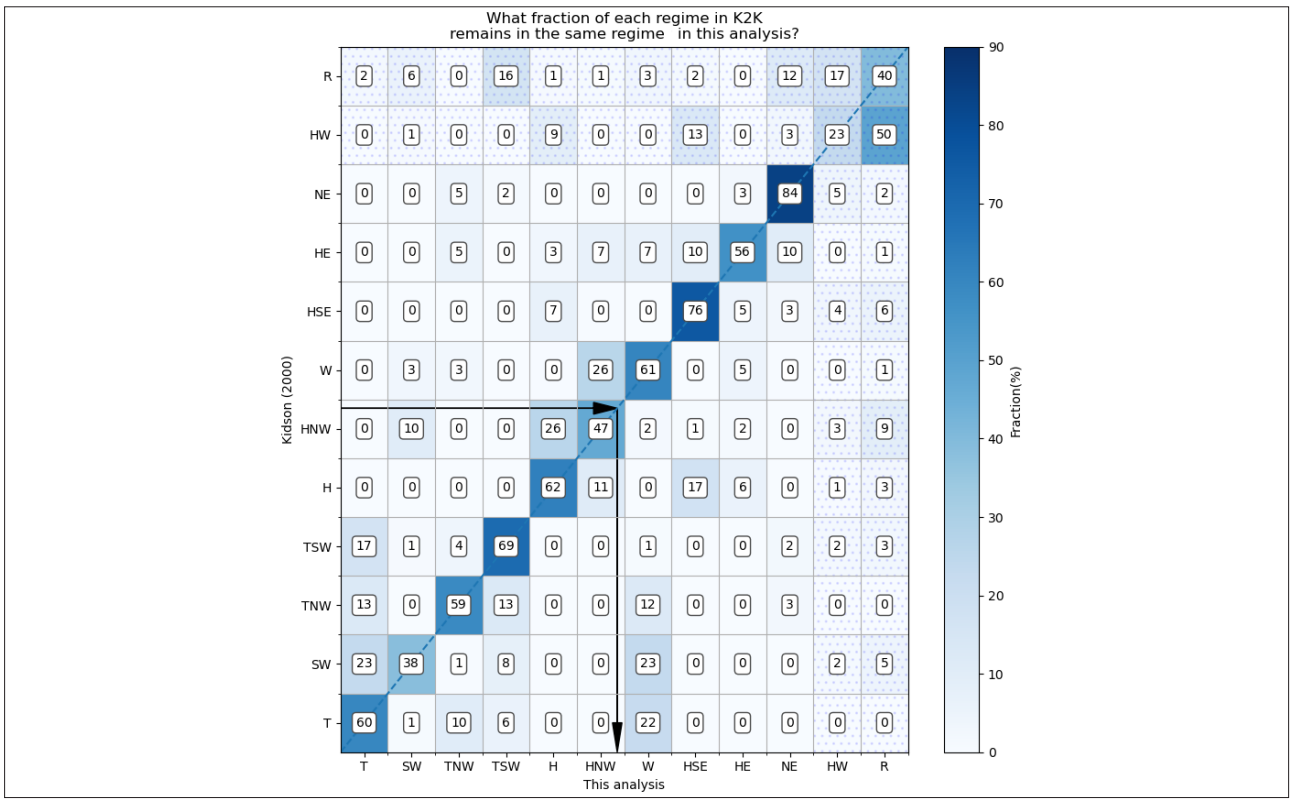

Figure 7: A contingency table showing the fraction of each regime in K2K which remains in the same regime in the new analysis, calculated on a point-by-point basis. The black arrows show - for example - that only 47% of the points in K2K which are assigned the HNW type, remain in this type in the new analysis. The hatching in the regions representing the HW and R regimes is to show the ambiguity in their assignment in this work; see Figure 5. Every row sums to 100% although this is not necessarily reflected in the integer values shown here due to rounding ambiguities.

4. New regimes using the ERA5 reanalysis

We now use the same method as described above but using the ERA5 reanalysis (Hersbach et al. 2020). The data is available hourly but in order to make the algorithms used here amenable to calculation on 1 processor in a time frame of ≈ 30 minutes, we have used 6-hourly data. At the time of writing, the ERA5 data is available from January 1979 and we use this data up until the end of 2014. The horizontal resolution is 0.25° compared to the 2.5° of the NCEP/NCAR data. Along with the doubling of time resolution used, this means that the overall number of points upon which to base this new analysis is 200 times greater than K2K.

Figure 8 shows the first five EOFs for the ERA5 dataset and is directly comparable with Figure 2 for NCEP/NCAR. There are some aspects to note immediately. Firstly, the broad structure of EOFs 1-3 on synoptic lengthscales is very similar to that given in Figure 2 for NCEP/NCAR. This is to be expected since the underlying physical state is the same, albeit represented by a different reanalysis scheme for different - but overlapping - time periods.

Secondly, compared to Figure 2, the 'order' of EOFs 4 and 5 has been reversed; broadly speaking EOF 4 for NCEP/NCAR has the same structure as EOF 5 for ERA5, and vice versa. This result illustrates the lack of statistical separation between EOFs 4 and 5.

Thirdly, the effect of the land is much more apparent, causing large local gradients and distortions in height contours. This is seen in all panels in Figure 8 but is particularly apparent for EOFs 3 and 4 as the zero contour crosses the Southern Alps and North Island Central Plateau respectively.

Figure 9 shows the 12 types obtained for the ERA5 dataset, ordered by their areal average mean geopotential height. There are some notable differences and similarities between the regimes in Figures 3, 5 and 9. For example Figure 3(j) and Figure 9(j) both show the same shape distinctive of the NE K2K-type, albeit with significant influence from the land in the latter - which is true for all of the new clusters. In addition the high pressure HSE type is seen in both analyses - Figures 3(h) and 9(l).

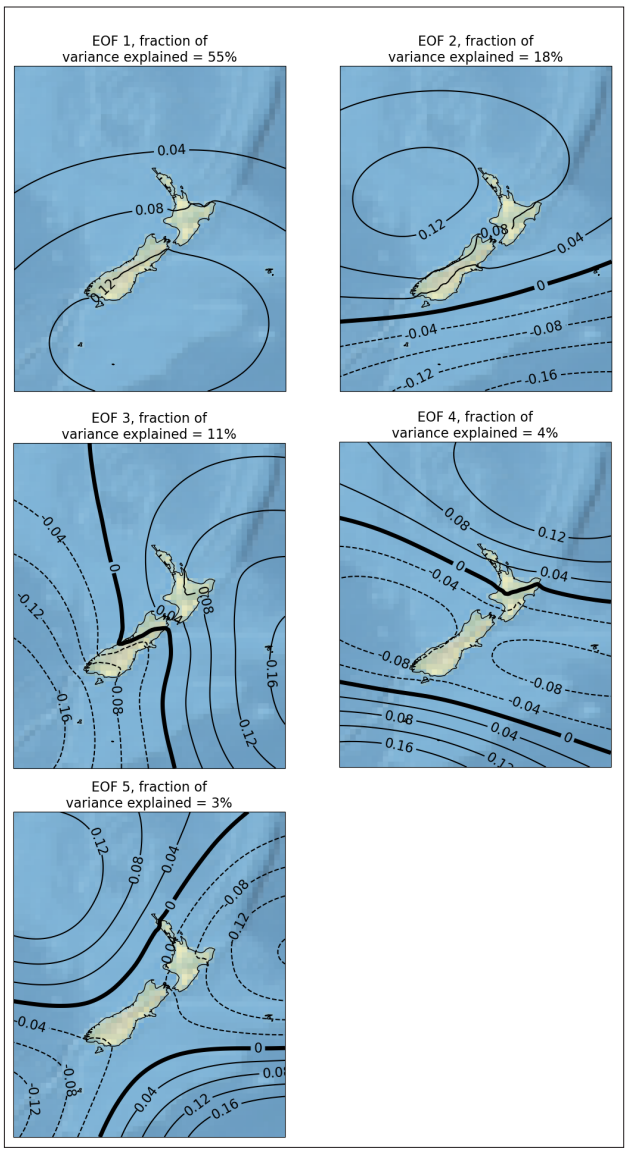

Figure 8: The first 5 EOFs, ε, of z_s for the ERA5 dataset. The contour lines are not smoothed in this case and the background of the figures shows the local relief. The EOFs are multiplied by 10 to aid comparison with Figure 2. This is due to the increase in the number of grid points and hence the total variance. The contour interval is 0.04 in all cases and varies from -0.16, to 0.16. The values are dimensionless. Positive contours are solid, negative contours are dashed and the zero line is thickened.

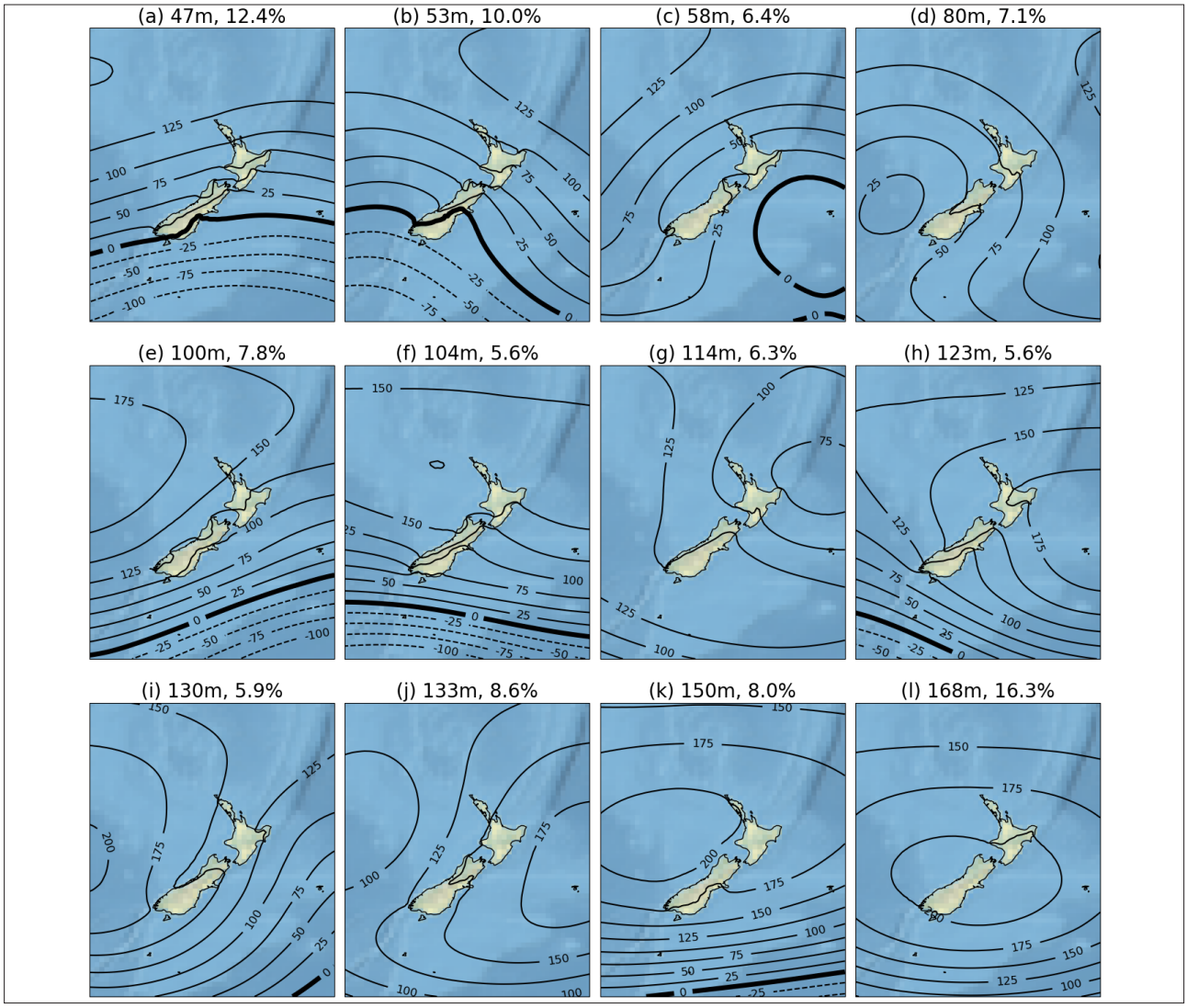

Figure 9: The 12 geopotential height clusters obtained for the ERA5 dataset. They are ordered from top left to bottom right by their areal mean geopotential height value. The frequency of occurrence for each regime is also given.

In contrast, some of the new ERA5 regimes do not have such a close analogue in K2K. For example, although Figure 9(g) is qualitatively similar to the R type in K2K, it has substantial local modifications.

Finally, revisiting the question of the ratio of intra- to inter-cluster variance for this new analysis, we find that using the 4-times-daily ERA5 data and 12 clusters gives an improvement in this ratio of ≈7% compared to the new NCEP/NCAR analysis. The individual values are 8.74 cf. 8.15 or - on a 'per cluster' basis - 0.728 cf. 0.679. This clearly illustrates the utility of using this improved dataset given the fact that the ratios for the two analyses of the NCEP/NCAR data were within ≈ 0.4% of one another and that we have only used 4 of the 24 available daily observations in ERA5.

It would be instructive in future work to construct a contingency table analogous to Figure 7 for the two reanalysis datasets used here and to examine our ERA5 results in the context of the recent study of Pohl et al., (2021).

5. Conclusions

In this work we have sought to provide not only a reassessment of dominant synoptic weather types over Aotearoa New Zealand from Kidson (2000), but also to provide an initial cluster analysis using the same methodology for a more recent dataset, ERA5. This product has significantly increased spatial and temporal resolution compared to NCEP/NCAR and indeed gives a substantially improved intra- to inter-regime variance ratio when 12 clusters are obtained. Widely-used peer-reviewed software packages in the Python programming language were used to calculate the EOFs and K-means clusters. Our results are broadly in line with K2K but with some notable differences. The key findings of this part of the work are:

- Although 10 of the 12 clusters identified in K2K are well reproduced in 'shape' in this work, 2 of the blocking regimes from K2K (HW and R) do not have recognisable analogues in the clusters found in this work. See Figure 3.

- Two of the regimes from K2K differ by factors of approximately 0.5 and 2 respectively with their spatially similar regimes from this work. This is accompanied by meridional shifts in the cluster mean height contours of about 100km in both cases, although in opposite directions.

- The average of the HW and R clusters from K2K is in striking agreement with the equivalent average of clusters 11 and 12 from this work, see Figure 5. This is attributed to different levels of EOF mixing in this work and in K2K and to subtle differences in the K-means clustering algorithms used in each case.

- Use of a contingency table for partitioning the results of this study and comparing them to those from Kidson 2000 shows that although some clusters are produced with very similar frequencies, this is not purely because the same observations are assigned the same type in the two analyses. Indeed for the T regime, even though both analyses show that this regime occurs 12.3% of the time, only 60% of the observations in this type in K2K are also assigned to this group in this work.

Our initial analysis of the clusters obtained from the ERA5 dataset show some interesting similarities and differences to previous work. Some of the dominant weather types identified in Kidson (2000) are very similar to those obtained in this new work, reflecting the overall synoptic dominance of some particular weather types, such as high pressure centred over Aotearoa New Zealand. There are however some types in the 12 cluster analysis which have some substantial local differences to those in K2K.

Future work will apply this methodology to differences in synoptic weather regimes over Aotearoa New Zealand in the UK Earth System Model (UKESM, e.g. Sellar et al. 2020) and in the NZESM (e.g. Behrens et al. 2020). This will be especially pertinent with regard to climate change and its effect on the dominant weather types that can be expected to occur in the future. It would also be of interest to examine the spatial and temporal occurrence of clusters from a selection of the CMIP6 models (see e.g. Eyring et al. 2016). This type of analysis over New Zealand has previously been reported for CMIP3 data (Parsons et al. 2014). Construction of a contingency table (Figure 7) comparing the clusters obtained from the two different reanalysis datasets used here would also be of interest.

6. Code and data availability

The analysis and plotting code used here is publicly available as a Jupyter notebook via GitHub (Williams 2021), the NCEP/NCAR reanalysis data is available at https://psl.noaa.gov/data/gridded/data.ncep.reanalysis.pressure.html and the ERA5 data is at https://cds.climate.copernicus.eu/cdsapp#!/dataset/reanalysis-era5-pressure-levels?tab=overview.

Acknowledgements

JW would like to thank Dr Nicolas Fauchereau of NIWA for the idea to use the scikit-learn package at the outset of this work (https://github.com/nicolasfauchereau/ACRE_workshop) and therein noting the problems associated with reproducing the regimes found in K2K, thus stimulating the pedagogical aspect of this work. We would also like to acknowledge Dr Andrew Lorrey, also of NIWA, for useful discussions on the use and interpretation of synoptic regimes. JW is funded through the Deep South National Science Challenge, under project C01X1902 from the New Zealand Government Department for Business, Innovation and Employment (MBIE). The authors wish to acknowledge the use of New Zealand eScience Infrastructure (NeSI) high performance computing facilities, consulting support and training services as part of this research. New Zealand's national facilities are provided by NeSI and funded jointly by NeSI's collaborator institutions and through the Ministry of Business, Innovation & Employment's Research Infrastructure programme. URL https://www.nesi.org.nz. The authors also wish to acknowledge the comments from two anonymous reviewers whose comments and suggestions have greatly improved this work.

Appendix A: Manually assigning new data to a cluster set

In this appendix we use the term 'observation' to encompass any new dataset to which clusters are assigned.

There have been many studies based on the Kidson types and several of these involve fitting new datasets to the Kidson types (e.g. Ackerley et al. 2011, Parsons et al. 2014). In this section the mathematical basis for this assignment is given.

The first step is to calculate the 'projection' of the z_s onto the individual EOFs. The dimensions of the EOFs are 5 × 13 × 11, that is, 5 EOFs over a region with 13 latitude values and 11 longitude values. The z_s values have dimensions of Nt × 13 × 11, where N_t is the number of timesteps considered. The projection, $\mathcal{P}$, is defined as,

$$\mathcal{P} = \sum_{jk} z_{s,jk} \mathcal{E}_{jk} \ , \qquad \text{(A.1)}$$

and therefore, the dimensions of $\mathcal{P}$ are $N_t \times 5$.

For each observation, we now have a 5 element array ($\mathcal{P}$) and a 12 × 5 element array representing the time mean of the PCs (P_n) for each index calculated by the K-means clustering algorithm,

$$C_{P,i} = \overline{P_i} \ , \qquad \text{(A.2)}$$

where $1 \leq i \leq 12$. The $C_{P,i}$ are often referred to in the literature as 'cluster means'.

To find out which of the 12 clusters the projection should be assigned to for each observation, the Euclidean distance, d, between the projection and each of the 12 height clusters is calculated. The projection and PC cluster arrays are normalised and are given by $\hat{\mathcal{P}}$ and $\hat{C}_{P,n}$ respectively. The minimum of these 12 numbers (i.e. the Euclidean distance in principal component space) gives the index and therefore the weather regime of each observation and its fractional occurrence. This can then be directly compared with the values obtained in Figure 3.

The Euclidean distances for each cluster, d_i, are given by,

$$d_i = \sqrt{\sum_{n=1}^{N_\mathcal{E}} \left| \hat{\mathcal{P}}_{n,i} - \hat{C}_{n,i} \right|^2} \ , \qquad \text{(A.3)}$$

where each of $\hat{\mathcal{P}}_{n,i}$ and $\hat{C}_{n,i}$ are 1 × 5 arrays and N_ε is the number of EOFs; i.e. 5 in this work.

A geometrical illustration of what the 'minimum Euclidean distance' means is shown in Figure A.1 for an arbitrary observation of z in the NCEP/NCAR reanalysis. It is clear that the figure showing the lowest d value - highlighted lines in Figure A.1(g) - has lines of $\hat{\mathcal{P}}$ and $\hat{C}$ which are closest to one another. The value of d can therefore be interpreted as a measure of the 'similarity' of $\hat{\mathcal{P}}$ and $\hat{C}$.

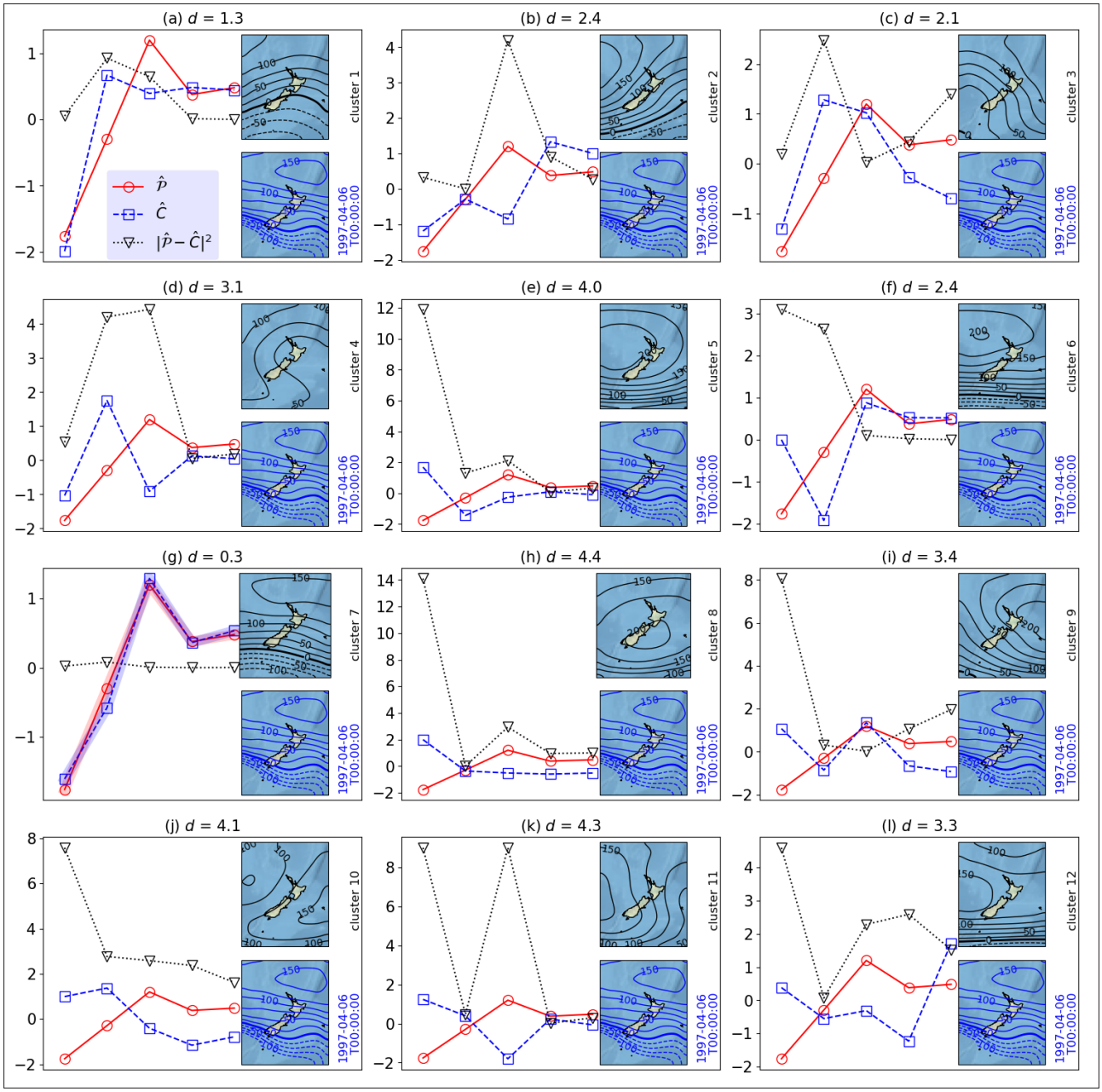

Figure A.1: Geometrical illustration of how an arbitrary observation of z (here at 0000 UTC on the 6th of April 1997) can be fitted to pre-existing clusters. Each subfigure shows the same arbitrary observation of geopotential height in the blue contours and the black contours show the 12 separate clusters obtained from this analysis (Figure 3 and Figures 5 (a) and (b)). As shown in the text, we want to find the smallest Euclidean distance, d, between the projection of the observation onto the EOFs, $\hat{\mathcal{P}}$ (○), and the cluster means, $\hat{C}$(□) as given by Equation 6. Note the simplified nomenclature used - i.e. lack of subscripts - to improve clarity. The individual $\left|\hat{\mathcal{P}} - \hat{C}\right|^2$ values are also shown (▽). The square root of the sum of the $\left|\hat{\mathcal{P}} - \hat{C}\right|^2$ values gives the Euclidean distance, d, shown in the subfigure titles and (g) highlights the similarity of the blue and red lines and hence the lowest d value.

References

Ackerley, Duncan et al. (2011). "Using synoptic type analysis to understand New Zealand climate during the Mid-Holocene". In: Climate of the Past 7.4, pp. 1189–1207.

Behrens, Erik et al. (2020). "Local grid refinement in New Zealand's earth system model: Tasman Sea ocean circulation improvements and super-gyre circulation implications". In: Journal of Advances in Modeling Earth Systems 12.7, e2019MS001996.

Cheng, Xinhua, Gregor Nitsche, and John M Wallace (1995). "Robustness of low-frequency circulation patterns derived from EOF and rotated EOF analyses". In: Journal of Climate 8.6, pp. 1709–1713.

Dawson, Andrew (2016). "eofs: A library for EOF analysis of meteorological, oceanographic, and climate data". In: Journal of Open Research Software 4.1.

Dawson, Andrew and Scott Wales (May 2019). ajdawson/eofs: Version 1.4.0. Version v1.4.0. doi: 10.5281/zenodo.2661604. url: https://doi.org/10.5281/zenodo.2661604.

Eyring, V. et al. (2016). "Overview of the Coupled Model Intercomparison Project Phase 6 (CMIP6) experimental design and organization". In: Geoscientific Model Development 9.5, pp. 1937–1958. doi: 10.5194/gmd-9-1937-2016. url: https://gmd.copernicus.org/articles/9/1937/2016/.

Gibson, Peter B, Sarah E Perkins-Kirkpatrick, and James A Renwick (2016). "Projected changes in synoptic weather patterns over New Zealand examined through self-organizing maps". In: International Journal of Climatology 36.12, pp. 3934–3948.

Harris, Charles R. et al. (Sept. 2020). "Array programming with NumPy". In: Nature 585.7825, pp. 357–362. doi: 10.1038/s41586-020-2649-2. url: https://doi.org/10.1038/s41586-020-2649-2.

Hersbach, Hans et al. (2020). "The ERA5 global reanalysis". In: Quarterly Journal of the Royal Meteorological Society 146.730, pp. 1999–2049.

Jiang, Ningbo (2011). "A new objective procedure for classifying New Zealand synoptic weather types during 1958–2008". In: International Journal of Climatology 31.6, pp. 863–879.

Jiang, Ningbo, Kim N Dirks, and Kehui Luo (2013). "Classification of synoptic weather types using the self-organising map and its application to climate and air quality data visualisation". In: Weather and Climate 33, pp. 52–75.

Jiang, Ningbo, John E Hay, and Gavin W Fisher (2004). "Classification of New Zealand synoptic weather types and relation to the Southern Oscillation Index". In: Weather and Climate 23, pp. 3– 23.

Kalnay, Eugenia et al. (1996). "The NCEP/NCAR 40-year reanalysis project". In: Bulletin of the American Meteorological Society 77.3, pp. 437–472.

Kidson, John W (1994a). "An automated procedure for the identification of synoptic types applied to the New Zealand region". In: International Journal of Climatology 14.7, pp. 711–721.

Kidson, John W (1994b). "Relationship of New Zealand daily and monthly weather patterns to synoptic weather types". In: International Journal of Climatology 14.7, pp. 723–737.

Kidson, John W (1997). "The utility of surface and upper air data in synoptic climatological specification of surface climatic variables". In: International Journal of Climatology: A Journal of the Royal Meteorological Society 17.4, pp. 399–413.

Kidson, John W (1999). "Principal modes of Southern Hemisphere low-frequency variability obtained from NCEP– NCAR reanalyses". In: Journal of Climate 12.9, pp. 2808–2830.

Kidson, John W (2000). "An analysis of New Zealand synoptic types and their use in defining weather regimes". In: International Journal of Climatology: A Journal of the Royal Meteorological Society 20.3, pp. 299– 316.

Kidson, John W and Ian G Watterson (1995). "A synoptic climatological evaluation of the changes in the CSIRO nine-level model with doubled CO2 in the New Zealand region". In: International Journal of Climatology 15.11, pp. 1179–1194.

Michelangeli, Paul-Antoine, Robert Vautard, and Bernard Legras (1995). "Weather regimes: Recurrence and quasi stationarity". In: Journal of the Atmospheric Sciences 52.8, pp. 1237–1256.

Moore, Todd W and Richard W Dixon (2015). "Patterns in 500 hPa geopotential height associated with temporal clusters of tropical cyclone tornadoes". In: Meteorological Applications 22.3, pp. 314– 322.

Parsons, Simon, Adrian J McDonald, and James A Renwick (2014). "The use of synoptic climatology with general circulation model output over New Zealand". In: International journal of climatology 34.12, pp. 3426–3439.

Pedregosa, F. et al. (2011). "Scikit-learn: Machine Learning in Python". In: Journal of Machine Learning Research 12, pp. 2825–2830.

Pohl, Benjamin et al. (2021). ""Beyond Weather Regimes": Descriptors Monitoring Atmospheric Centers of Action—A Case Study for Aotearoa New Zealand". In: Journal of Climate 34.20, pp. 8341– 8360. doi: 10.1175/JCLI-D-21-0102.1. url: https://journals.ametsoc.org/view/journals/ clim/34/20/JCLI-D-21-0102.1.xml.

Saavedra-Moreno, B et al. (2015). "Surface wind speed reconstruction from synoptic pressure fields: machine learning versus weather regimes classification techniques". In: Wind Energy 18.9, pp. 1531– 1544.

Sellar, Alistair A et al. (2020). "Implementation of UK Earth system models for CMIP6". In: Journal of Advances in Modeling Earth Systems 12.4, e2019MS001946.

Sheridan, Scott C and Cameron C Lee (2011). "The self-organizing map in synoptic climatological research". In: Progress in Physical Geography 35.1, pp. 109–119.

Sheridan, Scott C, Helen C Power, and Jason C Senkbeil (2008). "A further analysis of the spatiotemporal variability in aerosols across North America: Incorporation of lower tropospheric (850hPa) flow". In: International Journal of Climatology: A Journal of the Royal Meteorological Society 28.9, pp. 1189–1199.

Solman, SA and CG Menéndez (2003). "Weather regimes in the South American sector and neighbouring oceans during winter". In: Climate Dynamics 21.1, pp. 91–104.

Trenberth, Kevin E (1997). "The Definition of El Niño". In: Bulletin of the American Meteorological Society 78.12, pp. 2771–2778.

Virtanen, Pauli et al. (2020). "SciPy 1.0: Fundamental Algorithms for Scientific Computing in Python". In: Nature Methods 17, pp. 261–272. doi: 10.1038/s41592-019-0686-2.

Ward J, H (1963). "Hierarchical grouping to optimize an objective function". In: Journal of the American Statistical Association 58.301, pp. 236–244.

Williams, Jonny (Aug. 2021). weather-types. doi: 10.5281/zenodo.5339123.
url: https://github.com/jonnyhtw/weather-types.

Williams, Keith D and MJ Webb (2009). "A quantitative performance assessment of cloud regimes in climate models". In: Climate Dynamics 33.1, pp. 141–157.

Trend analysis on frequency of New Zealand climate extremes

R. Srinivasan[1], T. Carey-Smith[1] and G. Macara[1]

[1]*NIWA-Taihoro Nukurangi, 301 Evans Bay Parade, Ākautangi, Hātaitai, Wellington, Aotearoa New Zealand*

Correspondence: Raghav.Srinivasan@niwa.co.nz , +64-4-386-0525

Key words: Climate extremes, rankings, climate change, temperature extremes, rainfall extremes

Abstract

NIWA publishes monthly climate summaries which report on the occurrence of extreme climate and weather events. These summaries provide context to present-day observations with respect to the historical record at stations located throughout New Zealand. In the last decade, NIWA has reported many record-setting high temperature extremes in the climate summaries, with comparatively few record-setting low temperature extremes. In this study, we have generated ranked temperature and rainfall data iteratively from 1951 to 2020 and assessed if the trend of occurrences of these extremes (high & low) in New Zealand is changing. To do this, we calculated an extremeness ratio, which is derived by normalising the observed extremes with an expected probability of an extreme based on no long-term warming. We found that, in the last decade, on average, high monthly mean temperature extremes in New Zealand are increasing 4-5 times larger than expected in a climate with no long term warming. We also examined New Zealand's homogenised seven-station temperature series and found a similar trend for mean temperature extremes. In addition, we calculated the mean temperature extremes taking the climate warming trend (~ 1° C per century) into account and found that the rate of increase in extremes is faster than the rate of increase in mean temperature. We also find a positive trend in both high and low rainfall extremes with the low rainfall trend most prominent in eastern New Zealand.

1. Introduction

1.1 Background and context

Many National Meteorological and Hydrological Services issue monthly bulletins containing data from a selection of stations within the country and which may include monthly averages, extremes, and other statistical data (WMO, 2018). These bulletins provide useful information on climate and its variability (WMO, 2018) and often give historic context to contemporary climate observations.

Starting in 2008, New Zealand's National Institute of Water and Atmospheric Research Ltd. (NIWA) has routinely produced monthly, seasonal, and annual climate summaries, and these are primarily disseminated to end users via online publication (NIWA, 2021a). These summaries describe observed temperature and rainfall throughout representative geographical regions of New Zealand, and they highlight any extreme weather and climate events that have occurred. There is an extensive network of climate stations operating throughout New Zealand (data available at cliflo.niwa.co.nz) and data from these stations are used to inform the climate summaries.

Submitted: 10 August 2021
Accepted: 29 October 2021

NIWA provides historic context to contemporary observations of climate data by generating rankings for its monthly climate summaries. Specifically, climate data for a given month at a given climate station will be compared with relevant contemporary and historical data for that location to obtain a ranking. A convention has been adopted that if the present ranking is among either the top-four or bottom-four, then the data and associated ranking are presented in the climate summaries. This criterion is arbitrary, but allows NIWA to highlight climate stations where the observed climate for a given period has been particularly notable. We follow this convention, and refer to data values with a top-four or bottom-four ranking as an extreme.

NIWA presents monthly rankings for temperature, rainfall and wind. In the past, rankings of total hours of sunshine were also presented by NIWA. However, this was discontinued in recent years, due to the complexity associated with the comparison of historic sunshine totals measured by manual instruments with contemporary totals from electronic sensors (Legg, 2014; Srinivasan et al., 2019).

The global climate has changed, and human activities are estimated to have caused approximately 1.09°C of global warming above pre-industrial levels (IPCC, 2021). According to the record of global land and ocean temperatures spanning 1880-2020, the seven warmest years have all occurred since 2014, while the 10 warmest years have occurred since 2005 (NOAA, 2021). As a result of such climatic change, the probability of establishing new warm monthly temperature records worldwide has increased, on average five times larger than expected in a climate with no long-term warming (Coumou et al., 2013). Studies in the United States of America and Australia have assessed the changes in occurrence of record high and low daily temperatures (Meehl et al., 2009; Trewin and Vermont, 2010), showing that high temperature extremes have become increasingly more common than low temperature extremes in both countries.

New Zealand's climate has also changed, with the nationwide average temperature rising by a rate of 1.04 ± 0.25°C per century over 1909-2020 (NIWA, 2021b). Since 1998, nine years (1998, 1999, 2005, 2013, 2016, 2017, 2018, 2019 and 2020) have ranked among New Zealand's ten hottest on record (the remaining top-10 hottest year being 1971), with the highest nationwide average temperature of 13.45°C observed in 2016 (NIWA, 2021b). In light of such regularly high nationwide temperatures in recent times, it is reasonable to expect that individual locations throughout New Zealand will have also observed record or near-record high temperatures.

Indeed, for regular users of NIWA's climate summaries, a contemporary imbalance in the number of record or near-record temperature observations is readily apparent. Specifically, there have been many more occurrences of record or near-record high monthly temperatures relative to record or near-record low monthly temperatures. This imbalance was highlighted by Macara and Srinivasan (2018), who showed that from August 2012 to October 2018, there were 1271 instances of record or near-record high monthly mean temperatures at New Zealand locations, compared to just 105 instances of record or near-record low monthly mean temperatures. Whilst this is a stark difference, it is notable that the time period assessed (6 years) is relatively short, and hence the imbalance over longer time scales cannot be assessed. Furthermore, the number of station groupings (Section 2.1.1) examined were not static over the assessed period.

1.2 Study aims

The aim of this study is to provide additional context to climate records published in NIWA's monthly climate summaries, particularly with respect to changing frequencies and trends of occcurrence of extremes. How do the frequencies of these published extremes differ

from those of a stationary climate (Section 3.1, Section 3.2) for a static set of station groupings, and are the trends in temperature extremes consistent with New Zealand's observed warming (Section 3.4)? By quantifying the changing frequency of record or near-record climate observations in the context of climate summaries in New Zealand, we will determine if the trends are significant and also whether discrepancies between high and low occurences are apparent.

Climate summaries published in New Zealand typically use regional groupings of non-homogenised station records to portray or represent the climate of areas of interest, such as population centres or homogeneous geographic regions. These groupings are further described below. To assess the validity of presenting extremes based on groupings, we will compare the non-homogenised station grouping mean temperature extremes against those derived from NIWA's seven-station homogenised dataset (Mullan et al., 2010) in Section 3.3. Finally, we also compare the frequency of mean temperature extremes from the seven-station series to the background climate warming trend in Section 3.4. By taking the positive trend of mean temperatures into account, we aim to test whether or not the occurrence of extremes is consistent with what might be expected due to a warming climate.

2. Methodology

2.1 Climate extremes calculation process

2.1.1 Station groupings

Over time, New Zealand's climate monitoring network has changed, with new stations opening, stations closing, instrumentation changes, station location changes, and potential station exposure changes. This poses a challenge to providing un-biased historic context for contemporary observations for New Zealand locations. For example, if a station has been operational for only five years, then it is not particularly notable for that station to observe its highest monthly mean temperature on record.

To account for the dynamic nature of the climate monitoring network in New Zealand, 190 station groupings have been established. These groupings encompass open climate stations (i.e. operational) and additional closed climate stations (i.e. no longer operational) for cities, towns and other rural or isolated areas of the country where climate data are available. The stations comprising each grouping have been carefully selected to ensure their overall climate characteristics are comparable, and representative of the climate at the grouping location. As such, there is more than one grouping at several of New Zealand's main centres. An example of this is Wellington city, where there are two groupings. One is based on stations at Kelburn, a hillside suburb to the northwest of the central business district (CBD), whilst the other is based on stations at the Airport, a low-elevation coastal location to the southeast of the CBD. Separate groupings are necessary here because the difference in elevation and exposure to prevailing winds means that the site clusters have a different rainfall and temperature climatology.

NIWA uses these station groupings when generating location-based rankings listed in its Climate Summaries. The current climate value is compared against all values from all stations within the group, without any regard for homogeneity between one station's record and another. This approach is used due to the practical limitations of performing homogeneity checks in real-time, as well as the complexity associated with developing homogenous historic records.

Data homogeneity is a major issue in the assessment of changes in observed climate (e.g. Trewin and Vermont, 2010). In order to address this, NIWA's seven station series was also used in this study as an independent benchmark of the temperature trend. This series comprises a homogenous temperature record for seven New Zealand

locations dating back to 1909 (Mullan et al., 2010). When data from these locations are combined, they form New Zealand's nationwide reference temperature time series, which is regularly updated in NIWA's Climate Summary reports.

2.1.2 Method of calculation

For this study, extremes have been calculated so as to emulate the existing procedure which is part of NIWA's National Climate Database automated monthly statistical processing. This processing includes quality control checks and standard statistical calculations such as monthly means. For the indices described in Table 1, the rank of the current month's value is calculated for each station grouping. If the value is ranked in the top four it is classified as extreme and stored in the database along with its anomaly with respect to the 1981-2010 climate normal value. In the case where the value of an extreme is same as a previous extreme, an 'equal' rank is assigned.

To be eligible for an extreme ranking, the station grouping must have a record length of at least 20 years. The automated ranking process has been operational only since the year 2008. However, for this study rankings have been calculated retrospectively back to 1951 for only those station groupings with records starting at or before 1931. Precalculation of the initial 4th ranked extreme value prior to the year 1951 for each station grouping was done separately and the ranking calculation process was run from 1951-2020 to archive all the monthly extremes that were observed during this period. Querying this archived record enabled us to construct the timeseries of frequency of extremes that occurred from 1951 to 2020.

2.2 Extremeness ratio

As discussed in the previous section, extremes are ranked based on the historical record and any value that exceeds a previous historical threshold becomes a new extreme. This means that the threshold for a new extreme changes over time. In the case of high extremes the threshold increases and for low extremes the threshold decreases with every new extreme event. As a result, an extreme that occurs later in a timeseries carries more weight, i.e. is more unusual, than an extreme that occurred prior. This behaviour is depicted schematically in Figure 1, which shows the probability of a high extreme event decreasing

Table 1: Climate indices assessed in this study. The equivalent ETSCI index abbreviation is included where relevant (https://climpact-sci.org/indices).

Climate Index	ETSCI code	Description
Mean air temperature	TMm	Monthly average air temperature, calculated as the average of the monthly mean of daily maximum and minimum temperatures.
Mean max air temperature	TXm	Monthly average daily maximum air temperature.
Mean min air temperature	TNm	Monthly average daily minimum air temperature.
Extreme max temperature	TXx	Monthly highest daily maximum air temperature.
Lowest max temperature	TXn	Monthly lowest daily maximum air temperature.
Extreme min temperature	TNn	Monthly lowest daily minimum air temperature
Highest min temperature	TNx	Monthly highest daily minimum air temperature.
Total monthly rain	N/A	Monthly sum of daily rainfall totals.
Highest 1-day rain	Rx1day	Monthly maximum daily rainfall total.

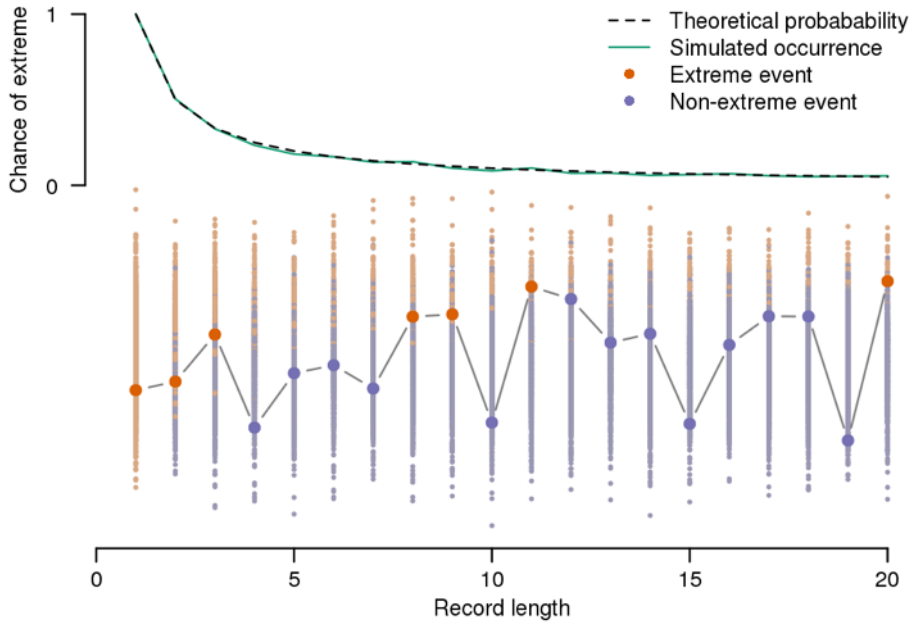

Figure 1: Simulation of extremes occurrence based on a stationary Gaussian distribution. The large orange and purple dots show record and non-record events from a single random time-series, while the smaller dots show events from 999 other realisations. By definition, the first year of all simulations is 'extreme'. The green line shows the proportion of simulated extreme events at each time step, while the black dashed line is 1/N, where N is the record length.

over time. In order to assess whether a particular climate index is producing more or less extremes than would be expected based on record length, we have used an 'extremeness ratio', *R*. This is the average of the ratio of observed extreme, *O(ext)*, against expected probability of an extreme, *P(ext)*, across all months in a year *(m)* and station groupings *(s)*:

$$R = \frac{1}{s \times m} \sum_{i=1}^{s} \sum_{j=1}^{m} \frac{O_{i,j}(ext)}{P_i(\text{ext})} \qquad (1)$$

Assuming the climate is stationary, the expected probability of a new record is 1/*N* where *N* is the length of the record for the particular station grouping and ranking. To account for the inclusion of the top four ranked values, we have used the following equation as the expected probability of an extreme:

$$P(ext) = {}^{4}/_{N} \qquad (2)$$

Observed extremes have been assigned a binary value of *O*=0 in case of no extreme observed for a given month and group and *O*=1, if there was any 1-4 ranking value observed. If the final *R* value for a given year is greater than 1, it implies that there were more extremes observed than would be expected based on the record lengths of the station groupings at that point. After calculating an annual series of *R* for each variable in Table 1, a linear trend was fitted to each series with respect to year. This was done to assess the statistical relationship of *R* with respect to year thereby testing the existence of any underlying trend.

3. Results

As described above, a linear model with respect to year was fitted to the annual series of *R* to test the null hypothesis that there is no relationship between *R* and year (i.e. no positive or negative trend). Using the p-value from each model we can assess whether the trend is significantly different from zero. Based on this analysis, for all high temperature extremes, we found a

positive trend with high statistical significance (Table 2). We also found significant positive trends for all rainfall extremes, with low total rain extremes having the highest significance. No statistically significant trend was found for low temperature extremes except for the extreme min and lowest max temperature. Further details of the results are discussed in the following sections, where we also describe tests performed to ensure the results are not dependent on timeseries length, number of groupings or number of extremes per month.

3.1 Temperature-related trend

To show the effect of the normalisation process, Figure 2 compares the mean occurrence of unnormalised extremes against the extremeness ratio for monthly mean high temperature extremes. The mean number of unnormalised extremes was derived without applying any correction factor for the length of the record. So, if there was any top-4 ranked record, it was counted as 1 for each month and grouping, and then averaged across all groupings for the whole year. As illustrated in Figure 2, the mean occurrence of unnormalised high temperature extremes is relatively constant through this period except for last decade. Conversely, the trend in the extremeness ratio becomes increasingly positive as the record length increases, leading to an increased difference between the two trend lines going forward in time.

To ensure that our use of the top-4 extremes (normalising by $4/N$) does not impact on the validity of the results, we compared the equivalent extremeness ratio based on only the top extreme normalised by $1/N$ (Figure 2, blue line). As can be seen, both the $1/N$ and $4/N$ time-series give consistent results and therefore we have used the top four ranked extremes with an expected probability of $4/N$ for our trend analysis as this increases the sample size, improving the significance of the results.

The main trend analysis is performed from 1951 to 2020 and as a result, the number of station groupings were limited due to availability of observations from at least 1931 (as described in Section 2.1.2). This was to ensure there were at least 20 years of observation as of 1951

Table 2: Observed trend in occurrence of extremes, 1951-2020.

Climate Index	Extreme type	Estimate per year (increase in R per year)	p-value - confidence
Mean air temperature	High	0.040	>99.9%
Mean max air temperature	High	0.0411	>99.9%
Mean min air temperature	High	0.028	>99.9%
Extreme max temperature	High	0.025	>99.9%
Highest min temperature	High	0.023	>99.9%
Total monthly rain	High	0.009	>99%
Highest 1-day rain	High	0.011	>99.9%
Mean air temperature	Low	-0.002	No significance
Mean max air temperature	Low	-0.001	No significance
Mean min air temperature	Low	0.001	No significance
Extreme min temperature	Low	0.007	>95%
Lowest max temperature	Low	0.011	>99%
Total monthly rain	Low	0.011	>99.9%

and also to prevent new station groupings being added in the latter part of the timeseries. Approximately 46 temperature groups met these conditions and in order to test that these groups represent the overall trend, we compared the mean temperature trend output of these 46 groups with a set of 85 groups that met the same set of conditions from 1971 onwards. The comparison showed that the trend was similar and robust even for this shorter time period with the additional groups available post-1971 (Figure 2, black line). This comparison also highlights that the extremeness ratio is producing comparable results regardless of length of record between the groups starting from 1951 vs 1971. The groupings from 1951 were distributed evenly throughout the country except a gap in coverage from Auckland to Whangarei.

Figure 3 plots the extremeness ratio for all temperature variables (both high/low) with respect to year. As can be seen, the temperature-related variables have a strong positive trend for high extremes (Figure 3a, b, and Table 2). Mean temperature, max and min temperature variables show no trend in case of low extremes (Figure 3c and Table 2), indicating the high temperature extremes are now occurring much more frequently than low temperature extremes. Extreme daily min temperature and lowest daily max temperature have minor positive trends and show high variability around the expected value of 1. We also analysed if there were any differences in temperature related trend between east coast vs west coast and both showed similar trends for both high and low extremes in mean temperature.

3.2 *Rainfall-related trend*

For the rainfall analysis, 78 groups were used which had data available satisfying the 20 year observations condition from 1951. The results of the trend analysis are summarised in Table 2 above. Similar to temperature, we performed an analysis of mean unnormalised extremes with respect to extremeness ratio for low rainfall extremes

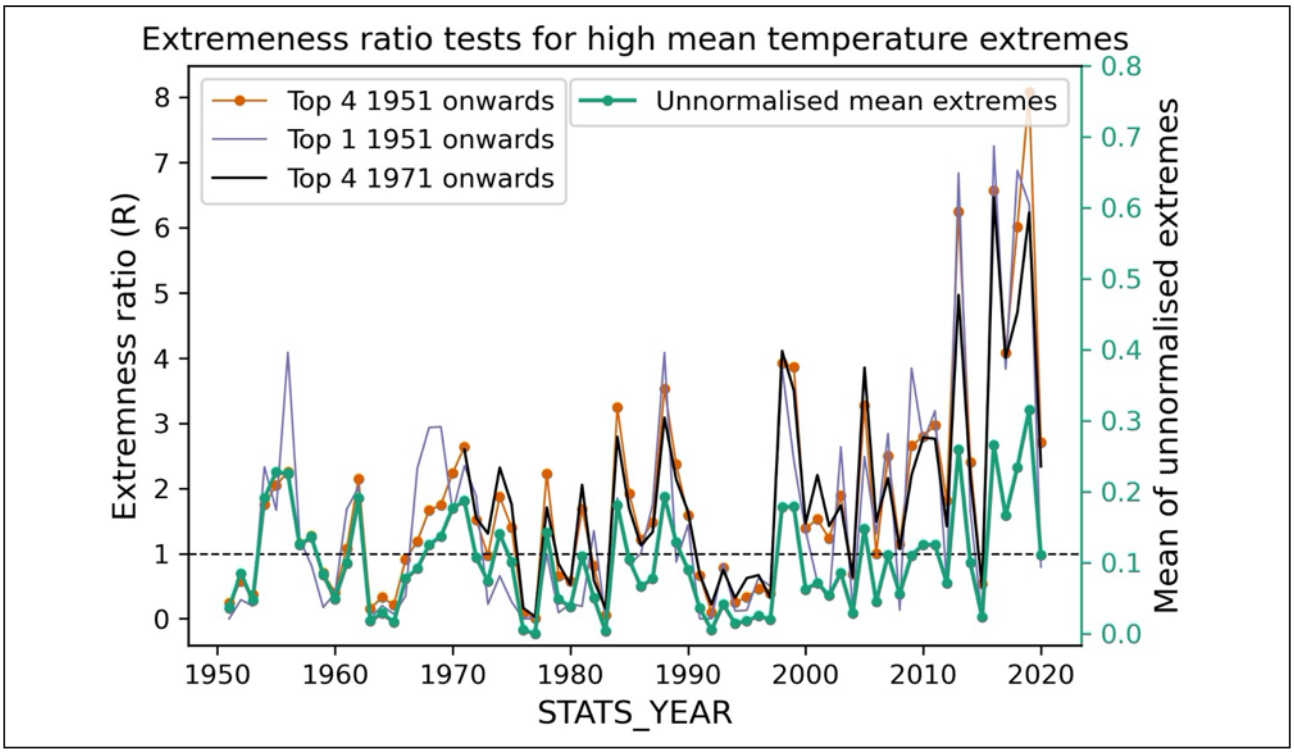

Figure 2: The annual time series of mean unnormalised extremes (green) compared with normalised extremes (orange). Also included is a time-series of normalised extremes based only on the top-most extreme (purple). Finally, the black solid line is the top-4 extremes from 1971 with additional groups following a very similar trend with top-4 extremes from 1951. The black dotted line indicates expected extremes in a stationary climate.

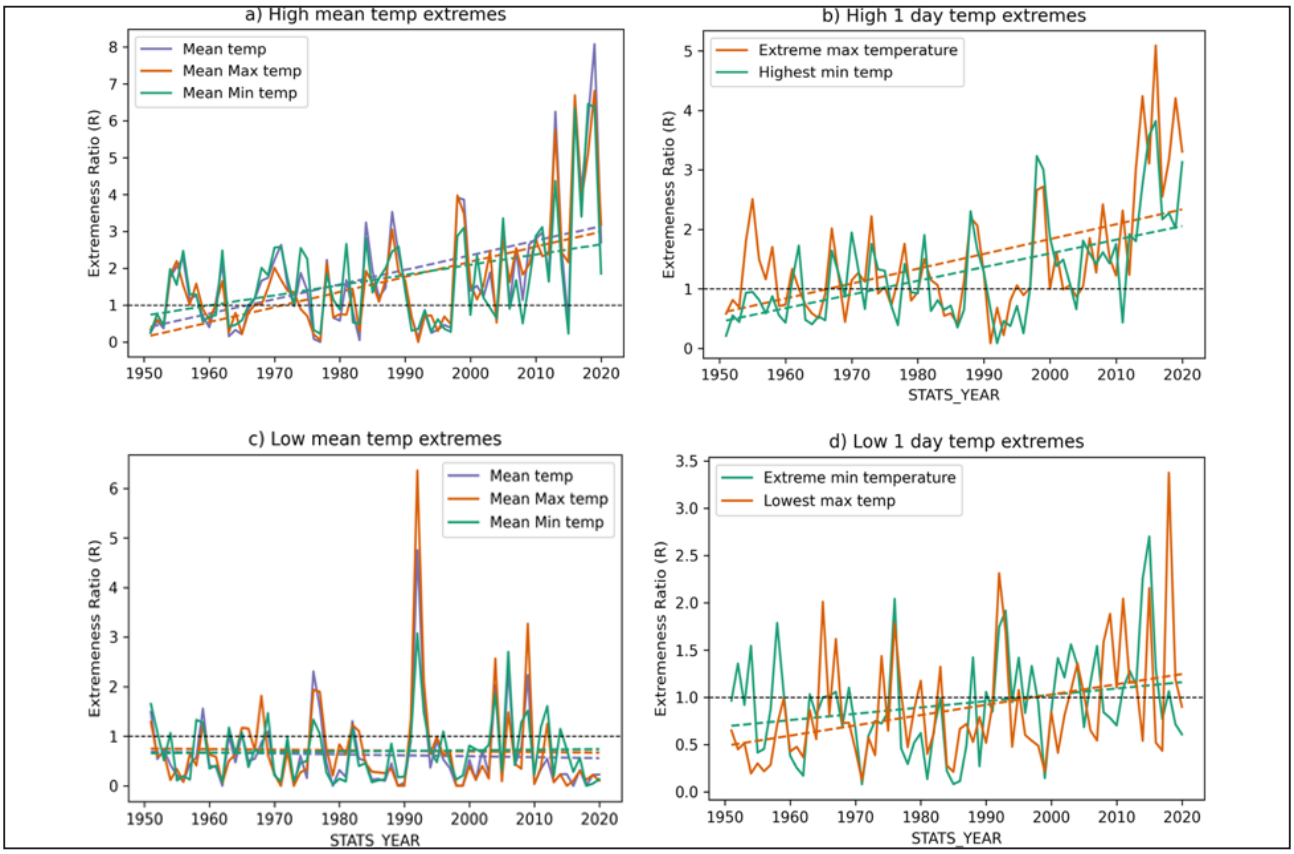

Figure 3: Results for all temperature extremes: a) high mean temperature (top-left), b) high 1-day temperature extremes (top-right), c) low mean temperature extremes (bottom-left), and d) low 1-day temperature extremes (bottom-right). Dotted lines in all panels are the fitted linear trend line corresponding to each variable.

(Figure 4a). Here we do not investigate the Top1/Top4 or post 1971 versions for rainfall extremes.

In this case, unlike temperature, the trend of mean unnormalised low rain extremes was negative and the process of normalisation to this mean raw low rain extremes adjusts the trend in the positive direction. This positive trend is in line with the overall drying trend that is represented by the total monthly potential evapotranspiration deficit (PED[1]) averaged across all the stations as can be seen in Figure 4a. We observe a statistically significant (99.9% confidence) linear relationship between PED and low rain extremes resulting in a 0.005 increase in *R* per mm increase in PED. In addition, Figure 4b plots the high monthly rainfall extremes trend along with high 1-day rainfall trend, both of which show a small but significant positive trend. Although small, both high and low rainfall extremes demonstrate a positive trend (Table 2) and this might be an indication of increasing variability in overall rainfall patterns.

To investigate the rainfall trends in more detail, the station groupings were separated into an 'east coast' and 'west coast' set based on the regional classification[2] system used in the climate database. The south of South Island and Northland regions were not included in either the west or east coast grouping. Figure 5 contains the extremeness ratio separated into east and west coast for both high and low rainfall extremes. The annual low extremes have similar variability in R between the east and west coasts except during the 1970s and 80s. This disagreement could be related to the changing phase of the Inter-decadal Pacific Oscillation (IPO) shown on Figure 5 with a thick

[1] *https://niwa.co.nz/climate/information-and-resources/drought/charts*
[2] *https://docs.niwa.co.nz/library/public/NZMSmp110(1985).pdf*

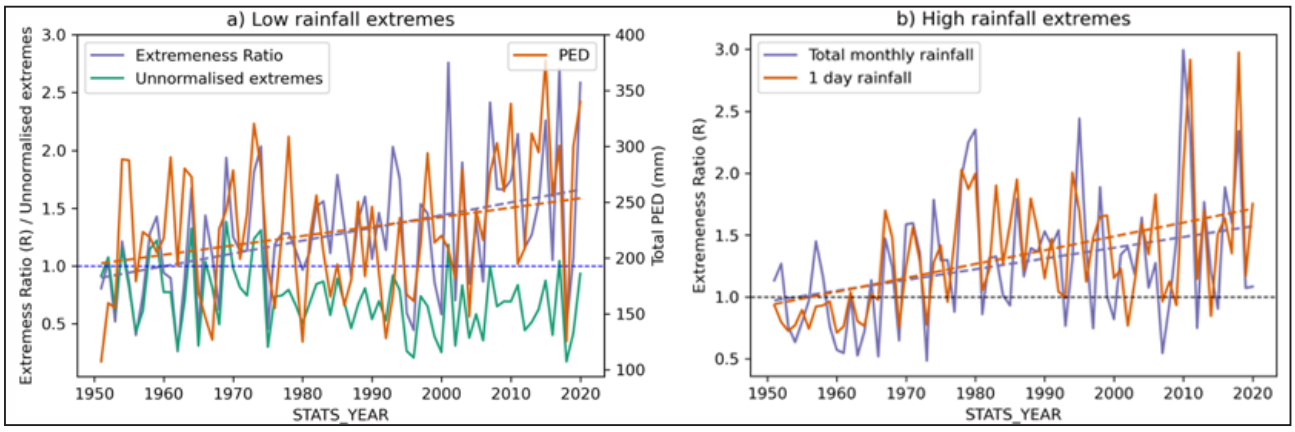

Figure 4: a) Low rain trend compared with extremes without normalisation and PED. Note: A scaling factor of 10 was applied to the unnormalised extremes so they could be included with the extremeness ratio on a single axis. b) High rain extremes (1-day rain and total monthly rain). Dotted lines in all panels are the fitted linear trend line corresponding to each variable.

green line depicting the negative phase. For high rainfall extremes, the difference between the west and east coast overall trends is small. For low rainfall extremes, an overall stronger positive trend (99.9% confidence) is observed for the east coast when compared with the west coast where very little trend (no statistical significance) is observed. This trend in the east coast is consistent with the projections of increased westerly winds in New Zealand, especially during winter and spring, thereby causing drier conditions in the east (MFE, 2018).

3.3 Comparison with seven-station homogenised series

To examine the impact of using data from station groupings that were not homogenised, extremes in NIWA's seven-station mean temperature series (Mullan et al., 2010) were also assessed using the methodology described in Section 2. We calculated the Extremeness Ratio from the seven-station series dataset and compared it against the equivalent ratio from the station groupings. As illustrated in Figure 6, the extremeness ratios of both the station groupings and seven-station series show a

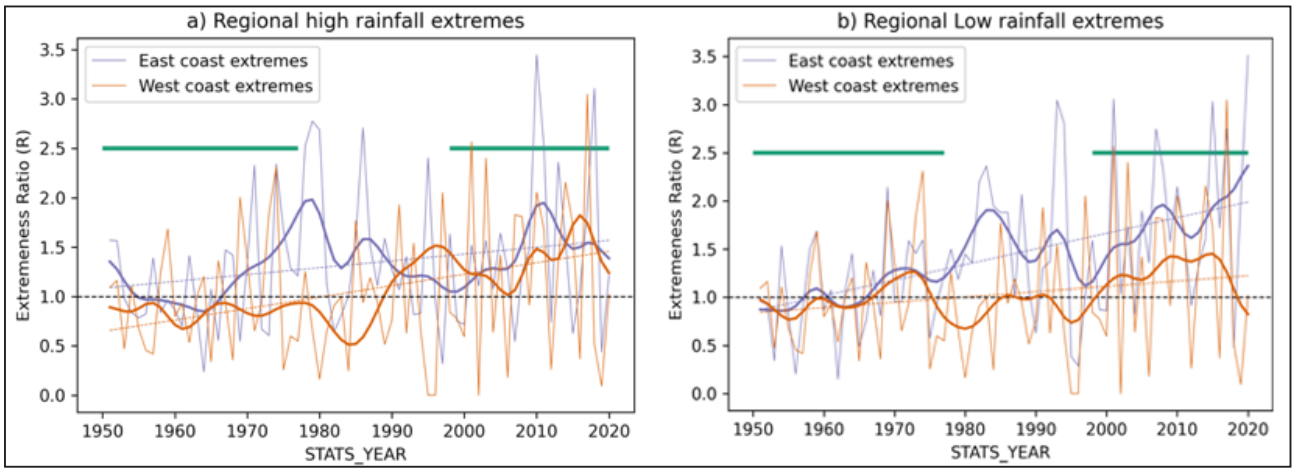

Figure 5: Occurrence of rainfall extremes, partitioned by east and west coast region. Smoothing is done using 1d Gaussian filter (sigma=2). Dotted lines in all panels are the fitted linear trend line corresponding to each region. Thick green line in the plot represents the period of Gaussian smoothened (sigma=2) IPO negative phase and the disagreement between west and east coast high/low extremes in 1970s and 1980s might be related to the changing phase of IPO.

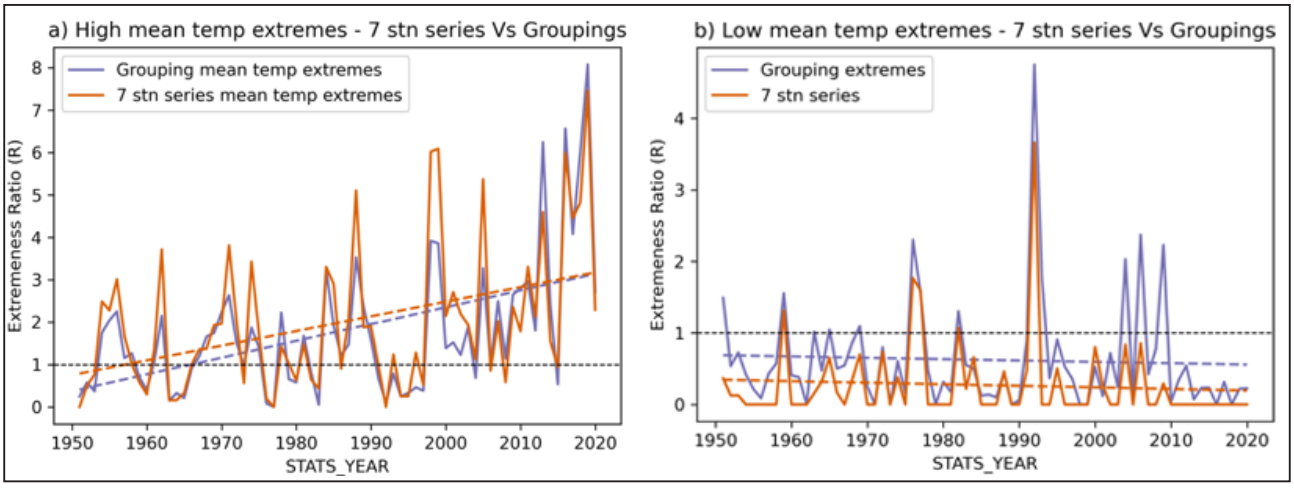

Figure 6: Seven-station series extremes vs station grouping extremes. Dotted lines in all panels are the fitted linear trend line corresponding to groupings and 7 station series mean temperature extremes.

consistent strong upward trend for mean temperature high extremes and no trend for low temperature extremes. There was a high correlation coefficient of 0.9 for high mean temperature extremes and 0.86 for low mean temp extremes between the seven-station series and the station grouping data. This highlighted that the station groupings were capturing the overall trend and variability in extremes that was observed in the homogenised dataset.

3.4 Comparison of stationary and trend-corrected extremeness ratio

As described in Section 2, we calculated our extremeness ratio assuming a stationary climate. In other words, we estimated our expected probability of an extreme based on $1/N$ law giving equal chance of an extreme based on the length of the record. Coumou et al., (2013) performed a study of mean monthly temperature extremes comparing the extremes on a stationary climate against a climate with a long-term warming trend. They calculated the extremeness ratio with expected probability of an extreme using $1/N$ (for stationary climate) and compared with an expected probability of $1/N$ + trend (for warming climate). We performed a similar comparison on the seven-station series dataset to test if the extremes were changing at the same rate as the mean temperature. For a warming climate, we used the following expected probabilty (Franke et al., 2010; Coumou, et al., 2013):

$$P(N) \approx 4\left(\frac{1}{N} + \alpha(N)\frac{\mu}{\sigma}\right) \quad \text{and} \quad \alpha(N) = \frac{2\sqrt{\pi}}{e^2}\sqrt{\ln\left(\frac{N^2}{8\pi}\right)} \qquad (3)$$

where μ is the long-term linear trend for each station and month and σ is the short-term variability for each station and month. A multiple of 4 was included to account for the use of the top-4 extremes.

After deriving the expected probability for each station using the above equation, we derived the Extremeness ratio and compared with the $4/N$ extremeness ratio as shown in Figure 7.

By the end of the 2010s, the mean temperature extremes are on average 4 to 5 times more than expected given a stationary climate, and are 2 to 3 times more than expected given a non-stationary climate. So, after taking into account the long term temperature trend of around 1 degree per century, we are still observing on average 2 to 3 times more extremes than expected, indicating that extreme events are increasing at a faster rate than the mean temperature. This implies that the shape of the temperature distribution is also changing.

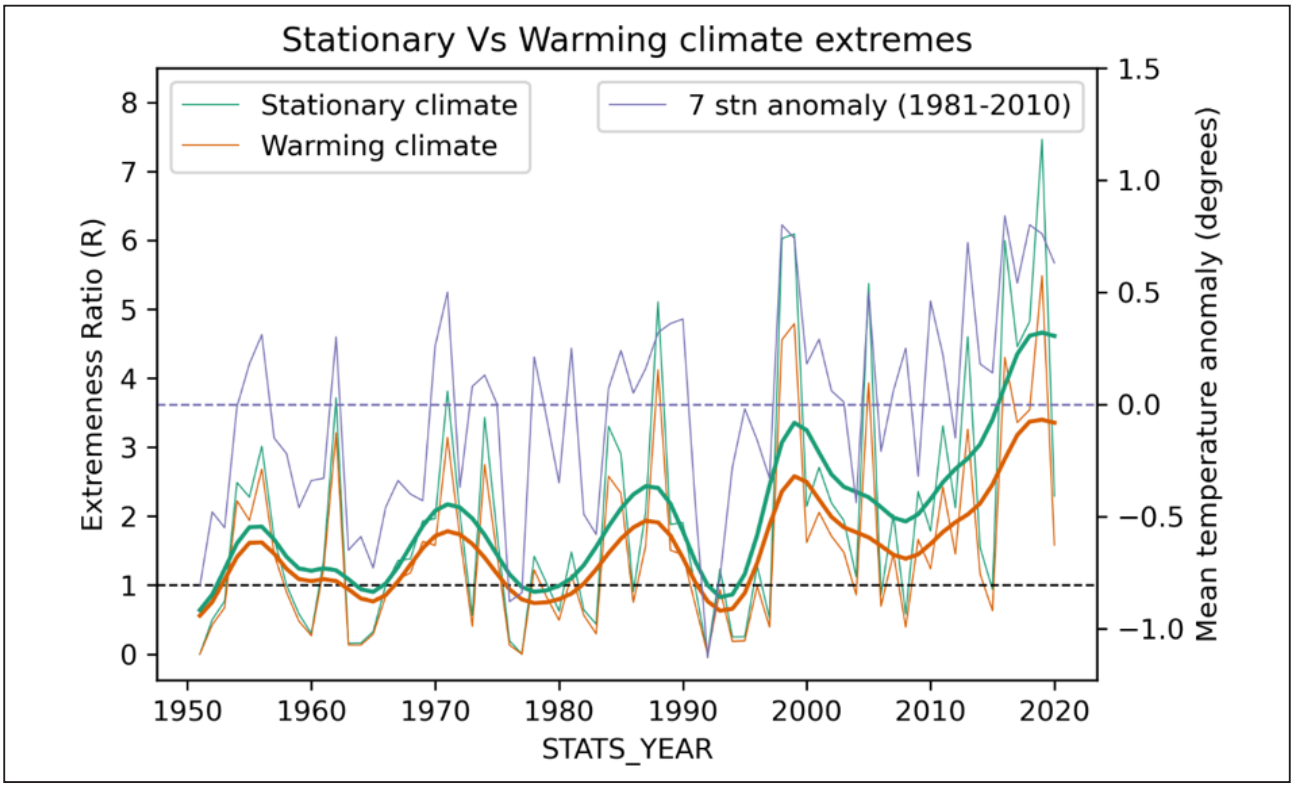

Figure 7: Blue is the mean temperature anomaly for the seven-station series (1981-2010 normal) using the right-side axis. Green is the extremes normalised assuming an expected probability due to a stationary climate. Red is the extremes adjusted using the warming climate trend estimated from the seven-station series which should follow the y=1 line, if the increase in extremes is consistent with the mean temperature trend. Smoothing is done using 1D Gaussian filter (sigma=2).

4. Conclusion and future work

In this study we derived an extremeness ratio assuming a stationary climate to represent frequencies of extremes for different temperature- and rainfall-related variables in New Zealand, from 1951-2020. We performed trend analyses and found a strong positive trend for all high temperature extremes, with extremes increasing around 4-5-fold on average in the last couple of decades in New Zealand. We could also determine from the trend that high temperature extremes occur more frequently than low temperature extremes. A positive trend for both high and low total rainfall extremes is observed, with low rain extremes mainly increasing in the east coast of New Zealand. We have also compared non-homogenised mean temperature extremes with the seven-station series and found that the station groupings were capturing the overall trend reasonably consistently in comparison with a homogenised dataset. This provides confidence that we can derive a more comprehensive New Zealand-wide picture and include variables not captured by the seven-station series. Finally, we derived mean temperature extremes after taking into account the mean warming trend and found that the rate of high temperature extremes is increasing faster than the mean temperature increase.

The result from this study provides confidence and additional context to NIWA's method of presenting climate records in the Climate Summaries, and in particular addressing scientific and public interest in how the frequency in climate extremes may be changing with long term climate change. As a next step, the extremeness ratio calculation can be operationalised and included in the monthly climate summaries to provide additional context to reported extremes. Also, the calculation of

temperature extremes from the homogenised seven-station series can also be operationalised and used as a reference for temperature extremes. In future, we also intend to perform additional analyses on low rainfall extremes and its relationship with the New Zealand Drought Index (NZDI) (Mol et al., 2017) and the climate indices (Thomson., 2006). This would enable a more comprehensive comparison of drought with low rainfall extremes.

Acknowledgements

The authors would like to thank Andrew Harper, Alan Porteous and Errol Lewthwaite of NIWA for their support of this work.

References

Coumou, D., Robinson, A., Rahmstorf, S. (2013) Global increase in record-breaking monthly-mean temperatures. Climate Change, 118, 771-782.

Franke, J, Wergen, G, Krug, J (2010) Records and sequences of records from random variables with a linear trend. J Stat Mech 10:1–22.

IPCC, (2021) Summary for Policymakers. In: Climate Change 2021: The Physical Science Basis. Contribution of Working Group I to the Sixth Assessment Report of the Intergovernmental Panel on Climate Change [Masson-Delmotte, V., P. Zhai, A. Pirani, S. L. Connors, C. Péan, S. Berger, N. Caud, Y. Chen, L. Goldfarb, M. I. Gomis, M. Huang, K. Leitzell, E. Lonnoy, J. B. R. Matthews, T. K. Maycock, T. Waterfield, O. Yelekçi, R. Yu and B. Zhou (eds.)]. Cambridge University Press. In Press.

Legg, T. (2014), Comparison of daily sunshine duration recorded by Campbell–Stokes and Kipp and Zonen sensors. Weather, 69: 264-267. https://doi.org/10.1002/wea.2288

Macara, G., Srinivasan, R. (2018) Groupings and rankings in NIWA's climate reporting. Oral presentation at Meteorological Society of New Zealand 2018 Annual Conference, Christchurch, December 2018.

Meehl, G. A., Tebaldi, C., Walton, G., Easterling, D., McDaniel, L. (2009) Relative increase of record high maximum temperatures compared to record low minimum temperatures in the U.S. Geophysical Research Letters, 36, doi:10.1029/2009GL040736

Ministry for the Environment (2018) Climate Change Projections for New Zealand: Atmosphere Projections Based on Simulations from the IPCC Fifth Assessment, 2nd Edition. Wellington: Ministry for the Environment.

Mol, A., Tait, A. and Macara, G. (2017) An automated drought monitoring system for New Zealand, Weather and Climate 37(1), 23-36.

Mullan, A. B., Stuart, S. J., Hadfield, M. G., Smith, M. J. (2010) Report on the Review of NIWA's 'Seven-Station' Temperature Series. NIWA Information Series No. 78. 175 p.

NIWA (2021a) Climate Summaries. Accessed at https://niwa.co.nz/climate/summaries Date accessed: 29 June 2021.

NIWA (2021b) 'Seven-station' series temperature data. Accessed at https://niwa.co.nz/seven-stations Date accessed: 12 July 2021.

NOAA (2021) Global Climate Report – Annual 2020. Accessed at https://www.ncdc.noaa.gov/sotc/global/202013 Date accessed: 5 October 2021.

Srinivasan, R., Macara, G., Liley, B. (2019) Sunshine duration instrument comparisons in New Zealand.Weather and Climate,39,28-40.

Thompson, C.S (2006) Relative Influence of the Interdecadal Pacific

Oscillation on Drought Occurrence and Severity. Weather and Climate, 26, (2006), 35-66

Trewin, B., Vermont, H. (2010) Changes in the frequency of record temperatures in Australia, 1957-2009. Australian Meteorological and Oceanographic Journal, 60, 113-119.

WMO (2018) Guide to Climatological Practices. 2018 Edition. WMO-No.100.Geneva.ISBN 978-92-63-10100-6.

South Island West Coast orographic rainfall – a polarimetric radar view

J. F. Crouch[1] and F. M. Russell[1]

[1]*Meteorological Service of New Zealand (MetService), P.O. Box 722, Wellington, New Zealand*

Correspondence: john.crouch@metservice.com

Key words: orographic rainfall, polarimetric radar, trapped mountain waves, turbulence as a mechanism to enhance orographic rainfall, Southern Alps

Abstract

This study uses a dual-polarisation C-band weather radar to investigate a period of heavy orographic rainfall about the South Island West Coast on 18 June 2015 when rainfall rates of 20-35+ mm/h were recorded from stratiform rain with no embedded convection. The dual-polarisation imagery clearly shows the location and depth of the melting layer and Dendritic Snow Growth Zone (DGZ), which are both more intense over the mountains, and shows enhancement of rainfall below the melting layer due to collision-coalescence and collectional growth (e.g. seeder-feeder) type effects. Radar doppler radial velocity imagery reveals an embedded trapped mountain wave turbulent layer about 1-2 km thick immediately above the mountains which has not been observed before in New Zealand radar imagery. The moist onshore winds are initially lifted by a low-level barrier jet, then are lifted further above the observed mountain wave turbulent layer providing moisture to the DGZ and enhancing ice growth in this zone immediately above, and slightly upwind, of the mountains. Specific Differential Phase (K_{DP}) imagery reveals an additional ice-growth layer between the DGZ and the melting layer. It is suggested this may be an ice splintering and riming zone, and that the turbulent layer below is producing higher concentrations of super-cooled liquid water leading to enhanced riming in this zone. The turbulent trapped mountain wave layer therefore appears to be an important mechanism in enhancing the surface rainfall by providing additional lift to the onshore airmass, enhancing ice crystal growth aloft and, when combined with warm rain collision-coalescence and collectional growth processes, appears to shift the maximum rainfall upwind towards the first range of mountains.

1. Introduction

The west coast of the South Island is the wettest part of New Zealand with an average annual rainfall of 2,000-3,000mm about the coast, and greater than 8,000 to 10,000mm about the ranges of the Southern Alps (Macara, 2018). Heavy rainfall events are common, and often exceed 100mm in a 24-hour period, with significant spill-over into the headwaters of the main Canterbury and Otago lakes and rivers.

Several New Zealand studies have investigated Southern Alps rainfall, mainly concentrating on the distribution of rainfall across the Southern Alps and spillover into the catchments east of the main divide (e.g., Sinclair et al., 1997, Chater and Sturman, 1998, Henderson and Thompson, 1999, Purdy and Austin, 2003). The largest of these studies was the multi-agency Southern Alps Experiment (SALPEX) in the mid 1990's (Wratt et al., 1996). This was a large multi-faceted study into the influence of the mountains on the distribution of rain

Submitted: 7 September 2021
Accepted: 10 November 2021

and snow fall across the Southern Alps. Observational data was obtained through a combination of local weather stations, rain-gauges, balloon flights, satellite data and research aircraft measurements, but radar observations were limited to an operational MetService C-band single polarisation radar on the Canterbury Plains located about 115 km southeast of the Southern Alps main divide, and two small mobile X-band radars on the West Coast (Purdy et al., 2005).

Of the numerous papers that came from the SALPEX experiment, three are relevant to this study. Sinclair et al. (1997) used rain gauge, radar and atmospheric observations to study a prolonged northwesterly storm which affected the South Island West Coast and Southern Alps in November 1994. During this storm the location and intensity of precipitation varied markedly, mainly dependent on stability. They suggested that in stable blocked northwesterly flows, the ascent and precipitation maxima are shifted upstream of the Southern Alps main divide, while spillover is enhanced during stronger and/or unstable flows as the upstream influence lessens and snow/ice particles drift farther downwind before falling below the freezing level. Revell et al. (2001) modelled the northeast barrier flow which occurs along the West Coast in stable prefrontal northwesterly flows. Their modelling showed that for the case studied, the barrier jet extended offshore and provided a gradual uplift to the onshore flow which extended far enough upstream to enable cloud droplets to grow to drizzle droplets before reaching the more substantial updrafts at the foot of the Southern Alps. They suggested this allows vigorous prefrontal precipitation to occur over the foothills and mountains due largely to warm rain processes. Purdy et al. (2005) used 2 X-band radars to document a seeder-feeder event on the windward side of the Southern Alps where precipitation in the form of snow falling from a cloud sheet aloft enhanced rainfall at lower levels.

More recently, several international studies investigating the microphysical processes associated with orographic rainfall have shown that turbulence plays an important role in increasing surface precipitation by enhancing snow crystal growth aloft. Houze and Medina (2005) used S-band radar data over the Oregon Cascade mountains (USA) and European Alps to show that turbulent cells embedded within a precipitating orographic cloud system made possible a precipitation growth mechanism that would not have been present in a laminar upslope flow. They showed that the turbulent updraft cells create pockets of highly concentrated super-cooled liquid water which leads to increased riming of dendritic snow crystals and flakes falling from above. This produces heavier, more rapidly falling precipitation particles which have a higher probability of reaching the ground upwind of a mountain crest. Without the turbulent cells, condensate would more likely be advected farther up and perhaps even over the mountain range. Geerts et al. (2011) showed similar results from a study of 10 winter storms over the Medicine Bow Range in Wyoming USA. They noted that Doppler vertical velocity transects showed an approximately 1 km deep turbulent layer draped over the terrain which was sometimes clearly distinct from the stratified flow in the free troposphere aloft, and that rapid snow growth was observed within the boundary layer turbulence, especially when it was more intense. They also suggested that boundary layer turbulence may also be important in warm clouds through accelerated growth by collision and coalescence. Grazioli et al. (2015) used a polarimetric X-band radar in the Swiss Alps to observe the polarimetric radar signatures associated with riming and snowfall microphysics. They also investigated the role of turbulence in enhancing snow crystal growth and noted when a turbulent atmospheric layer persists for several hours and ensures continuous super-cooled liquid water generation, riming can be sustained longer and large accumulations of snow at ground level can be generated. Aikins et al. (2016) used a suite of high-resolution radars to study winter orographic storms over the Sierra Madre Range in Wyoming USA. Although cloud liquid water was absent, a turbulent shear layer created by a mid-level cross-barrier jet still enhanced snow growth through deposition and aggregation processes.

This study will use a dual-polarisation C-band weather radar to investigate a South Island West Coast orographic heavy rainfall event on 18 June 2015. This event is of interest as it was a stable stratiform rain event with no embedded convection yet still produced prolonged heavy rainfall rates of 20-30+ mm/h near the radar well upwind of the main divide (similar to the observation made by Sinclair et al. (1997)). The study will show how the radar imagery can be used to identify some of the mesoscale and microphysical processes involved in producing the heavy stratiform rain, and also show the role that trapped mountain waves embedded within the rain-band may be playing in enhancing surface precipitation.

2. MetService Westland weather radar

The New Zealand Meteorological Service (MetService) Westland weather radar is a Vaisala WRM200 dual polarisation C-band Doppler radar. It was installed in November 2011 and is located about 8 km east of Hokitika (Figure 1) at a height of 360 metres above mean sea level (amsl). The radar produces three dimensional scans out to 250 km range every 7.5 minutes. The scans contain 13 elevation angles from 0.5° to 20.0° with a range bin spacing of 200 metres. The lowest radar beams are blocked significantly by the western ranges of the Southern Alps about 15 km east of the radar, which does affect surface rainfall estimates in this area. The radar beams are however unobstructed in this same direction from 3.0° degrees and higher which allows good radar coverage over the Southern Alps from about 1.3 km to 20 km amsl. The radar beams are unobstructed in all other directions from southwest to north-northeast of the radar. This allows excellent radar coverage of weather systems approaching from the west.

The radar produces the following radar fields:

- Reflectivity (horizontal - Z_H) – dependent on the size and density of radar targets.
- Doppler Radial Velocity (V) - Nyquist Velocity

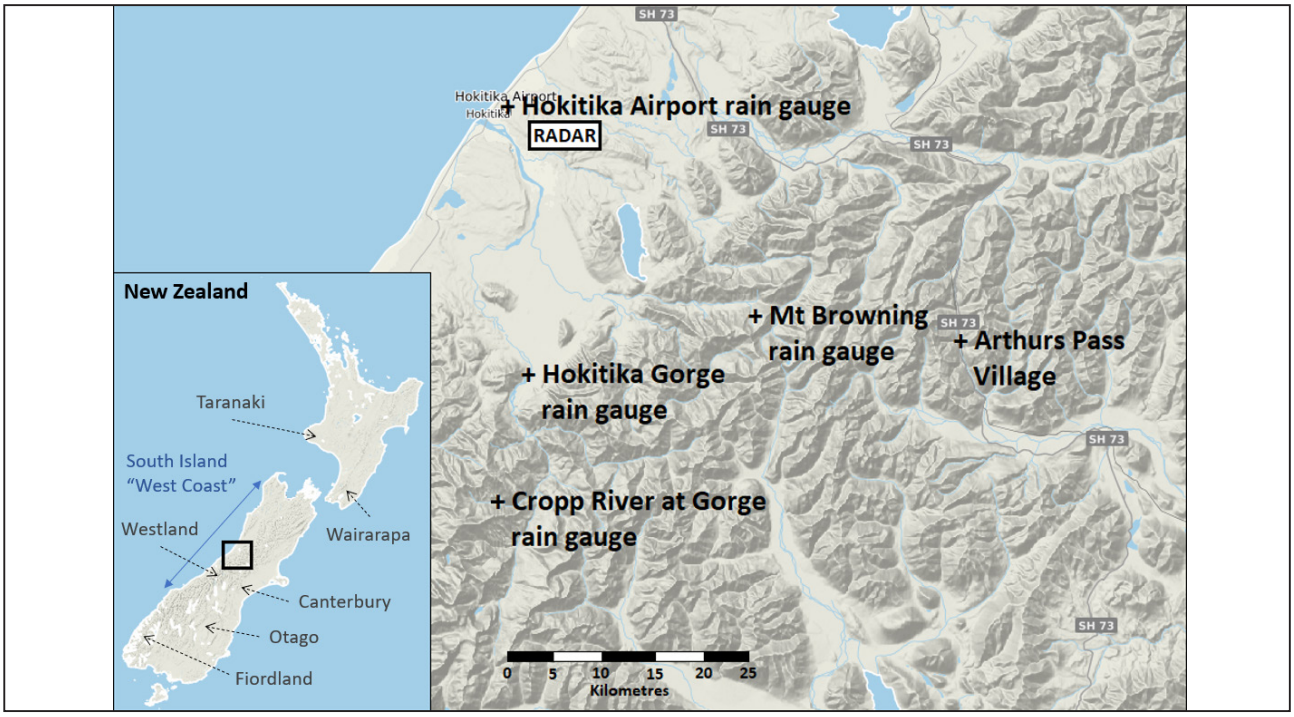

Figure 1: Map showing the study area near Hokitika on the South Island west coast of New Zealand, and locations mentioned in the text. The location of the MetService Westland weather radar (marked as RADAR) and the rain-gauges mentioned in this study are marked on the larger map. The main divide of the Southern Alps lies approximately midway between the Mt Browning rain-gauge and Arthurs Pass village.

is 16 m/s, obtained using dual pulse-repetition-frequencies of 600 and 400Hz. The data can be unfolded in post-processing using Vaisala IRIS radar software.

- Differential Reflectivity (Z_{DR}) – dependent on the shape of a radar target.
- Correlation Coefficient (ρ_{HV}) – a measure of radar target diversity.
- Differential Phase (φ_{DP}) and Specific Differential Phase (K_{DP}) – dependent on the shape and density of radar targets.
- Hydrometeor Classification - A fuzzy logic algorithm which uses the radar fields to classify targets into 5 meteorological and 1 non-meteorological categories.

3. Heavy orographic stratiform rainfall event – 18 June 2015

A major frontal system affected the South Island of New Zealand on 18 and 19 June 2015, bringing heavy rain to the South Island West Coast and Southern Alps, and low-level snow to parts of Canterbury, Otago and Southland. Rain was particularly heavy about Westland and the Southern Alps, with over 500mm being recorded at several stations in the 42 hours between 6am on the 18th and midnight on the 19th NZST (West Coast Regional Council gauges - Cropp River at Gorge 537mm, Mt Browning 533mm and Hokitika Gorge 513mm. Location of gauges shown in Figure 1). This system then brought heavy rain to the lower North Island over the following 2 days with significant flooding of rivers and streams from Taranaki to Wairarapa.

This study will consider the 12-hour period from midday to midnight on 18 June 2015 NZST (18/0000 to 18/1200 UTC) and examine the rainfall near the MetService Westland weather radar sited near Hokitika (Figure 1). This event is of interest as it produced rainfall rates of 20-30+ mm/h from stratiform precipitation with no embedded convection. The heaviest rainfall was observed well upstream of the Southern Alps main divide at the Hokitika Gorge and Cropp River at Gorge gauges, with lesser amounts recorded near the main divide at the Mt Browning gauge.

The heavy rain on the South Island West Coast occurred ahead of a cold front which moved slowly northwards over the South Island during 18 June 2015 (Figure 2).

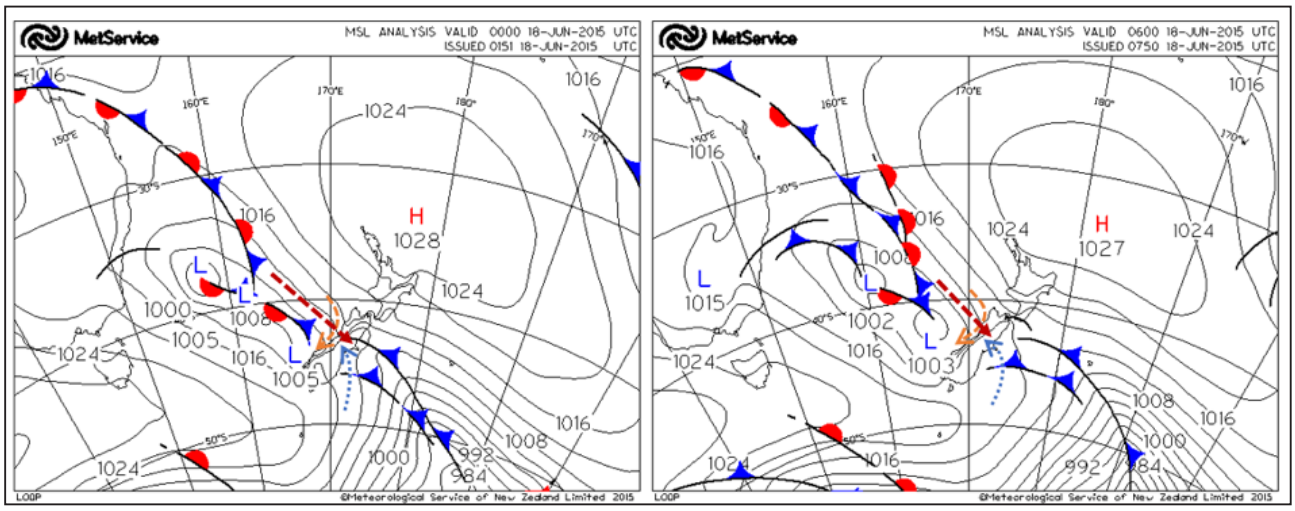

Figure 2: Mean sea level pressure analysis for 00:00 UTC (Midday NZST) 18 June 2015 on left and 06:00 UTC (6pm NZST) 18 June 2015 on right. Dashed arrows indicate wind flow around the South Island of New Zealand - Orange is the low-level northeasterly barrier flow on the West Coast, Red is the deeper northwesterly flow aloft (which crosses the Southern Alps), and Blue indicates a low-level southerly about Canterbury.

A warm, moist, and deep northwesterly airflow overlaid a coastal north to northeasterly barrier flow (Figure 3), and this was associated with a well-defined atmospheric river extending from the Coral Sea (east of Queensland Australia) to the South Island West Coast (Figure 4). A low level northwesterly wind speed maximum of around 26m/s (50kt) was observed over the radar at a height of about 2.5km amsl during the afternoon (Figure 5a), but this later evolved into a better defined, but similar strength, low-level jet centred just above the barrier flow at a height of about 1.5km amsl by early evening (Figure 5b). A tephigram for Hokitika Airport (Figure 6) derived from the MetService 8km WRF model initialised off the US NCEP/GFS global model shows a deeply stable atmosphere with the strongest vertical motion between 1 and 3 km high immediately above the northeast barrier flow. Low level (925-850hPa) wet-bulb potential temperature was around 12°C.

Figure 7 shows a 12-hour gauge corrected radar rainfall accumulation from the MetService Westland radar for the period from midday to midnight NZST (00:00 to 12:00 UTC) 18 June 2015, along with the locations of the MetService Westland radar and the Hokitika Aero, Hokitika Gorge and Mt Browning rain gauges. The image shows a significant enhancement of rainfall just inland from the coast around the radar site, but the rainfall estimates are significantly blocked east of the radar due to terrain and are therefore underestimated in this area. Also depicted on the image is a line showing the transect of vertical radar cross-sections presented in this study.

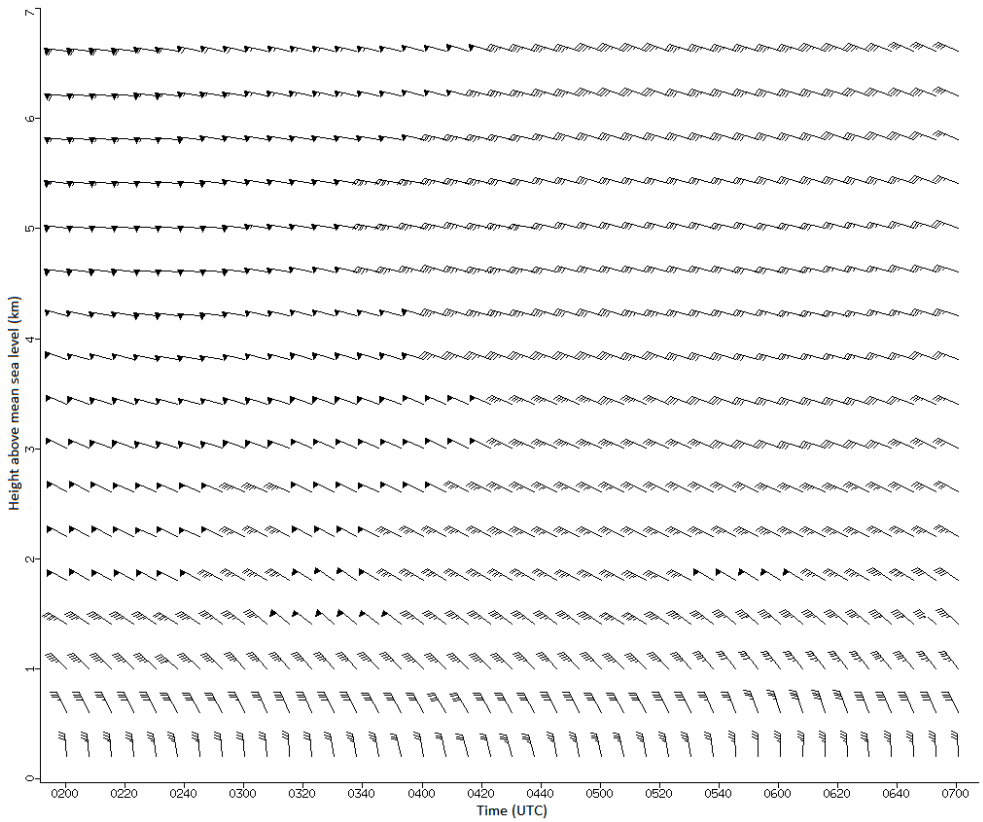

Figure 3: Vertical wind profile derived from the MetService Westland weather radar between 02:00 UTC (2pm NZST) and 07:00 UTC (7pm NZST) 18 June 2015. The wind profiles are calculated every 7.5 minutes using a Volume Velocity Processing technique (Waldteufel and Corbin, 1979), using data within 30km range from the radar. The profile shows a generally deep and uniform northwesterly flow aloft, with winds veering to a strong north to northeasterly barrier flow below 1km. Plotted wind barbs are in knots.

The hourly rainfall intensities and 12-hour rainfall totals for the Hokitika Airport, Hokitika Gorge and Mt Browning rain gauges, along with their height above mean sea level, are shown in Figure 8. These gauges have been chosen as they are located near the MetService Westland radar. The heaviest rain was recorded well upstream, about 20km west of the Southern Alps main divide, at Hokitika Gorge with consistent rainfall rates of 20-30+ mm/h in the 7 hours between midday and 7pm NZST (0000 to 0700 UTC) 18 June 2015. Hourly rainfall rates were less at the Mt Browning gauge located close to the main divide, however both gauges recorded their highest rainfall rates between 5 and 7pm NZST.

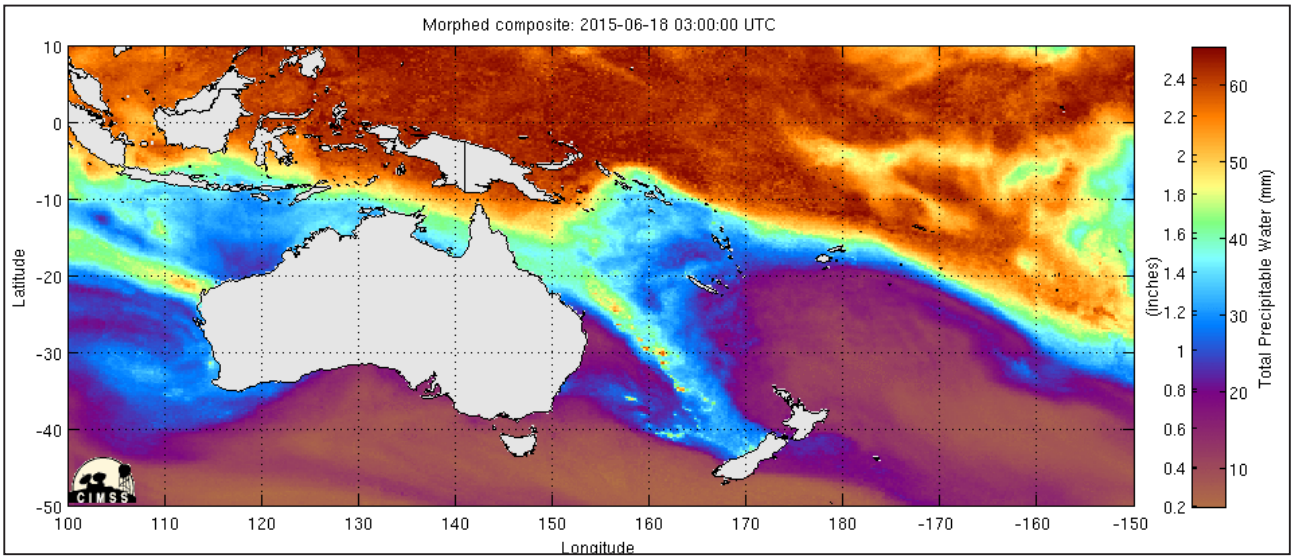

Figure 4: Total Precipitable Water image for 03:00 UTC (3pm NZST) 18 June 2015 from Cooperative Institute for Meteorological Satellite Studies (CIMMS) showing an atmospheric river (of moisture) extending from the Coral Sea onto the South Island of New Zealand.

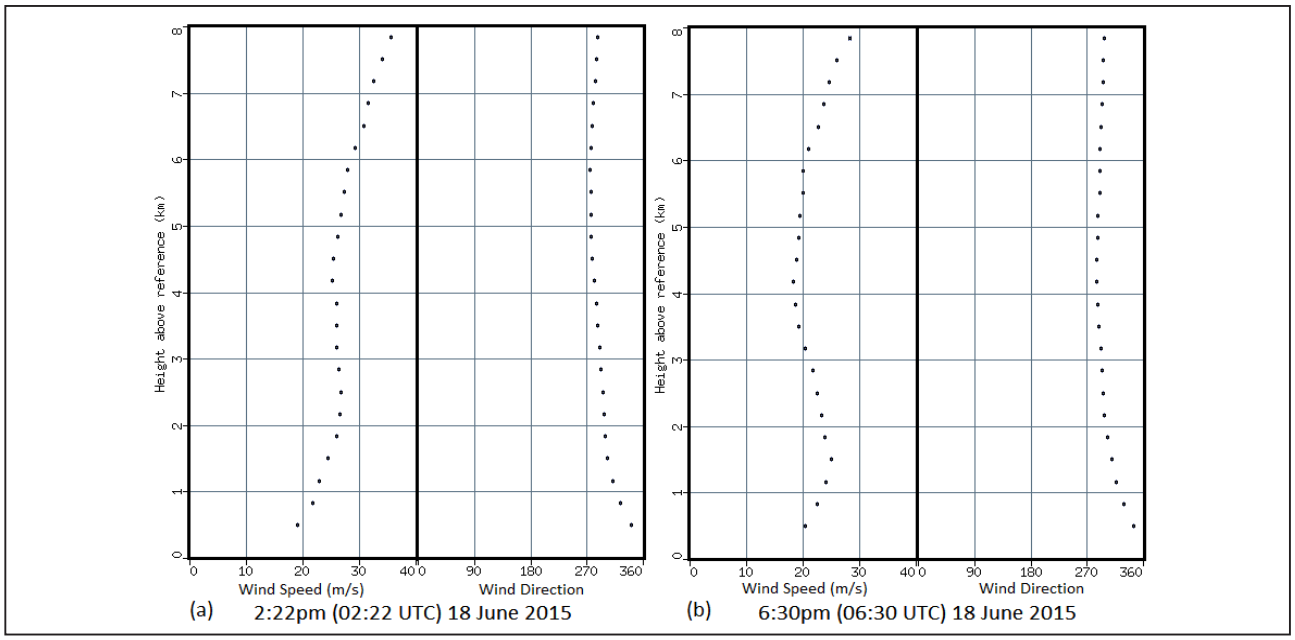

Figure 5: Vertical profile of wind speed and direction derived from the MetService Westland weather radar at (a) 02:22 UTC (2:22pm NZST) and (b) 06:30 UTC (6:30pm NZST) 18 June 2015. The profiles are calculated using a Volume Velocity Processing technique (Waldteufel and Corbin, 1979), using data within 30km range from the radar.

4. Polarimetric radar cross-sections

Radar vertical cross-sections for two times, approximately three hours apart, during the period of heavy rain between midday and midnight (NZST) on 18 June 2015 will now be discussed. This period is of interest as very heavy rainfall rates were recorded from stratiform rain with no embedded convection, and the heaviest rain recorded was about 20km upwind of the main divide at the Hokitika Gorge gauge. The cross-sections are all along the same line which is orientated in a northwest to southeast direction (see Figure 7), and this is chosen to align with the prevailing northwest flow aloft (see Figures 3 and 5). The radar cross-sections pass through Hokitika (northwest of the radar) and Arthurs Pass village (southeast of the radar), which are both marked on the imagery. The cross-sections extend to 60 km away from the radar in both directions, extend from sea level up to 10 km high, and are overlaid with a terrain profile.

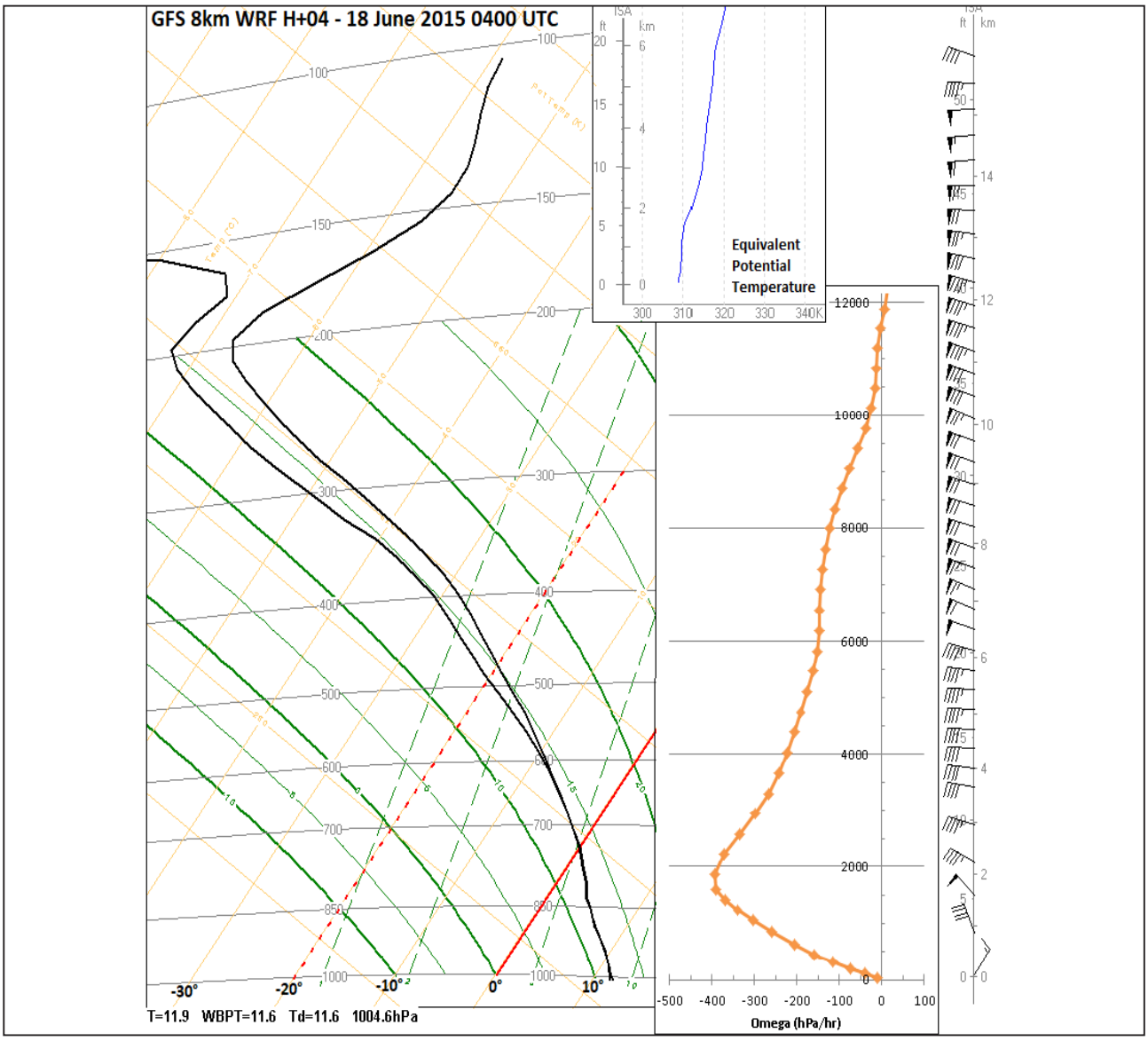

Figure 6: Model tephigram and vertical profiles for Hokitika Airport at 4pm (04:00 UTC) 18 June 2015 derived from the MetService 8km WRF model initialised off the 18/0000 UTC US NCEP/GFS global model. Orange lines orientated from top-right to bottom-left are isotherms; orange lines from top-left to bottom-right are dry adiabats; solid dark-green curves are saturated adiabats. The Equivalent Potential Temperature graph increases with height indicating a deep stable airmass. Vertical motion (omega) up to 12 km high is also shown and peaks around 2 km high. Wind barbs are in knots.

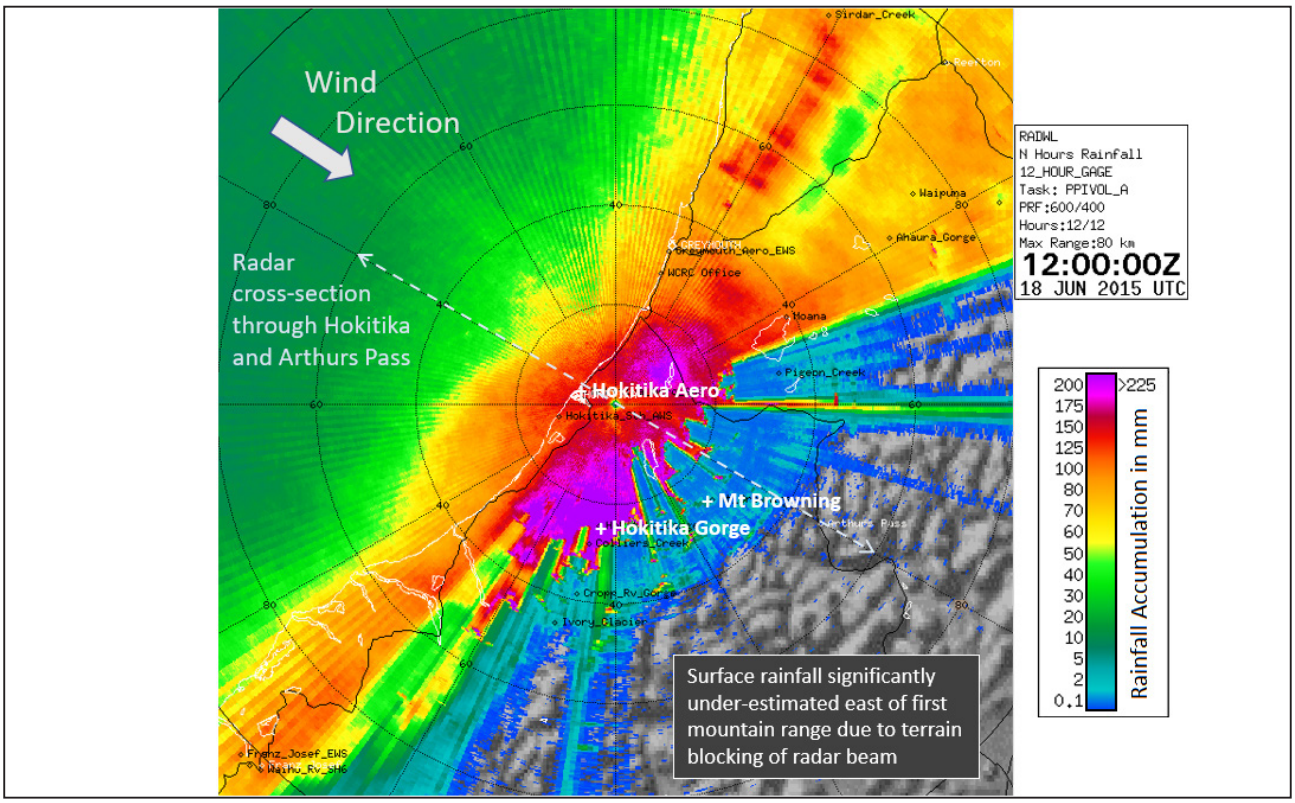

Figure 7: Gauge corrected radar rainfall accumulation from the MetService Westland radar for the 12-hour period from 00:00 UTC (Midday NZST) to 12:00 UTC (Midnight NZST) 18 June 2015. Radar reflectivity from the lowest clutter-free bin is used, using a Vertical Profile of Reflectivity correction to obtain the reflectivity at a fixed reference height of 0.1 km. Locations of the three rain-gauges in figure 8 are shown, as is the transect of the radar cross-section shown in figures 9, 10, 12 and 13.

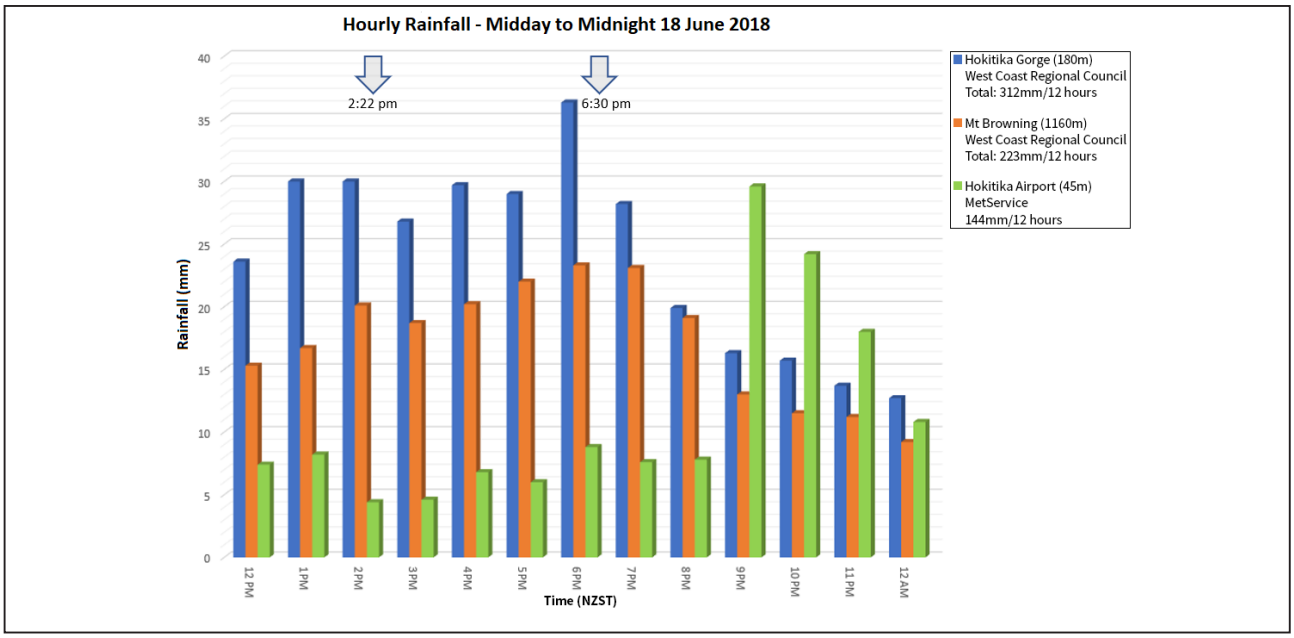

Figure 8: Hourly rainfall data for three gauges near the MetService Westland radar for the 12-hour period from midday to midnight NZST (00:00 to 12:00 UTC) 18 June 2015. The locations of the gauges are shown in figures 1 and 7. Hokitika Airport is near the coast, Hokitika Gorge is about midway between the coast and the main divide of the Southern Alps, and Mt Browning is an alpine station close to the main divide. The owner of the station and its height above sea level are included in the key. The times of the two radar vertical cross-sections discussed in section 4 are shown. The heavy rain recorded at Hokitika Airport around 9pm was associated with a shallow easterly wind change and is not discussed in this study.

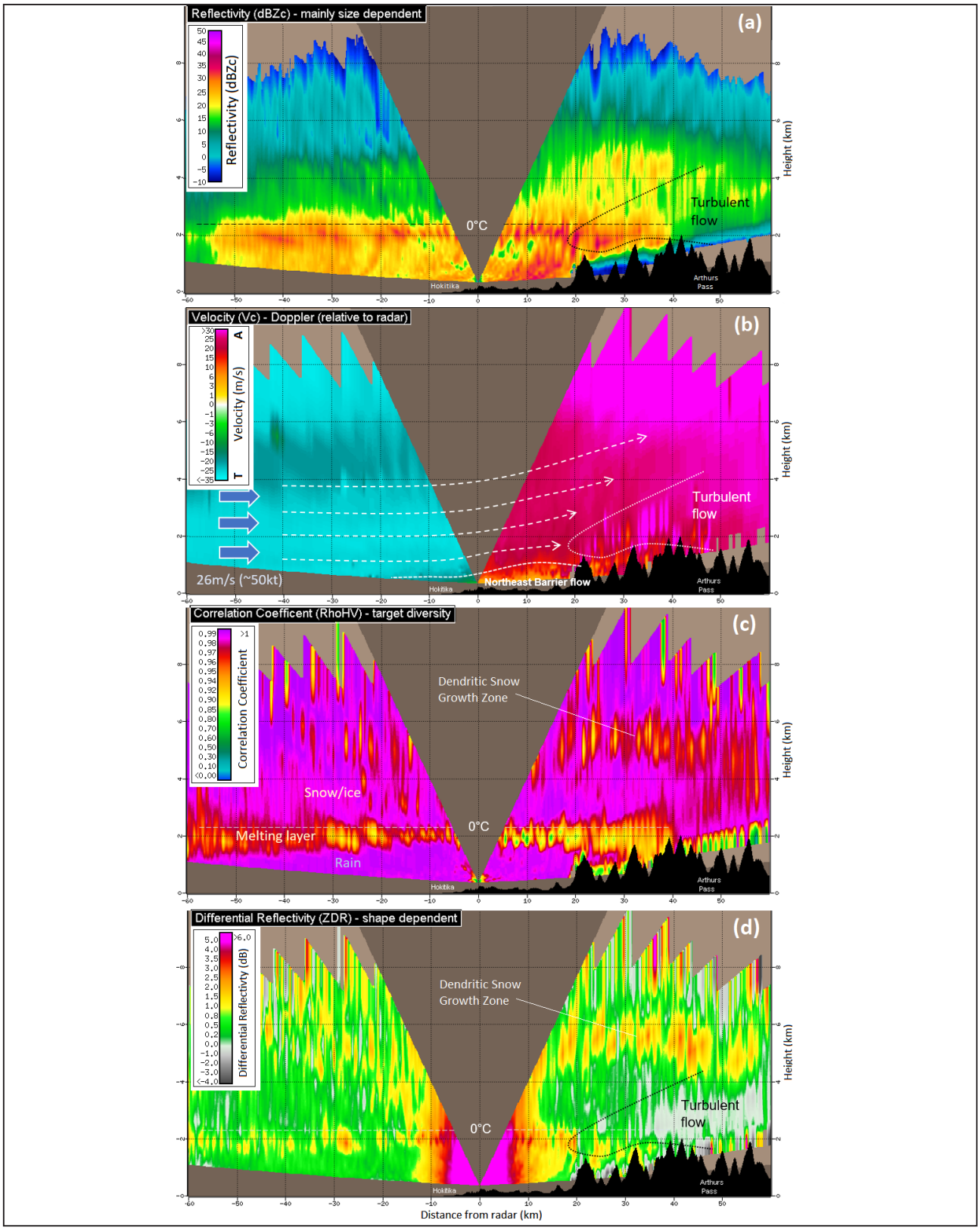

Figure 9: Westland radar vertical cross-sections at 02:22 UTC (2:22pm NZST) 18 June 2015. The 4 radar fields are (a) Horizontal Reflectivity (dBZ) corrected for attenuation, (b) Unfolded Doppler Radial Velocity (m/s), (c) Correlation Coefficient (unit-less), and (d) Differential Reflectivity (dB). The transect of the cross-section is shown in figure 7. The 0°C height is estimated from a combination of the radar imagery and the tephigram shown in figure 6.

4.1. Radar Cross Sections at 02:22 UTC 18 June 2015

During the afternoon of 18 June 2015, rainfall rates of 25-30mm/h were recorded at Hokitika Gorge, while around 20mm/h was recorded at Mt Browning. Figure 9 shows a combined radar vertical cross-section at 02:22 UTC (2:22pm NZST) which is representative of the rainfall during this period. The cross-section shows four radar fields, (a) the horizontal Reflectivity (Z_H) corrected for attenuation, (b) the unfolded Doppler Radial Velocity (V_C), (c) the Correlation Coefficient (ρ_{HV}) and (d) the Differential Reflectivity (Z_{DR}) fields. The imagery shows stratiform precipitation only with no embedded convection. The estimated height of 0°C is marked on the imagery.

The melting layer shows as a band of enhanced reflectivities (~30 dBZ) known as the radar bright-band (Rinehart, 2010) just below 0°C in the reflectivity image (Figure 9a), but is better defined in the Correlation Coefficient field (Figure 9c) as a layer of reduced ρ_{HV} values (~0.75 to 0.95) and in the Differential Reflectivity field (Figure 9d) as a zone of enhanced Z_{DR} values (~1.0 to 3.0 dB). The melting layer is the region where falling ice crystals and snowflakes melt to raindrops. As the snowflakes melt, they first acquire meltwater on the outer portions of the flakes which leads to an increase in reflectivity (Z_H). After further melting, the snowflakes collapse and become more oblate in shape before breaking up into individual and less oblate raindrops. It is this increasing oblateness during the melting process which produces the zone of larger positive Differential Reflectivity values (Kumjian, 2013). Also, as they melt, there is a mix of ice and snow, melting ice and snow, and fully melted raindrops within the melting layer which produces the zone of reduced Correlation Coefficient values (Kumjian, 2013). This mix of radar targets is greatest in the lowest half of the melting layer, which shows as reduced values of Correlation Coefficient (ρ_{HV} ~0.75 to 0.85) in Figure 9c. Note that the depth of the melting layer generally appears to increase with distance from the radar in the Correlation Coefficient field, but this is due to the radar beams increasing in width at greater range and passing through the melting layer at a shallower angle which gives the incorrect appearance of a deeper melting layer further from the radar. Despite this, there is some evidence in both the Correlation Coefficient and Differential Reflectivity cross-sections of a deeper melting layer east of the radar under the stronger reflectivity echoes aloft which will be mainly due to downward penetration of snow in heavier precipitation, but also an above-mountain turbulent layer, as seen in Figure 9b and discussed later in this section, which may be throwing partially melted snow and ice crystals a little above the general melting level. The Correlation Coefficient image (Figure 9c) shows the melting layer depth to be about 500 metres west of the radar, and about 1km (or more) east of the radar in the heavier precipitation over the mountains. There are also lower ρ_{HV} values within the melting layer east of the radar indicating more target diversity and possibly larger aggregated snowflakes taking longer to melt and falling to a lower height (Kumjian, 2013).

The next zone which is easily observable is the Dendritic Snow Growth Zone (DGZ) at about 5-6km high. The DGZ is the region where the growth of dendritic snow crystals occurs and maximises between about -13°C and -17°C (Stoelinga et al., 2013). This generally occurs in regions of strong upward motion. The DGZ is characterised in the Correlation Coefficient field as a zone of reduced ρ_{HV} values (~0.90 to 0.98), and in the Differential Reflectivity field as a zone of increased positive values of Z_{DR} (~1.0 to 3.5 dB). These signatures are due to the rapid growth by deposition of planar or dendritic snow crystals within the zone (Kennedy and Rutledge 2011, Andric et al. 2013, Kumjian 2013). Within and below the DGZ, reflectivity (Z_H) generally increases rapidly as the snow crystals fall out and aggregate into larger snowflakes (Kumjian 2013). Previous studies (Kennedy and Rutledge 2011, Bechini et al. 2013) have noted that these dual-polarisation radar

signatures observed around -15°C (i.e. reduced ρ_{HV} and enhanced Z_{DR}) correlate well with increased reflectivity, and precipitation rates, at the surface.

In the cross-sections (Figures 9c and 9d), the Dendritic Snow Growth Zone (DGZ) is particularly enhanced east of the radar over the mountains where the vertical motion is likely to be strongest (due to orographic lifting) compared to weaker signals over the sea west of the radar where vertical motion will be much weaker. These strong DGZ signatures aloft correlate well with increased reflectivity at lower levels, and the rapid increase in reflectivity within and immediately below the DGZ will be associated with aggregating snow crystals (Kumjian 2013). This all indicates that the growth of dendritic snow crystals is much stronger over the mountains and is likely to be one important mechanism in producing heavy precipitation at the surface. Interestingly, there is still a good Dendritic Snow Growth Zone signature east of the main divide (near Arthurs Pass village), although it does appear to lower in height. This suggests that significant numbers of dendritic snow crystals are still being produced aloft just east of the main divide and contributing to the production of "spill-over" precipitation by drifting downwind and falling farther east.

The radial velocity image (Figure 9b) is an unfolded Doppler wind field, and the cross-section is aligned with the prevailing northwest flow. Winds are shown relative to the radar with winds towards the radar on the left (negative values) and away from the radar on the right (positive values). Upwind of the radar (over the Tasman Sea), the northwest winds are strong and appear fairly uniform below about 4km, however the radar derived vertical wind profile in Figure 5a shows a wind speed maximum of about 50 knots (26m/s) over the radar at 2.5km amsl with slightly decreasing speed immediately above. The imagery also shows a low-level northeast barrier flow (indicated by reduced Doppler radial wind values due to the cross-wind component of the barrier flow) extending up to about 1.5km high and extending over the coastal hills up to the first range of mountains about 20km east of the radar. There is also evidence of the barrier flow west of the radar but at a shallower height which dips below the radar beam offshore. It is interesting to note that the depth of the barrier flow does appear to be about twice as deep over the land east of the radar as it is near the coast.

Figure 10 shows a comparison between the raw radial velocity and the unfolded radial velocity cross-sections, taken along the same transect as Figure 9b. Although the strong northwest flow aloft is folded in the raw radial velocity cross-section (Figure 10a), and hence the towards/away winds are incorrect, the northeast barrier flow is depicted correctly and shows up well as a shallow layer below about 1km west and 1.5km east of the radar. Also evident in Figure 10a is a shallow turbulent layer along the top of the barrier flow which will be due to wind shear between the northeasterly winds in the barrier flow and the stronger onshore northwesterlies aloft.

More significantly, the Doppler radial velocity imagery (Figures 9b and 10a/b) shows a regularly-spaced variation in the velocity field immediately above the mountains to a depth of about 1-2km, which is similar to observations made by Houze and Medina (2005) over the European Alps (see also Rotunno and Houze, 2007). This is considered to be a turbulent flow generated by mechanical turbulence over the ranges. Note however, that in the unfolded velocity imagery (Figures 9b and 10b) the stronger "away" velocities showing within this turbulent flow are probably being incorrectly unfolded by the Vaisala IRIS software, and it may be depicted better in the raw radial velocity cross-section (Figure 10a). This is due to the software basing the unfolding on the vertical wind profile at the radar, which is all northwesterly, and assuming the same relative wind direction elsewhere. To explain the likely reason for this turbulence, consider the tephigram in Figure 6 which shows a deeply stable atmosphere, and the radar derived wind profile at 2:22pm in Figure 5a which shows a wind maximum of

about 26m/s (50kt) at 2.5km height above the radar and slightly decreasing wind speed above. Combined with the observed depth of the turbulent layer and the regular pattern in the Doppler Radial Velocity image (Figures 9b and 10), this suggests that the vertical shear associated with the observed wind maximum in Figure 5a is creating standing gravity waves over the mountains and these are likely to be trapped mountain waves (COMET, 2016). These trapped mountain waves, as observed at 02:22 UTC (Figures 9b and 10), are initially produced by the first range of mountains, then become complex over successive ranges, and increase in height over the higher terrain up to the main divide. Above this turbulent trapped mountain wave layer, the northwest flow appears more laminar. The imagery also shows that the onshore northwest winds are lifted initially over the coastal barrier flow, confirming early modelling on barrier jets done by Revell et al. (2001) using 1996 SALPEX data, then appear to be lifted further over the mountain induced turbulent flow. This suggests the trapped mountain waves may be providing extra lift to the onshore winds and increasing the vertical motion upwind of the higher terrain.

The horizontal extent of the turbulent layers, as observed by the radar, is shown in Figure 11 which shows both the 2.0 degree raw (folded) and unfolded Doppler radial velocity PPI (Plan Position Indicator) imagery at 02:24 UTC. This 2.0 degree radar beam passes approximately

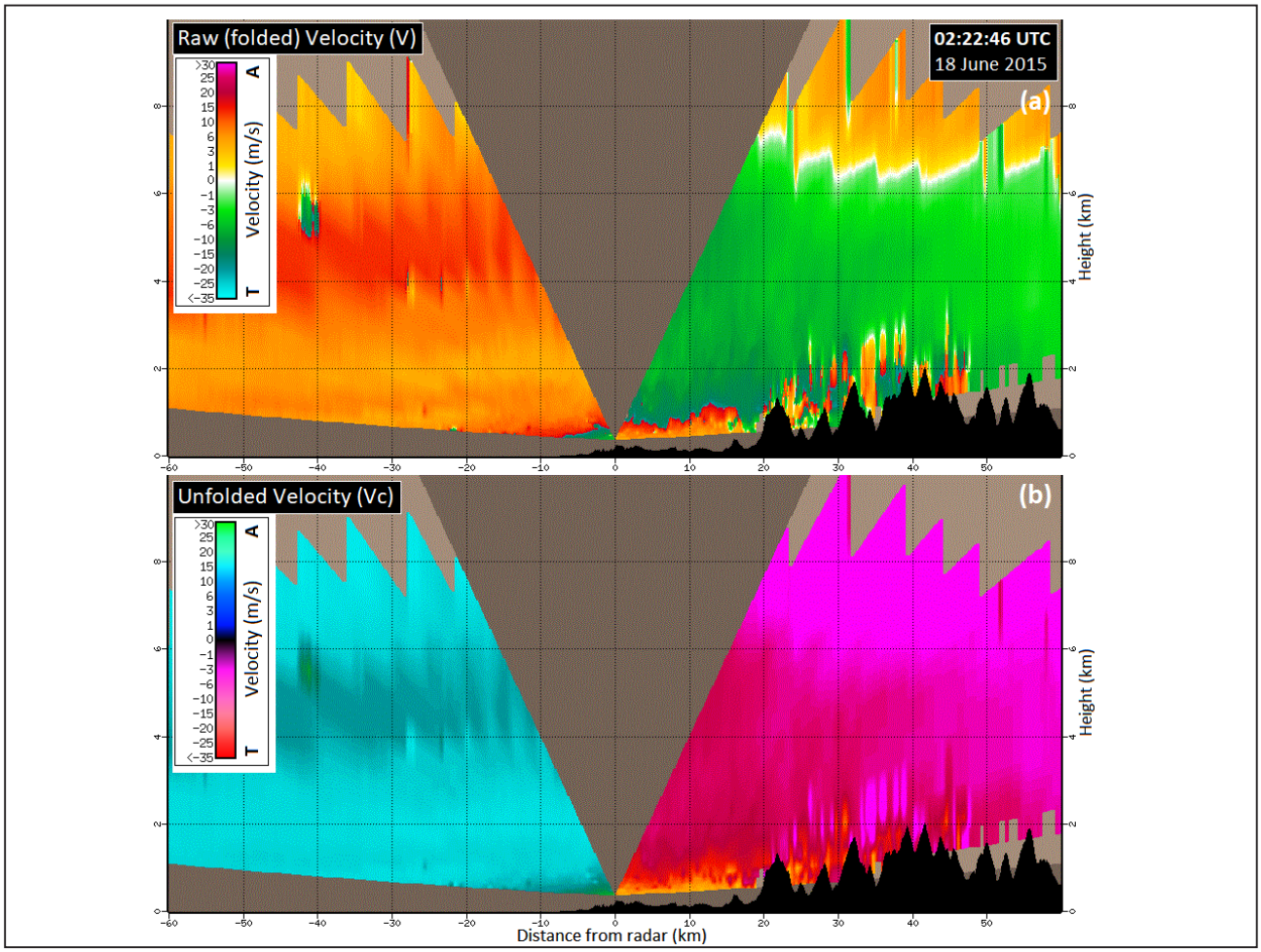

Figure 10: Vertical cross-sections showing the corresponding (a) raw and (b) unfolded Doppler Radial Velocity fields for the same time (02:22 18 June 2015 UTC), and along the same transect, shown in figure 9. The velocity data is unfolded using Vaisala IRIS software. Due to the strong northwest flow aloft, and a radar Nyquist Velocity of 16m/s, most of the data above the low-level northeast barrier in the raw velocity field is folded, and then corrected in the unfolded velocity field. Data within the turbulent layer over the mountains, however, is probably incorrectly unfolded by the software due to the complicated nature of the turbulence. On the scale bar, T indicates "towards radar" velocities, and A indicates "away from radar" velocities.

along the top of the barrier flow east of the radar and through the centre of the turbulent layer over the mountains. A shear turbulent layer, generated by vertical wind shear between the northeast barrier flow and the stronger onshore northwest flow aloft, shows in both images as a set of approximately parallel lines just east of the radar. Immediately downwind of this, the mechanical turbulent layer over the mountains shows as a broad zone of mixed towards and away velocities in the raw velocity field (Figure 11a) and as a broad zone of strong variable away velocities in the unfolded velocity field (Figure 11b). As mentioned above however, the velocities within this zone are probably being unfolded incorrectly by the software. The mechanical turbulent layer appears very noisy in the PPI imagery due to the complex nature of the turbulence and the underlying terrain but does show a more wave-like structure in the vertical radial velocity cross-sections (Figure 10) discussed earlier. This mechanical turbulent layer was observed on both the PPI and cross-section imagery to be persistent though the whole period of heavy rain during the afternoon and evening of 18 June 2015. It consistently extended over the main divide towards Arthurs Pass village, but at times did vary in intensity and often extended well east of the main divide of the Southern Alps. Note however, that at 02:24 UTC (Figure 11), it is possible the 2.0 degree radar beam may be overshooting any lower waves east of Arthurs Pass due to the increasing height of the beam with range, and lower elevation beams from the Hokitika radar are unable to detect them due to terrain blocking.

The reflectivity image (Figure 9a) shows an increase in reflectivity below the melting layer and within the barrier flow (about 10-20km east of the radar) which results in enhanced surface rainfall. This enhancement is likely the result of a collectional growth (or seeder-feeder) type mechanism where falling precipitation collides and coalesces with smaller cloud droplets within the moist barrier flow (Houze, 2012, Stoelinga et al., 2013). Stoelinga et al. (2013) notes this often occurs in cases with a high melting layer, and Figures 9a/c/d show the melting layer to be around 2-3km high in this area. A similar

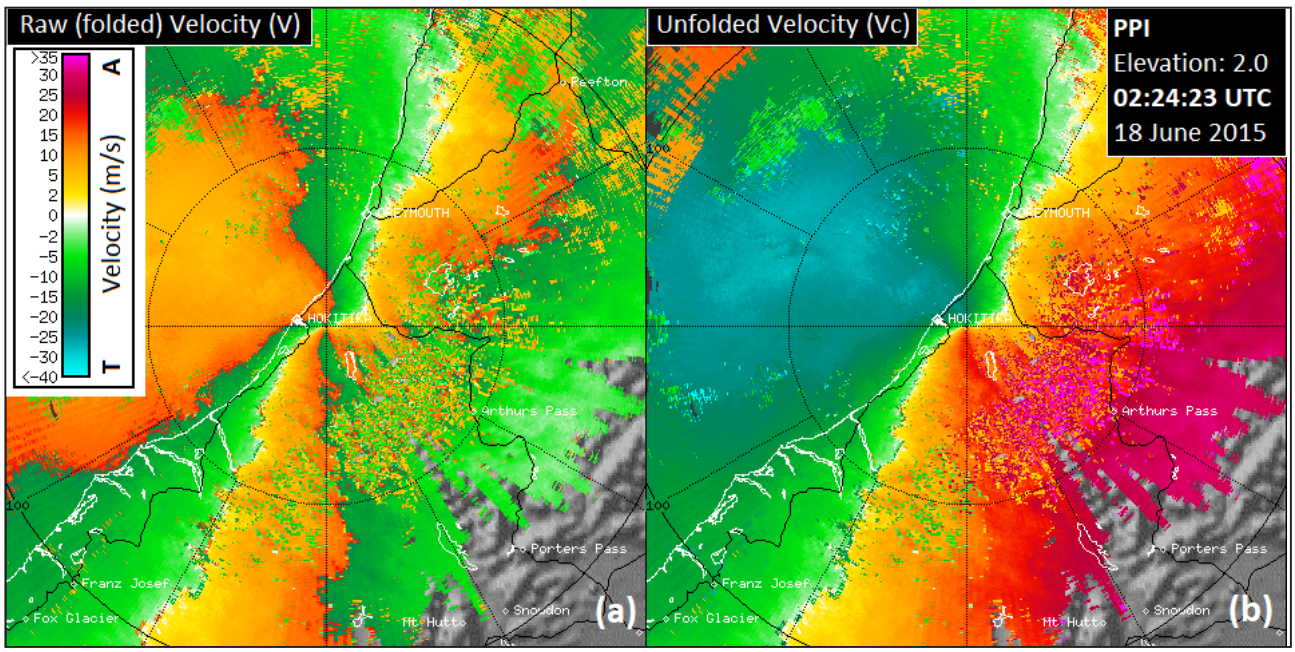

Figure 11: 2.0 degree Plan Position Indicator (PPI) images showing (a) raw Doppler Radial Velocity and (b) unfolded Doppler Radial Velocity at 02:24 18 June 2015 UTC. The velocity field is unfolded using Vaisala IRIS software. Most of the data is considered to be correctly unfolded by the software, however the data within the broad turbulent zone observed over the mountains is probably incorrectly unfolded due to the complicated nature of the turbulence. On the scale bar, T indicates "towards radar" velocities, and A indicates "away from radar" velocities. Range rings are shown at 50km and 100km from the radar.

seeder-feeder enhancement was observed by Purdy et al. (2005) with X-band radars on the South Island West Coast during the 1996 SALPEX experiment (Wratt et al, 1996), however their study involved a more classical seeder-feeder type event where snow falling from a separate system aloft fell into a lower shallow raining cloud system.

4.2. Radar Cross Sections at 06:30 UTC 18 June 2015

Figure 12 shows the same radar cross-sections as in Figure 9 but at 06:30 UTC, while Figure 13 shows in more detail the raw and unfolded radial Doppler velocity cross-sections. The imagery in Figure 12 again clearly shows the melting layer at 2-3km high and the Dendritic Snow Growth Zone (DGZ) around 5-7km high over the mountains, but it also shows several significant changes from the previous time, most of which can be attributed to changes in the structure of the onshore northwesterly flow. In the Doppler radial velocity imagery, the previous cross-sections at 02:22 UTC (Figures 9b and 10a/b) and the associated wind profile in Figure 5a showed a slight wind speed maximum about 2.5km high, but at 06:30 UTC (Figures 12b and 13a/b), this has now changed to a better-defined low-level jet of around 50kt (26m/s), centred about 1km high over the sea west of the radar. The northeast barrier flow is still well marked up to about 1.5km height east of the radar up to near the first range of mountains, and there is still a strong trapped mountain wave turbulent layer downstream of the first range of mountains which increases in height from about 2km high to about 4km high over the area just east of the main divide above Arthurs Pass village. This mountain wave turbulent signature appears to be stronger and better defined than at 02:22 UTC. The low-level jet can also be observed being lifted to higher elevations above the barrier flow and over the mountains. This is presumably transporting significant amounts of low-level moisture up into the riming and aggregation zones, and may also be creating a stronger mountain wave turbulent layer due to the greater vertical wind shear and reduction in cross-barrier flow above the ascending jet (COMET, 2016). Also observable on the Doppler radial velocity images (Figures 12b and 13) is a shallow cold easterly flow (marked by the right arrow in Figure 12b) which has moved across the Southern Alps main divide from Canterbury. Note however, that due to incorrect assumptions made by the velocity unfolding software, this easterly wind in the unfolded imagery (Figures 12b and 13b) is shown as a positive "away" wind rather than a negative "towards" wind.

In Figure 12, both the melting layer and Dendritic Snow Growth Zone (DGZ) are about 500 m higher than at 02:22Z indicating a warming of the airmass. The Correlation Coefficient and Differential Reflectivity imagery (Figures 12c and 12d) also show a sharp lowering of the melting layer over the mountains about 35km east of the radar associated with the much colder easterly flow advecting across the Southern Alps from Canterbury where snow was falling to low levels over the Canterbury Plains. This is a good example of a warm advection snowfall event where a shallow layer of much colder denser air is undercutting a deep warm moist layer aloft (Neale and Thompson, 1977, MetService, 2015).

The strongest DGZ and reflectivity signatures aloft in Figure 12 are generally further east than at 02:22 UTC, however there is still a good DGZ signature showing in both the Correlation Coefficient and Differential Reflectivity images (Figures 12c and 12d) above, and slightly upwind of, the first range of mountains. The area of enhanced reflectivity (20-25 dBZ) between about 4 and 6 km high (30 to 50 km east of the radar) will be associated with aggregating snowflakes, while the lower area of enhanced reflectivities (20-30 dBZ) between 3 and 4 km high (and extending out to about 35 km east of the radar) will be due to riming and aggregation (Andric, et al., 2013). This lower enhanced reflectivity area lies within the ascending low-level jet, and near the top of the

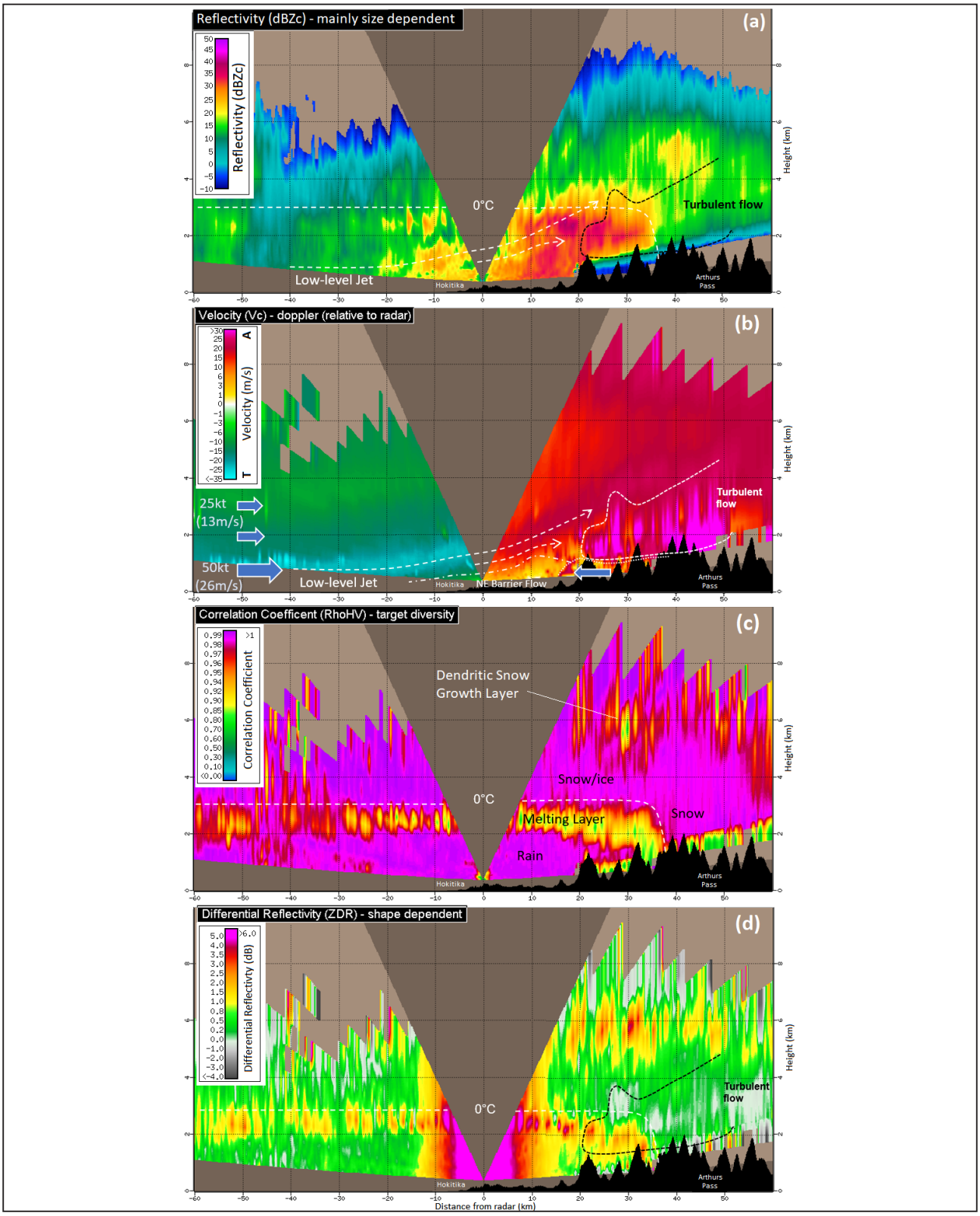

Figure 12: Westland radar vertical cross-sections at 06:30 UTC (6:30pm NZST) 18 June 2015. The four radar fields are (a) Horizontal Reflectivity (dBZ) corrected for attenuation, (b) Unfolded Doppler Radial Velocity (m/s), (c) Correlation Coefficient (unit-less), and (d) Differential Reflectivity (dB). The transect of the cross-section is shown in Figure 7. The 0°C height is estimated from a combination of the radar imagery and the model tephigram shown in Figure 6.

turbulent layer, and it is likely that there are significant amounts of super-cooled liquid water in this region causing strong riming (Grazioli, 2015).

Below the melting layer, in the area about 10-20 km east of the radar, there is a deep layer of enhanced reflectivities (30-40dBZ, Figure 12a) extending from the melting layer to the surface that will be associated with very heavy rain. This is the heavy rain that affected the Hokitika Gorge rain gauge around this time when rainfall rates in excess of 30 mm/h were recorded (Figure 8). This region of observed heavy rain lies within both the warm part of the ascending low-level jet and the northeast barrier flow suggesting the enhancement is due to a strong collision-coalescence and/or collectional growth (or seeder-feeder) type affect as falling precipitation generated aloft collides with smaller cloud or drizzle droplets advected into this area below the melting layer.

5. 6.0° PPI Radar Imagery – 06:30 UTC 18 June 2015

To get a better understanding of the microphysical processes producing the heavy orographic rain, we can look at an individual radar beam that slices through the all the zones identified in the cross-sections discussed in section 4. Figure 14 shows the position of the 6.0° beam on the 06:30 UTC cross-section discussed in section 4.2. The radar beam lies near the path of the ascending low-level jet below the melting layer, then lies near the top, or just above, the embedded mountain wave turbulent layer at higher elevations. Figure 15 shows the 6.0° PPI (Plan Position Indicator) imagery for four radar fields at 06:30Z. In this type of imagery, layers of constant elevation show as circular rings.

In Figure 15, the melting layer is well defined just below

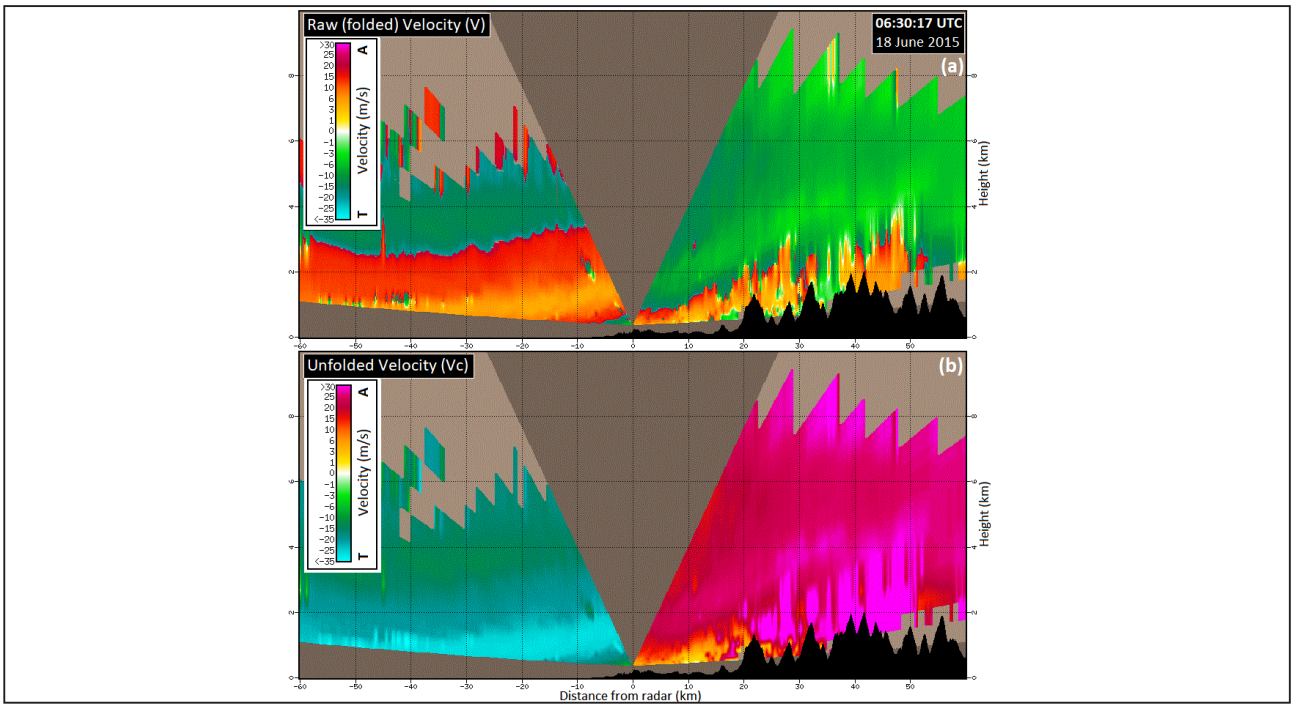

Figure 13: Vertical cross-sections showing the corresponding raw (top) and unfolded (bottom) Doppler Radial Velocity fields for the same time (06:30 18 June 2015 UTC), and along the same transect, shown in figure 12. The velocity data is unfolded using Vaisala IRIS software. Due to the strong north-west flow aloft, and a radar Nyquist Velocity of 16m/s, much of the data above the low-level northeast barrier in the raw velocity field is folded, and then corrected in the unfolded velocity field. A shallow easterly wind change moving through the mountains east of the radar has been incorrectly un-folded by the software and is shown correctly in the raw velocity image. Data within the turbulent layer over the mountains is also probably incorrectly unfolded by the software due to the complicated nature of the turbulence. On the scale bar, T indicates "towards radar" velocities, and A indicates "away from radar" velocities.

0°C as a ring of enhanced reflectivities of around 30 to 40 dBZ (the radar bright band) on the reflectivity image (Figure 15a), a ring of reduced values of around 0.75 to 0.95 in the Correlation Coefficient image (Figure 15b), and a ring of enhanced positive Differential Reflectivity values of around 1.0 to 3.0 dB (Figure 15c). The other area of very high Differential Reflectivities below the melting layer and near the radar is noise from an unknown systematic bias. Similarly, on the Specific Differential Phase image (Figure 15d) the large area of negative KDP values near the radar is also considered to be noise from an unknown systematic bias and is masking any melting layer signals.

The Dendritic Snow Growth Zone (DGZ) is well defined in the zone between -10° and -20°C over the land (likely maximising around -13° to -17°C, Stoelinga et al., 2013), and is particularly strong over the mountains east of the radar due to the strong vertical motion from orographic lifting and moisture transported into this region by the ascending onshore flow (as discussed in section 4.2). The DGZ is observed as an outer ring of reduced Correlation Coefficient values (ρ_{HV} ~ 0.95), and enhanced positive values of both Differential Reflectivity (Z_{DR} ~ 1.0 to 3.0 dB) and Specific Differential Phase (K_{DP} ~ 1.0 to 2.0 deg/km). The ρ_{HV}, Z_{DR} and K_{DP} rings are co-located, and the maximum values of the outer K_{DP} ring generally lies just below the Z_{DR} maximum. Reflectivity (Z_H) increases from about the middle of the DGZ towards the ground suggesting the aggregation of dendritic snow crystals in the lower part of the Dendritic Snow Growth Zone. These observations are consistent with the findings of others (e.g. Andric 2013, Schrom 2015). Interestingly, the DGZ does not appear to be perfectly circular which indicates its height varies. This is likely related to changes in the strength of the vertical motion due to terrain effects which may be altering the temperature structure within the cloud system over the mountains.

Of significant interest is a third zone of strongly enhanced KDP values showing between about -5°C and -10°C on the Specific Differential Phase image (Figure 15d). This zone is associated with a slight enhancement of Z_{DR} values and a slight reduction in ρ_{HV} values. There is also a decrease in reflectivity Z_H values within this zone, but they do increase again immediately below it. This

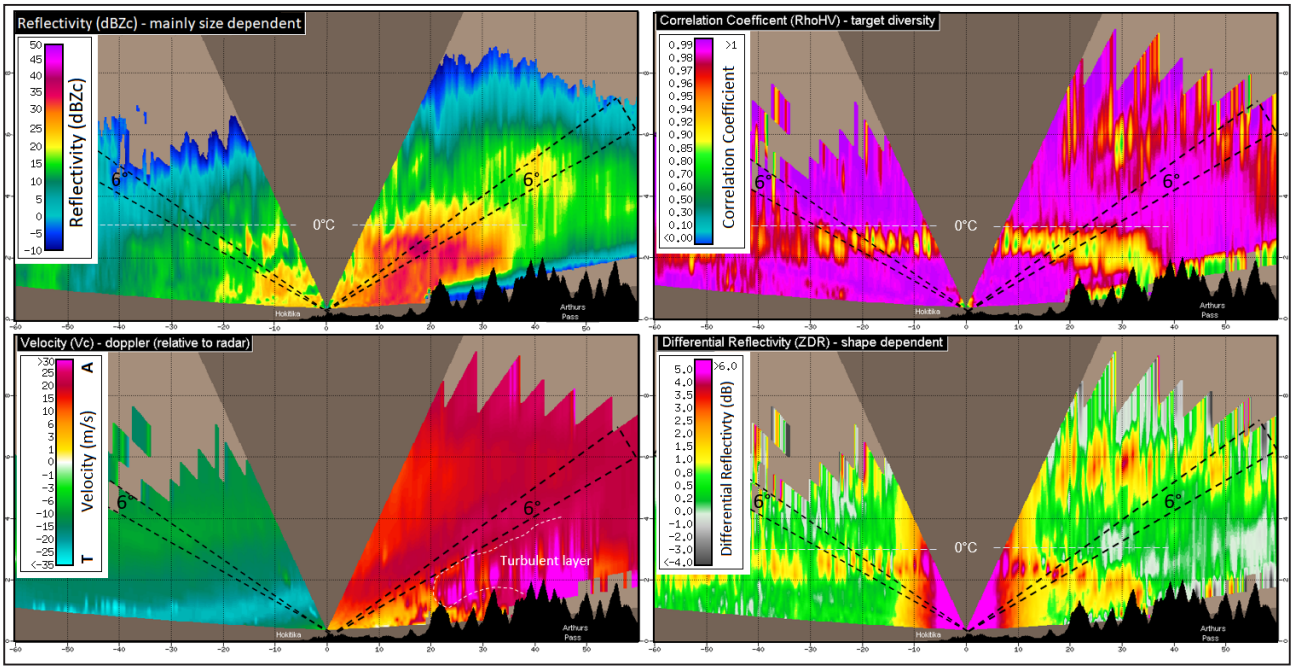

Figure 14: Westland radar vertical cross sections for 06:30 UTC 18 June 2015 (same as figure 12) showing the position of the 6.0° radar beam used for the PPI imagery in figure 15.

zone also appears to lie just above the turbulent layer observed in Figures 9 and 12. This signature is not well documented in the literature but was very persistent for this event and is often observed on the Westland radar over the mountains during heavy orographic rainfall events. The reduction of Z_H values suggest that the snow/ice aggregates are reducing in size within this zone, and the strong K_{DP} signature combined with only a minor increase in Z_{DR} values suggests there may be a significant increase in the target density in this area. It is therefore possible that this may be an ice-splintering and riming zone, possibly due to the turbulent layer below. If there is a significant increase in the number of targets/ice particles within this zone, and these can then grow further through riming and/or coalescence at lower levels, then this will significantly increase precipitation rates at the surface.

6. The role of turbulence in enhancing orographic precipitation

The radar imagery (Figures 9, 10, 11, 12 and 13) shows a significant and persistent trapped mountain-wave turbulent layer extending 1-2 km above the mountains up to and often beyond the main divide of the Southern Alps. This raises the question of whether or not this turbulent layer plays any contributing role in the production of

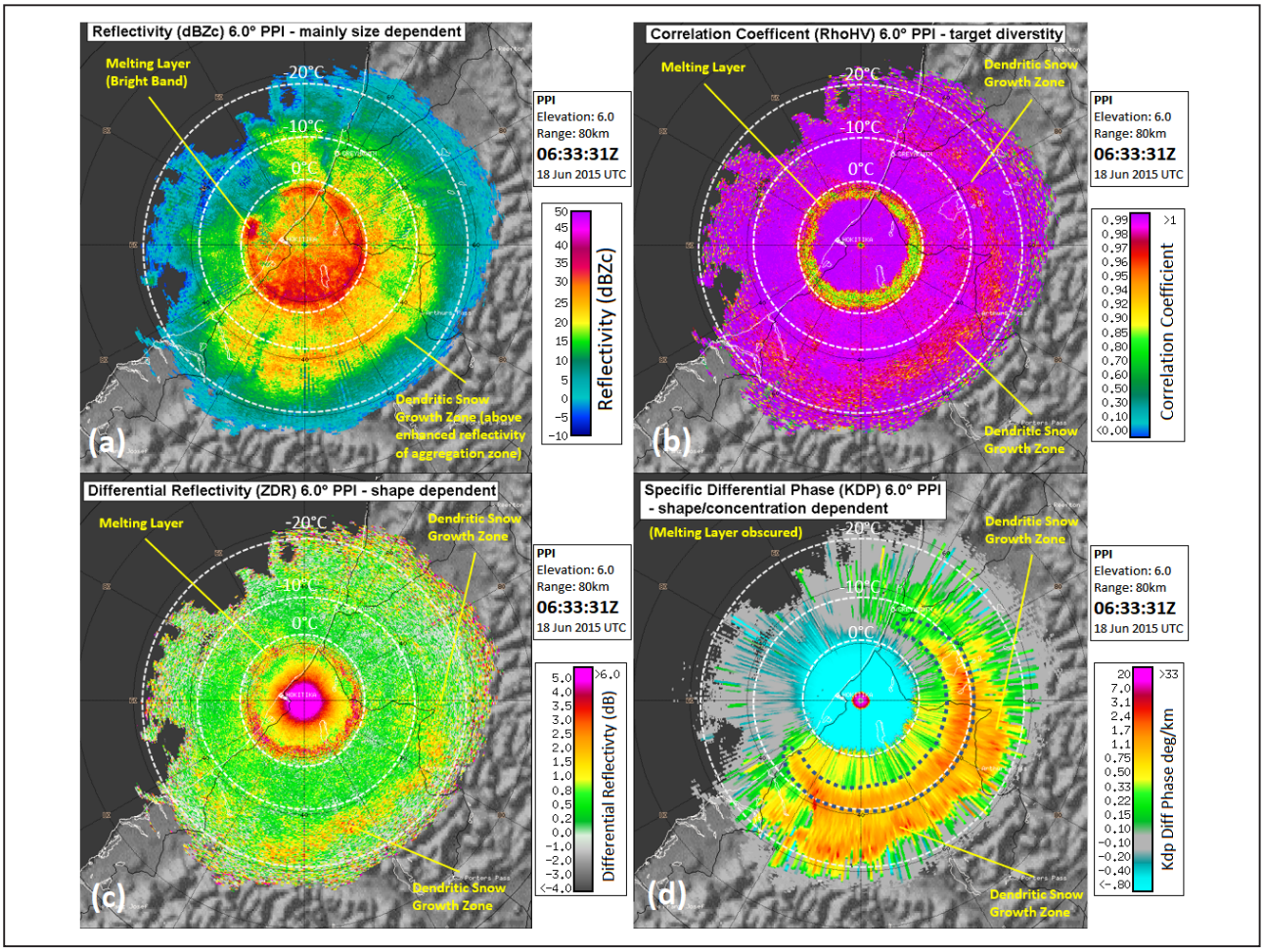

Figure 15: 6.0° Westland radar PPI (Plan Position Indicator) images for 06:30 UTC (6:30pm NZST) 18 June 2015. The 4 radar fields are (a) Horizontal Reflectivity (dBZ) corrected for attenuation, (b) Correlation Coefficient (unit-less), (c) Differential Reflectivity (dB), and (d) Specific Differential Phase (deg/km). The melting layer and Dendritic Snow Growth Zones are marked, as are approximate temperatures for 0°C, -10°C and -20°C (derived from the Hokitika Airport model tephigram shown in figure 6). Also marked on the Specific Differential Phase image is a secondary intermediate zone lying between the melting layer and the Dendritic Snow Growth Zone at approximately -5° to -10°C.

heavy rain at the surface. The Doppler radial velocity cross-sections in Figures 9b and 12b (also Figures 10 and 13) clearly show the onshore northwest flow being lifted above the turbulent layer so it does appear to provide extra lift to the ascending low-level moisture, but is it also enhancing the production of precipitation particles aloft?

Several studies have shown that turbulence does play an important role in enhancing snow crystal growth aloft (e.g. Houze and Medina, 2005, Geerts et al, 2011, Grazioli et al, 2015, Aikins et al. 2016). This turbulence can be the result of vertical wind shear (e.g., the layer between the lower blocked barrier flow and the unblocked flow above), or from orographically induced eddies/oscillations triggered by the flow of stable air over rough terrain/ridgelines (e.g., the trapped mountain waves observed in Figures 9b, 10, 12b and 13). Turbulent updrafts embedded within the flow, such as those associated with the trapped mountain waves observed in Figures 9b, 10, 12b and 13, can create pockets of highly concentrated super-cooled liquid water embedded within an orographic cloud sheet which leads to increased riming of dendritic snow-flakes/crystals falling from above (Houze and Medina 2005, Stoelinga et al. 2013). Houze and Medina (2005) found this produced heavier, more rapidly falling precipitation particles which have a higher probability of reaching the ground upwind of a mountain crest, and that without the turbulent cells, condensate would more likely be advected farther up and perhaps even over the mountain range. The observed trapped mountain waves embedded within the flow (Figures 9b, 10, 12b and 13) may also provide a favourable regime allowing heavier rimed snow crystals to fall more directly to the ground within downdrafts, and also promote further growth of ice crystals through aggregation by creating a field of highly variable and turbulent air motions which makes it easier for ice crystals to collide and stick together. At lower levels, turbulence within the warm cloud layer (i.e., temperature warmer than 0°C) also enhances coalescence through more collisions (Houze and Medina, 2005, Geerts et al., 2011).

Grazioli et al, (2015) provide a possible explanation for the observed intermediary K_{DP} layer observed in Figure 15d and relate this to turbulence. Although they mainly considered small-scale turbulence, the ideas may still be applicable to the deeper turbulent layer observed in this study. They suggest that wind shear and updrafts within the turbulent layer together continuously feed the regions above the shear layer with super-cooled liquid water and ice fragments, and favour the growth of anisotropic (directionally dependent, usually with a horizontal orientation) ice crystals at this level. This growth of anisotropic ice crystals creates an enhancement of Z_{DR} and K_{DP} in polarimetric radar imagery. Ice multiplication effects within the riming zone, and the availability of large quantities of small crystals fed from the turbulent layer below, both likely contribute to the stronger secondary peak of K_{DP} which is observed in Figure 15d between the more common higher level K_{DP} peak associated with dendritic snow growth aloft and a lower peak associated with the melting layer (which is hidden by noise from an unknown systematic bias close to the radar in Figure 15d). As mentioned previously, this observed secondary peak of K_{DP} is not well documented in the literature and doesn't appear at this strength and intensity in non-orographic or weaker orographic stratiform precipitation (whereas both the dendritic-zone and melting-layer peaks generally do).

7. Conclusion

The polarimetric radar imagery presented in this study has clearly shown several processes responsible for producing the observed heavy orographic rainfall. Some of these processes are confirmation of the existing knowledge related to South Island West Coast orographic rainfall, but some are new ideas to New Zealand.

Confirmation of existing knowledge:

- The radar imagery confirms the idea that the initial lifting of the low-level moisture occurs over the

northeast barrier flow (as modelled by Revell et al., 2002), then rises further over the mountains providing moisture to the snow-growth and riming zones.

- The polarimetric radar imagery clearly shows the melting layer and Dendritic Snow Growth Zone, which are both enhanced over the mountains. These layers are both well-known and documented features in polarimetric radar imagery and are observable in most deep stratiform rain systems (for further detail see Kumjian, 2013).

- The main microphysical growth mechanisms in the production of heavy orographic stratiform rainfall are the deposition processes (especially the growth of dendrites, which maximises around -13 to -17°C in the region known as the Dendritic Snow Growth Z.one), and the accretion processes (i.e., riming (cold cloud), aggregation (cold cloud) and collision/coalescence (warm cloud)), with deposition, riming and collision/coalescence likely the most important (for further detail see Stoelinga et al., 2013).

- Ice multiplication/splintering is likely to be important in the production of heavy stratiform rain as it provides more ice crystals which can grow further through riming and aggregation (for further detail see Hallott and Mossop, 1974; Grazioli et al., 2015).

- The downwind drift of lighter snowflakes formed aloft on the western side of the Southern Alps leads to spillover precipitation east of the main divide (as suggested by Sinclair et al., 1997, Chater and Sturman, 1998)

The radar imagery also reveals some additional processes associated with heavy orographic rain on the South Island West Coast, which are consistent with the findings of previous studies (e.g. Houze et al., 2005, Geerts et al., 2011, Grazioli et al., 2014, Aikins et al., 2016). Specifically, as discussed in section 6, the observed trapped mountain waves embedded within the rainband and associated turbulence are considered to be an important mechanism for the enhancement of the orographic precipitation by providing additional lift to the onshore airmass and enhancing ice crystal growth aloft. The radar cross sections (Figures 9 and 12) showed the low-level moisture being lifted quickly up into the snow and ice growth regions, with a strongly enhanced Dendritic Snow Growth Zone observed in the Correlation Coefficient and Differential Reflectivity imagery (Figures 9c/d and 12c/d) immediately above, and even slightly upwind, of the first range of mountains. This would have produced significant numbers of snow crystals well upwind of the highest terrain that grew further through aggregation and riming at lower levels due to the turbulent trapped mountain waves producing pockets of highly concentrated super-cooled liquid water. This, combined with a lighter horizontal wind regime and the associated updrafts and downdrafts within the embedded trapped mountain waves, would have produced heavier, more rapidly falling precipitation particles which had a higher probability of reaching the ground well upwind of the main divide. These processes are considered to have significantly contributed to producing the heavy stratiform rain observed over the mountains upwind of the main divide, and when combined with the strong collision-coalescence and/or collectional growth type effects observed at lower levels in section 4 (Figures 9 and 12), most likely increased the rainfall nearer the coast leading to the significantly heavier rain recorded at the Hokitika Gorge rain-gauge compared to the Mt Browning gauge which is located at a higher elevation farther downwind closer to the main divide (Figure 8).

A secondary (intermediate) ice-growth region was also observed in the Specific Differential Phase (K_{DP}) imagery between the melting layer and the Dendritic Snow Growth Zone (Figure 15). This zone is not well documented in the

literature and is considered to be a riming and splintering (ice multiplication) zone which is not always as strong or as well defined in other non-orographic stratiform rain systems. This zone appears to be related to heavy surface precipitation, and possibly indicates large numbers of small, splintered ice crystals undergoing riming. As discussed in section 6, the combination of wind shear and vertical updrafts/downdrafts within the turbulent mountain wave layer may have broken up falling ice crystals and fed the regions above with small ice fragments that grew further through the riming process leading to more precipitation. It is suggested that the embedded mountain wave/turbulent layer and the intermediate enhanced K_{DP} layer observed in the radar imagery are related, and probably act together to enhance surface precipitation in mountainous terrain.

In conclusion, this study has shown that the dominant microphysical processes involved in producing the heavy orographic rain observed during this event are related to the strength and location of the dendritic snow growth zone, the riming and ice splintering above the mountain wave turbulent layer, and the enhancement of the rainfall at low levels by warm rain processes (i.e., collision-coalescence and collectional growth). The turbulent layer embedded within the rainband appears to be an important mechanism in enhancing the first two of these processes, and, when combined with warm rain effects at lower levels, may also be a factor in shifting the maximum rain accumulations well upwind of the Southern Alps main divide nearer to the first range of mountains. Due to their short horizontal wavelength, these mountain waves are generally poorly resolved by numerical weather prediction (NWP) models, and this may be one of the reasons the forecast models occasionally under-estimate the rainfall about the Southern Alps. Future work to improve the forecasting and modelling of these embedded turbulent mountain waves could lead to a better understanding of the observed rainfall distribution about the mountains on the South Island West Coast. Other future work could include using the MetService Westland radar to scan above the mountains at a better vertical resolution and higher Nyquist velocity, and maybe even using a separate vertically-pointing Doppler radar located within the mountains west of the main divide, to better understand the above-mountain turbulent layer and its contribution to enhancing the surface rainfall.

Acknowledgements

The authors would like to thank West Coast Regional Council and MetService for the use of their rain-gauge data, and MetService for the radar data used in this study.

References

Aikins, J., Friedrich, K., Geerts, B. and Pokharel, B., 2016. Role of a cross-barrier jet and turbulence on winter orographic snowfall. Monthly Weather Review, 144(9), pp.3277-3300.

Andrić, J., Kumjian, M.R., Zrnić, D.S., Straka, J.M. and Melnikov, V.M., 2013. Polarimetric signatures above the melting layer in winter storms: An observational and modeling study. Journal of Applied Meteorology and Climatology, 52 (3), pp.682-700.

Bechini, R., Baldini, L. and Chandrasekar, V., 2013. Polarimetric radar observations in the ice region of precipitating clouds at C-band and X-band radar frequencies. Journal of Applied Meteorology and Climatology, 52 (5), pp.1147-1169.

Chater, A.M. and Sturman, A.P., 1998. Atmospheric conditions influencing the spillover of rainfall to lee of the Southern Alps, New Zealand. International Journal of Climatology: A Journal of the Royal Meteorological Society, 18 (1), pp.77-92.

COMET, 2016. MetEd: Forecasting Mountain Wave Turbulence for Aviation, viewed 26 July 2021. University Corporation for Atmospheric Research. <www.meted.ucar.edu/aviation/mtnwave_turbulence>

Geerts, B., Miao, Q. and Yang, Y., 2011. Boundary layer turbulence and orographic precipitation growth in cold clouds:

Evidence from profiling airborne radar data. Journal of the atmospheric sciences, 68(10), pp.2344-2365.

Grazioli, J., Lloyd, G., Panziera, L., Hoyle, C.R., Connolly, P.J., Henneberger, J. and Berne, A., 2015. Polarimetric radar and in situ observations of riming and snowfall microphysics during CLACE 2014. Atmospheric Chemistry and Physics, 15 (23), pp.13787-13802.

Hallett, J. and Mossop, S.C., 1974. Production of secondary ice particles during the riming process. Nature, 249 (5452), pp.26-28.

Henderson, R.D. and Thompson, S.M., 1999. Extreme rainfalls in the southern Alps of New Zealand. Journal of Hydrology (New Zealand), pp.309-330.

Houze Jr, R.A., 2012. Orographic effects on precipitating clouds. Reviews of Geophysics, 50 (1).

Houze Jr, R.A. and Medina, S., 2005. Turbulence as a mechanism for orographic precipitation enhancement. Journal of the atmospheric sciences, 62 (10), pp.3599-3623.

Kennedy, P.C. and Rutledge, S.A., 2011. S-band dual-polarization radar observations of winter storms. Journal of Applied Meteorology and Climatology, 50 (4), pp.844-858.

Kumjian, M.R., 2013. Principles and Applications of Dual-Polarization Weather Radar. Part II: Warm-and Cold-Season Applications. Journal of Operational Meteorology, 1.

Macara, G.R., 2018. The climate and weather of New Zealand. NIWA Science and Technology Series 74, 50 pp.

MetService 2015, Snowfall in New Zealand, MetService, viewed 26 July 2021, <https://blog.metservice.com/node/1063>

Moisseev, D.N., Lautaportti, S., Tyynela, J. and Lim, S., 2015. Dual-polarization radar signatures in snowstorms: Role of snowflake aggregation. Journal of Geophysical Research: Atmospheres, 120 (24), pp.12644-12655.

Neale, A.A. and Thompson, G.H., 1977. Meteorological conditions accompanying heavy snowfalls in southern New Zealand. New Zealand Meteorological Service.

Purdy, J.C. and Austin, G.L., 2003. The role of synoptic cloud in orographic rainfall in the Southern Alps of New Zealand. Meteorological Applications: A journal of forecasting, practical applications, training techniques and modelling, 10(4), pp.355-365.

Purdy, J.C., Austin G.L., Seed A.W., Cluckie I.D., 2005. Radar evidence of orographic enhancement due to the seeder feeder mechanism. Meteorological Applications, 12 (3), pp 199-206.

Revell, M.J., Copeland, J.H., Larsen, H.R. and Wratt, D.S., 2002. Barrier jets around the Southern Alps of New Zealand and their potential to enhance alpine rainfall. Atmospheric research, 61 (4), pp.277-298.

Rinehart, R.E., 2010. Radar for Meteorologists, Or, You Too Can be a Radar Meteorologist, Part III. Rinehart Publications.

Rotunno, R. and Houze, R.A., 2007. Lessons on orographic precipitation from the Mesoscale Alpine Programme. Quarterly Journal of the Royal Meteorological Society: A journal of the atmospheric sciences, applied meteorology and physical oceanography, 133 (625), pp.811-830.

Schrom, R.S., Kumjian, M.R. and Lu, Y., 2015. Polarimetric radar signatures of dendritic growth zones within Colorado winter storms. Journal of Applied Meteorology and Climatology, 54 (12), pp.2365-2388.

Sinclair, M.R., Wratt, D.S., Henderson, R.D. and Gray, W.R., 1997. Factors affecting the distribution and spillover of precipitation in the Southern Alps of New Zealand—A case study. Journal of Applied Meteorology, 36 (5), pp.428-442.

Stoelinga, M.T., Stewart, R.E., Thompson, G. and Thériault, J.M., 2013. Microphysical processes within winter orographic cloud and precipitation systems. In Mountain Weather Research and Forecasting (pp. 345-408). Springer, Dordrecht.

Waldteufel, P. and Corbin, H., 1979. On the analysis of single-Doppler radar data. Journal of Applied Meteorology and Climatology, 18 (4), pp.532-542.

Wratt, D.N., Ridley, R., Sinclair, M.R., Larsen, H.M., Thompson, S., Henderson, R., Austin, G., Bradley, S.H., Auer, A., Sturman, A.F., Owens, I., Fitzharris, B., 1996. The New Zealand Southern Alps Experiment. Bulletin of the American Meteorological Society, 77, pp 683-692.

Evaluation of global and regional reanalyses performance over New Zealand

A.A.S. Pirooz[1], S. Moore[1], T. Carey-Smith[1], R. Turner[1], C.-H. Su[2]

[1]NIWA-Taihoro Nukurangi, 301 Evans Bay Parade, Ākautangi, Hātaitai, Wellington, Aotearoa New Zealand
[2] Bureau of Meteorology, Docklands, Victoria 3008, Australia

Correspondence: stuart.moore@niwa.co.nz , amir.pirooz@niwa.co.nz

Key words: Regional reanalysis, numerical weather prediction, BARRA, ERA, verification

Abstract

Atmospheric reanalyses provide long-term physically consistent and spatially complete records of meteorological variables that can be used to study recent past climate trends and establish extreme event climatologies. In this work, three global reanalysis products, namely ERA-Interim, ERA5 and ERA5-Land along with a 12-km resolution regional reanalysis, BARRA-R, are compared against point-based and gridded observational data across New Zealand for the period 2014 – 2018 for four variables; mean and gust wind speeds, total precipitation, and surface air temperature. It is generally found that the skill of the reanalyses decays over the mountainous regions of the South Island, in high wind regions such as the Cook and Foveaux Straits, and in high rainfall regions like the west coast of the South Island. The study demonstrates that the BARRA-R reanalysis performs better for precipitation and temperature than ERA reanalysis products over New Zealand. BARRA-R outperforms ERA-Interim in predicting gust wind speeds. However, unlike ERA5, BARRA-R does not capture the frequency of high gust wind speeds over the more southern mountains of the South Island but does produce higher gust speeds in the lower North Island.

1. Introduction

Although meteorological observing stations generally provide valuable and reliable data, they are usually located far from one another, inhibiting high quality spatial analyses. Such data sparsity, the effects of local orography and regional climate variability can make interpolation techniques unreliable and diminish their value (Tait et al., 2006). Accurate spatial estimation of climate variables is essential for many applications and studies, such as extreme value analysis and engineering designs (Mo et al., 2015; Xu et al., 2020), energy resources assessment (Frank et al., 2018; Miao et al., 2020), hydrological models (Essou et al., 2017), enhancement of climate projection models and evaluation of climate change effects (Di Virgilio et al., 2019; Avila-Diaz et al., 2020). In addition, historical observational data are often available only for a limited period or are not continuous. Therefore, alternative datasets, such as numerical model-derived reanalysis products, which can provide physically consistent and long-term spatially complete records of climate variables, can be employed to fill the gaps in observations time series (Dee et al., 2011; Tetzner et al., 2019).

Reanalysis products are developed utilising numerical weather prediction (NWP) models and data assimilation techniques to generate observation-constrained model estimates of climate variables (Su et al., 2019). Several global and regional reanalysis datasets with different

Submitted: 7 September 2021
Accepted: 10 November 2021

spatial and temporal resolutions are currently available. Early global reanalysis products, such as European ReAnalysis-40 (ERA40) (Uppala et al., 2005) employ a coarse resolution model that is unable to capture well the sub-grid variations of variables and small-scale processes, particularly over complex terrain (Su et al., 2019). Regional reanalyses are often developed by downscaling from a coarser resolution global-scale model to a higher resolution limited domain and therefore provide better temporal and spatial representations of meteorological fields, improving variability and the representation of extremes and frequency distributions.

Recently, Su et al. (2019) developed the first regional reanalysis covering a large region of Oceania, including Australia, New Zealand, and southeast Asia, which has a horizontal resolution of 12 km and uses ERA-Interim as the driving model. Compared to global reanalyses, the Bureau of Meteorology Atmospheric high-resolution Regional Reanalysis (BARRA-R) showed better statistical scores and agreement with respect to observations over Australia, particularly in estimating temperature, wind speed, surface pressure, precipitation and frequency of heavy rain events. Later, Su et al. (2021) created the BARRA-C reanalysis dataset by downscaling BARRA-R to 1.5 km horizontal resolution over four major Australian cities. At this scale wind and temperature performance, particularly over complex and coastal regions, was further enhanced.

As complementary datasets to observations, reanalyses provide invaluable information for meteorological and climatological studies, particularly where observations are scarce. However, the performance of each reanalysis needs to be assessed to fully understand their limitations and uncertainties associated with their resolution or NWP science.

In this study, we evaluate the performance over New Zealand of the BARRA-R regional reanalysis (Su et al., 2019) and that of three commonly used global reanalysis products, namely European ReAnalyses (ERA) products of the European Centre for Medium-Range Weather Forecasts (ECMWF): ERA-Interim (Dee et al., 2011), ERA5 (Hersbach et al., 2020) and ERA5-Land (Muñoz Sabater, 2019). In Section 2, we outline the observation and reanalysis datasets used and the statistical methods applied in our evaluation. We present results in Section 3, focusing on precipitation, air temperature, and mean and gust wind speed performance over relatively flat and complex mountainous regions before summarising our findings in Section 4.

2. Methodology and data

In this work we concentrate on the five-year period, 2014 to 2018, using data from ERA-Interim, ERA5, ERA5-Land and BARRA-R. Table 1 summarises the main specifications of the reanalysis products used in this study. ERA5 is the ECMWF's latest climate reanalysis product replacing ERA-Interim. Compared with ERA-Interim, ERA5 benefits from 10 years of developments in the model physics and data assimilation, including the use of satellite data in NWP and atmospheric modelling (Hersbach et

Table 1: Global- and regional- scale reanalysis products used in this study.

	Name	Reference	Spatial Resolution	Temporal Resolution	Temporal Availability	Model Cycle
Global	ERA-Interim	(Dee et al, 2011)	80 km	3-hourly	1979 – present	Cy31r2 (2006)
	ERA5	(Hersbach et al, 2020)	31 km	Hourly	1950 – present	Cy41r2 (2016)
	ERA5-Land	(Muñoz-Sabater, 2019)	9 km	Hourly	1981 – present	Cy45r1 (2018)
Regional	BARRA-R	(Su et al, 2019)	12 km	Hourly	1990 – present	UM 10.2

al., 2020; Muñoz-Sabater et al., 2021). The ERA products are based on the ECMWF Integrated Forecasting System (IFS) models, as outlined in Table 1. ERA5-Land is an enhanced global dataset for the land component of ERA5, and shares most of its parametrisations with ERA5 (Muñoz-Sabater, 2019; Muñoz-Sabater et al., 2021). The higher horizonal resolution along with the non-linear dynamical downscaling with corrected thermodynamic input are the main advantage and improvement of ERA5-Land over its driving model, ERA5. Unlike the ERA products, BARRA-R uses the Unified Model (UM) (Davies et al., 2005) and is initialised using ERA-Interim and is forced with lateral boundary conditions derived from ERA-Interim; for more details see Su et al. (2019). All the reanalyses considered in this study, except for ERA5-Land, use a 4-dimensional variational data assimilation technique. Although ERA5-Land does not assimilate observational data directly, the observations affect the atmospheric forcing derived from ERA5, which drives ERA5-Land. In addition, BARRA-R has the benefit of assimilating additional observations over New Zealand from the National Climate Database (Cliflo, 2020), which may not be assimilated in other reanalyses. In BARRA-R, at each 6-hr analysis, observations valid from ±3 hr were used in the data assimilation scheme. However, the validation in this study is done using BARRA-R forecast data valid from 3 hr to 9 hr after the analysis time. Thus, the validating observations are independent of those used in the data assimilation.

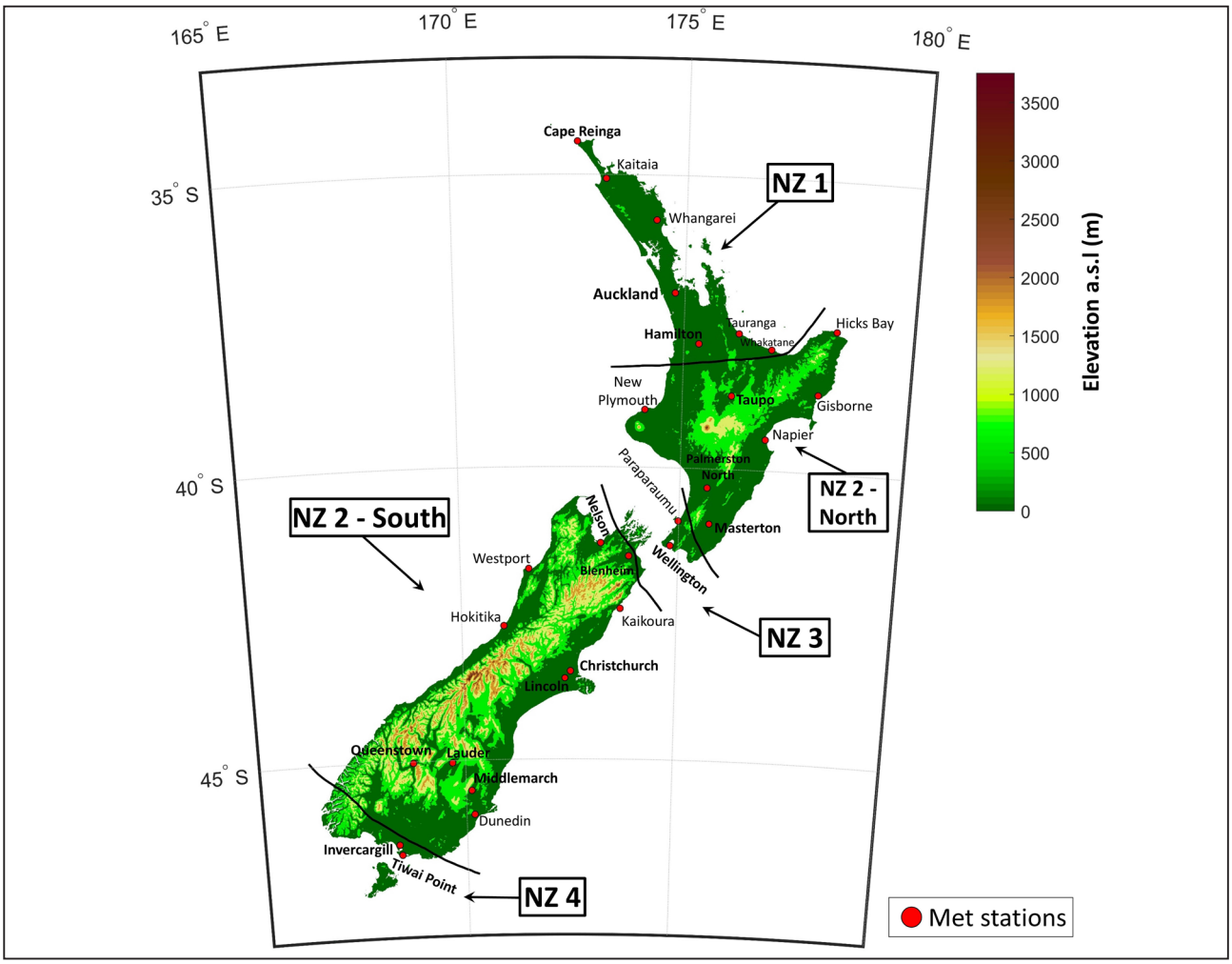

Figure 1: Orography map of New Zealand (1-km resolution) along with the locations of meteorological stations considered in this study. The New Zealand wind regions are also labelled.

The evaluation is made against two sets of observation data:

- Point-based meteorological station data recorded at selected stations around New Zealand and available from NIWA's online CliFlo climate database (Cliflo, 2020), and
- Virtual Climate Station Network (VCSN) data (Tait and Turner, 2005; Tait et al., 2006; Tait et al., 2012), which comprises 2D surfaces of climate variables (excluding gust wind speed) covering all of New Zealand on a 5-km grid based on the spatial interpolation of actual observation data at climate stations.

Station-based observations are available at an hourly temporal resolution, while VCSN only provides daily data. Further, VCSN provides two sets of rain data. The first, hereafter called VCSN, is the original rain field. More recently, a bias corrected rain field was added to VCSN, hereafter called VCSN_BC, which was corrected by incorporating more regional council station data into the original VCSN. The statistical scores for total precipitation were calculated between the reanalysis data and VCSN_BC.

In the case of mean and gust wind speeds, where often the measurements have not been taken following standard (World Meteorological Organisation, 2014), the retrieved observations were homogenised and converted to a common standard, namely 10-m height and 3-s gust duration, using the procedure proposed by Turner et al. (2019), Safaei Pirooz et al. (2020a) and Safaei Pirooz et al. (2020b).

Region NZ1 is relatively flat and covers the northern part of the North Island (NI). The NZ2 region consists of parts of both the North and South Islands, which have different orography. As shown in Figure 1, the South Island (SI) has steeper and more complex terrain compared to NI. NZ4 is exposed to strong westerly and south-westerly winds, and NZ3, due to the channelling effect of Cook Strait (Turner et al., 2019; Safaei Pirooz et al., 2020b), experiences strong westerly and north-westerly winds.

Land-sea masks of the reanalyses are shown in Figure 2 to better understand the performance of the models over different regions and coastal areas. It is clear that BARRA-R misses some land points in coastal regions, particularly in regions NZ3 and NZ4. In contrast, ERA5, and particularly ERA5-Land, product better represent the true coastline. By default, ERA products return a fractional land-sea mask. For the coastline comparison, the ERA's land-sea

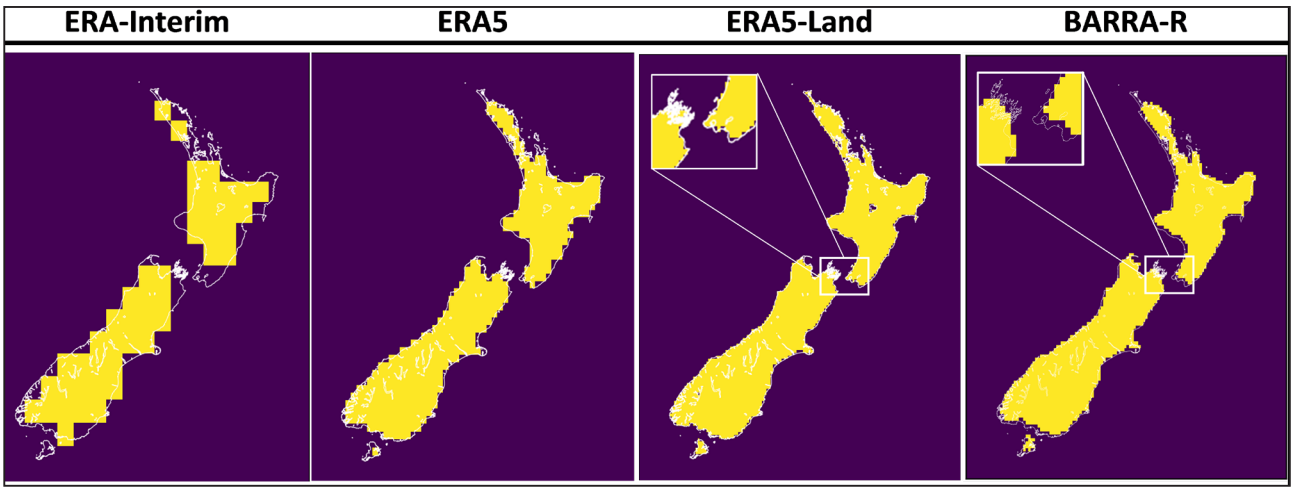

Figure 2: Land-sea masks of the reanalysis products used in this study.

masks were processed to generate binary land-sea masks, according to the guidelines provided in https://confluence.ecmwf.int/display/CKB/ERA5%3A+data+documentation; that is where land-sea mask value is greater than 0.5, set to a value of 1 (land), and where land-sea mask value is equal to or less than 0.5, set to 0 (ocean).

In carrying out the assessment, the closest reanalysis grid point to the meteorological stations were determined. Then, three statistical tests are performed (Tetzner et al., 2019; Minola et al., 2020).

- Pearson's correlation coefficient, which measures the strength of a linear association between two time series and is calculated using Eq. 1, where *X* and *Y* are the reanalysis and observation data, *cov*() and *var*() are the calculated covariance and variance, respectively. The Pearson correlation coefficient can take values from –1 to +1, with values closer to either –1 or +1, depending on negative or positive relationship, showing a stronger linear association of the two variables. Values close to zero indicates there is no association between the two variables. Values between –1 and +1, e.g. 0.7, show that there is variation around the line of best fit. To evaluate weather-generated variability, rather than climatological cycles, it is essential to remove periodicity in wind speed time series, which for the hourly and daily series can be done by subtracting mean diurnal and monthly series, respectively.

$$\rho(X,Y) = \frac{cov(X,Y)}{\sqrt{var(X)\,.\,var(Y)}} \qquad (1)$$

- Root Mean Square Error (RMSE): shows how far or close the reanalysed values are from the observed values. RMSE is calculated by Eq. 2, in which *X*, *Y* and *T* are the reanalysis, observed values, and number of data points, respectively.

$$RMSE = \sqrt{\frac{\sum_{t=1}^{T}(X-Y)^2}{T}} \qquad (2)$$

- Bias shows the deviation of the reanalysis data from the observations.

$$Bias = \frac{\sum_{t=1}^{T}(X-Y)}{T} \qquad (3)$$

3. Results

3.1 Total precipitation

Total daily precipitation from each reanalysis dataset are assessed against VCSN_BC data in Figure 3. ERA-Interim shows the lowest correlation, ranging from 0.7 – 0.8 across the country. ERA5 and ERA5-Land have correlations generally greater than 0.8, while the values drop over areas of complex terrain. BARRA-R depicts lower correlations, compared with ERA5 and ERA5-Land, of around 0.6 – 0.8 over the mountains and localised orography, which could be attributed to the different model physics and data assimilations used by these models. The precipitation is not corrected between ERA5 and ERA5-Land (Muñoz-Sabater et al., 2021). Thus, the performance of ERA5 and ERA5-Land is expected to be similar and marginal differences could be due to the grid resolution and the downscaling used in ERA5-Land.

All the considered reanalyses show high RMSE values, exceeding 15 mm, along the west coast of the SI. In terms of mean biases, ERA5 and ERA5-Land are generally negatively biased over complex terrain, particularly in the west part of the SI where the mean bias is about –7.5 mm. On the other hand, BARRA-R mostly shows positive bias over the mountainous regions. VCSN has been determined to underestimate the total precipitation, particularly over high-elevation terrain (Tait et al., 2006; Ackerley et al., 2012). Thus, the apparent overestimation of precipitation by BARRA-R, especially on the west coast of SI, is not believed to necessarily indicate poor performance of the model. On the eastern side of the SI, all the reanalyses are positively biased, with values mostly range 0.0 to 2.5 mm. These scores are clearly tied to the

underlying terrain of the Southern Alps and is likely indicative of the reanalysis model's inability to correctly simulate the orographically enhanced rainfall in this region. In the NI, where the topography effects are less significant, the mean bias values are generally within –2.5 mm to 2.5 mm.

The frequency of days with precipitation intensities between 1 mm to 10 mm, 10 mm to 50 mm, and greater than 50 mm, is shown in Figure 4. In these graphs, the X-axis shows the station observations and Y-axis is the corresponding closest VCSN_BC and reanalyses grid points values. The slope (*S*) of the lines of best fit and correlation (R^2) values are also shown in the figure. It can be seen that ERA5, ERA5-Land and ERA-Interim overestimate the fraction of days for which precipitation was between 1 – 10 mm. BARRA-R estimates the fraction of days with precipitation between 1 mm and 10 mm better than ERA5, with higher R^2 and *S* closer to 1.0, but slightly overestimating the fraction compared with VCSN_BC. ERA5, ERA5-Land and BARRA-R show similar results for 10 – 50 mm and over 50 mm precipitation ranges,

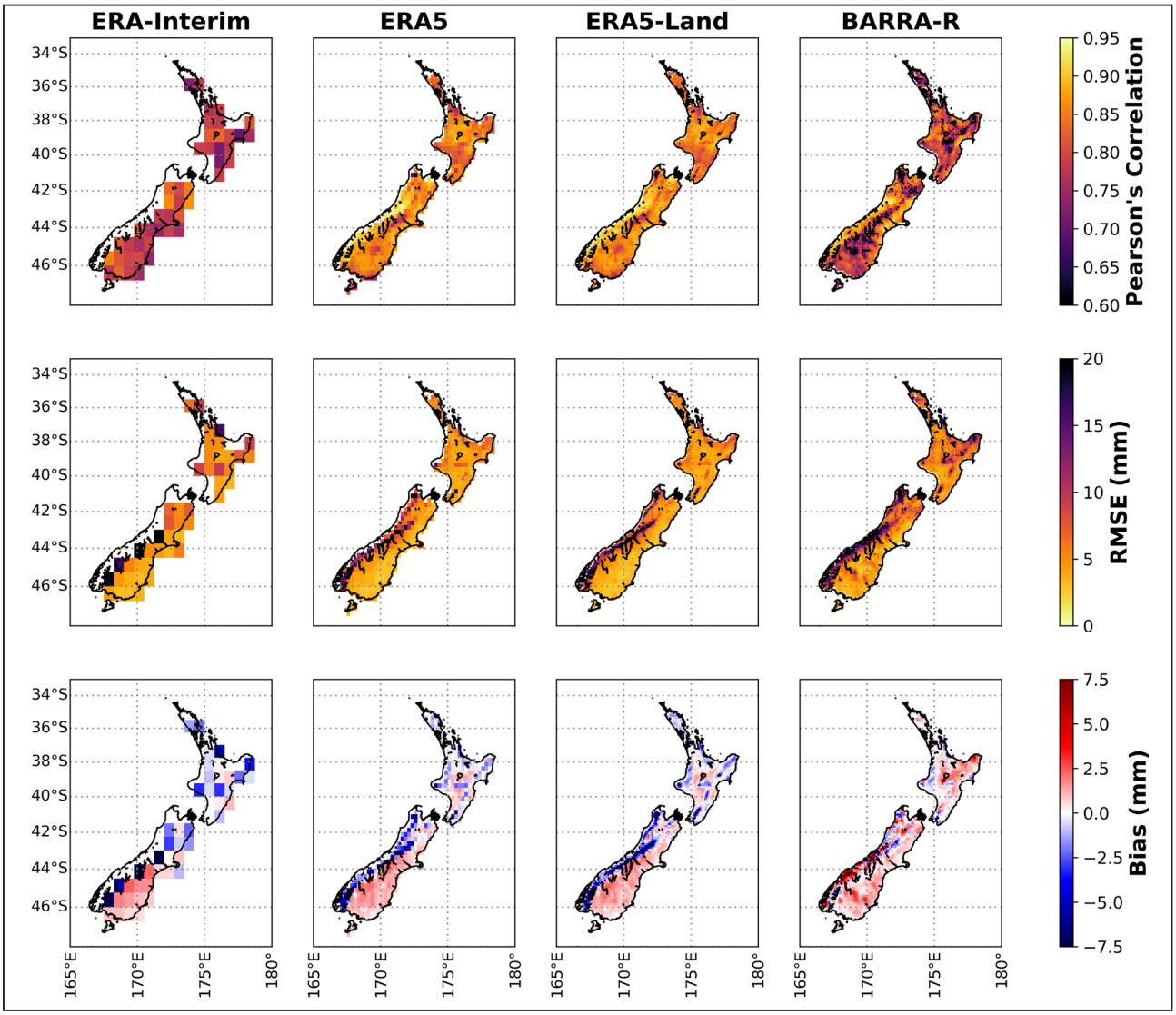

Figure 3: Statistical results calculated between the bias corrected VCSN and closest reanalysis grid point for total daily precipitation. First, second, and third rows are Pearson's correlation coefficients, RMSE and bias, respectively. Also, from left to right columns show the comparison between VCSN_BC and ERA-Interim, ERA5, ERA5-Land, and BARRA-R, respectively.

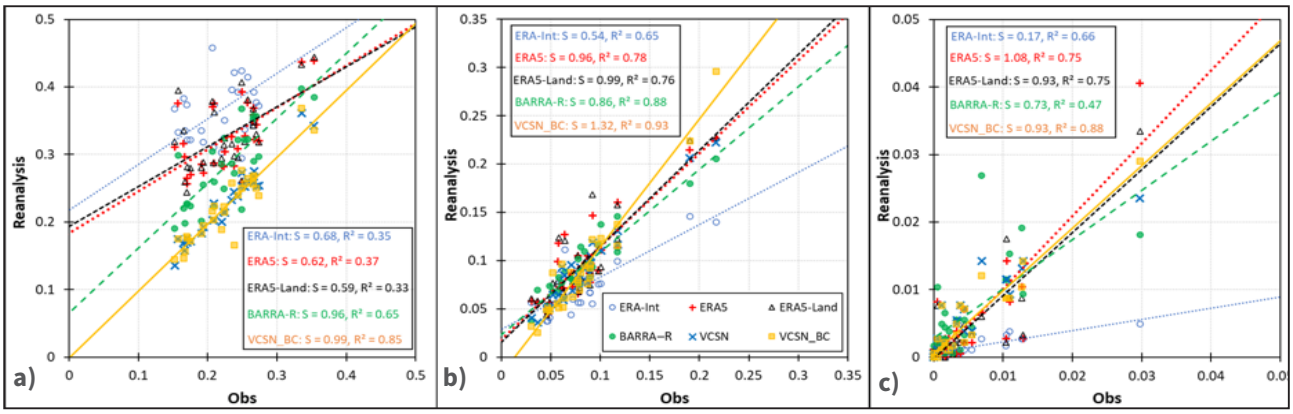

Figure 4: Fraction of days that total daily precipitation is: (a) 1 – 10 mm; (b) 10 – 50 mm; (c) greater than 50 mm, for the station observation data (X-axis) and corresponding closest VCSN_BC and reanalyses grid points (Y-axis) during 2014 to 2018. "S" and "R^2" are the slope and correlation of the best fit line, respectively.

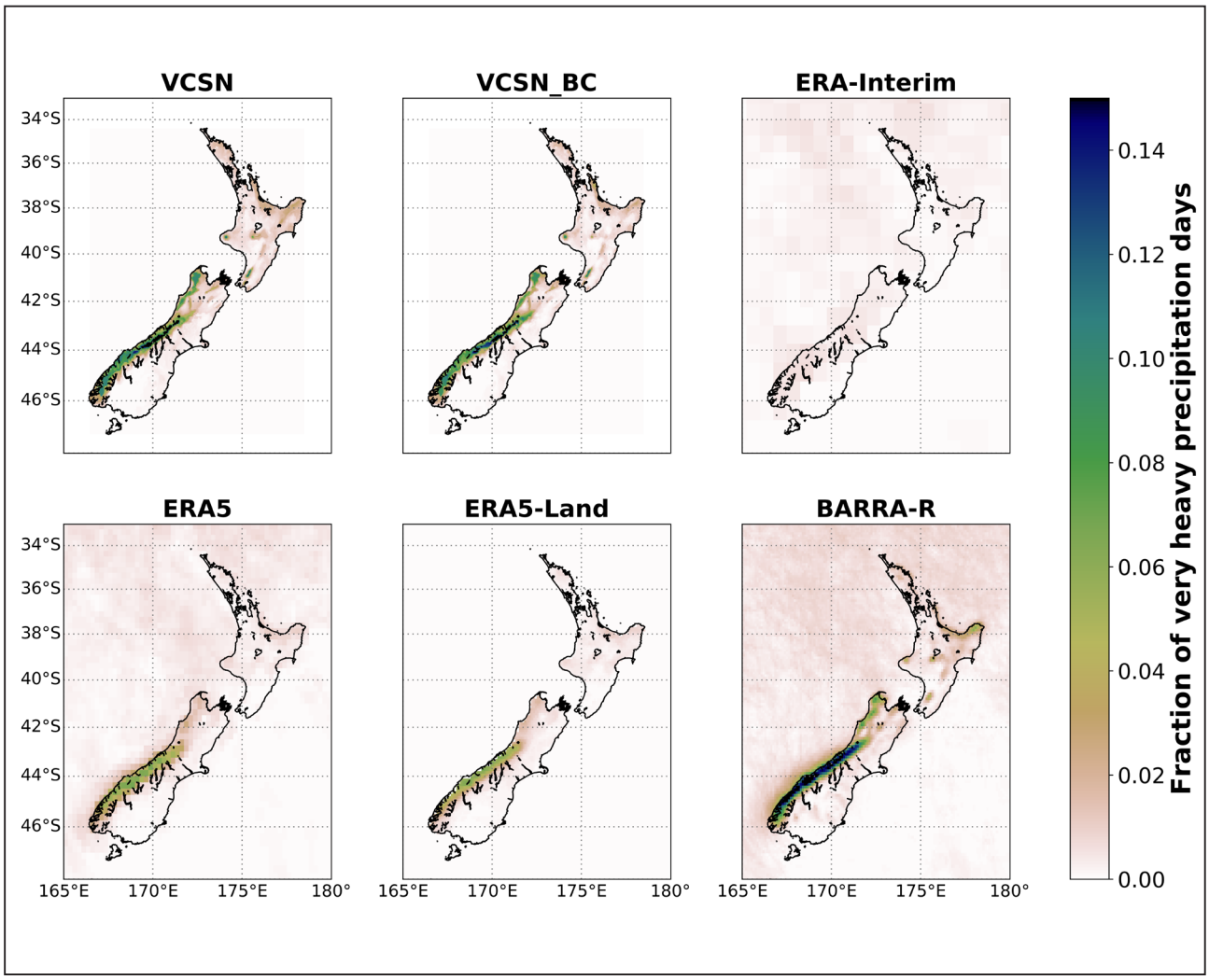

Figure 5: Fraction of days that precipitation is greater than 50 mm. Comparison between VCSN, VCSN_BC and reanalysis products.

while ERA-Interim underestimates the fraction of rainy days for both these ranges. For over 50 mm precipitation ranges, BARRA-R shows lower R^2 and S values compared with ERA5 and ERA5-Land.

In terms of fraction of rainy days in different seasons (not shown), unlike BARRA-R that agrees well with observations, ERA-Interim, ERA5 and ERA5-Land overestimate the numbers of days in almost all seasons and for the 1 – 10 mm range, and often show a poor correlation with the observation values (e.g. Jun – Aug (JJA) and Sep – Nov (SON) 1-10 mm). For 10 – 50 mm and > 50 mm precipitation ranges, BARRA-R, ERA5 and ERA5-Land depict good agreement with observations, and BARRA-R slightly outperforms the other reanalysis products, except for high precipitation estimates in SON season (seasonal results not shown here).

For a better spatial assessment, Figure 5 compares the fraction of very heavy precipitation (i.e. > 50 mm accumulation) days across New Zealand obtained from the reanalyses and both VCSN datasets. BARRA-R is the only reanalysis dataset to provide similar estimates of the frequency of very heavy rains compared with VCSN, particularly on the west of the SI and over the NI topography. While ERA-Interim does not capture the frequency of very heavy rain days at all, ERA5 and ERA5-Land do exhibit signatures of increased heavy

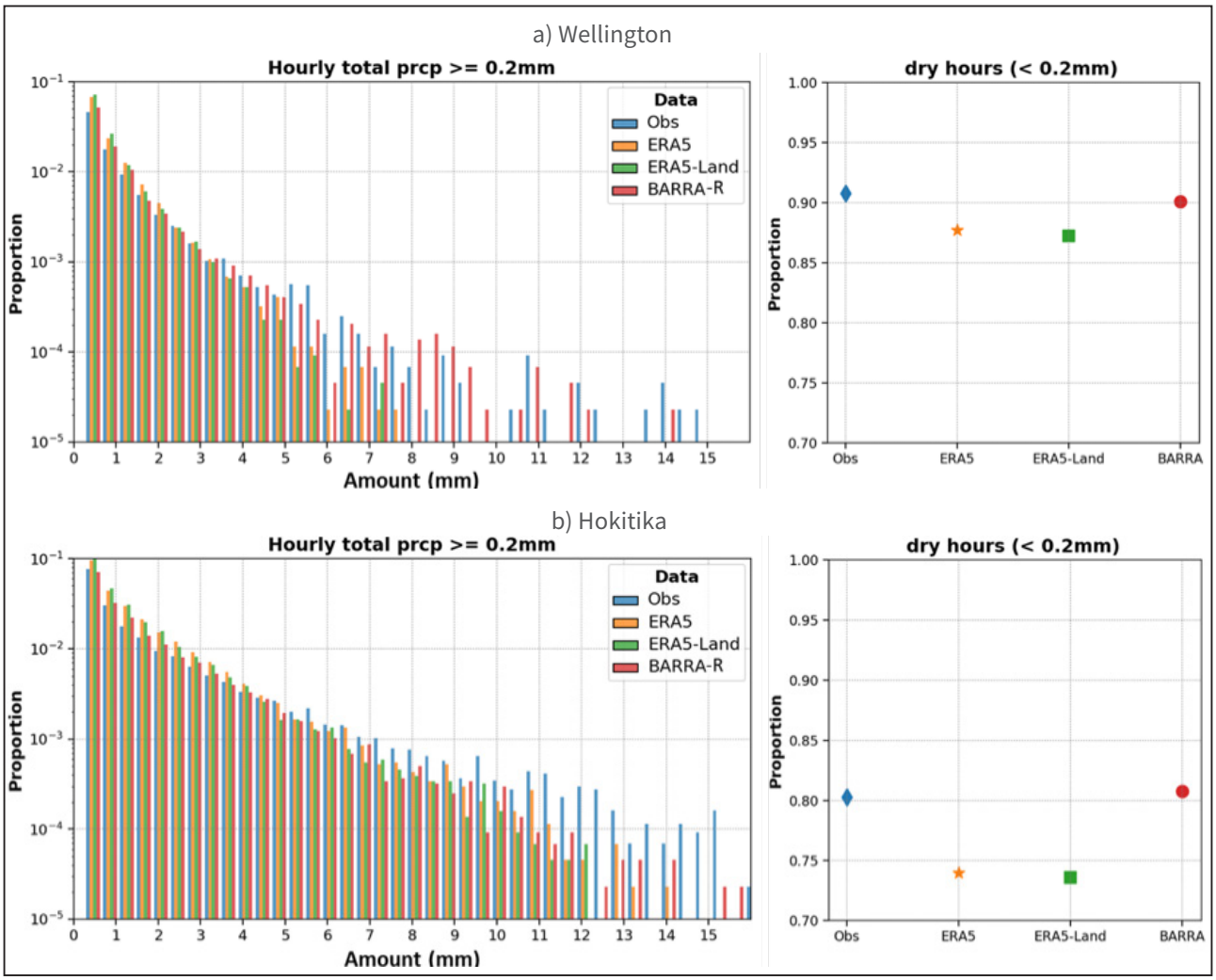

Figure 6: Comparison of station data and reanalyses distributions of hourly wet (left), i.e. >= 0.2 mm precipitation, and dry (right), i.e. < 0.2 mm precipitation, at: (a) Wellington; (b) Hokitika.

rainfall along the SI's west coast but both underestimate compared to VCSN and BARRA-R, suggesting these datasets do not capture rainfall totals representative of that region. Su et al. (2019) and Jermey and Renshaw (2016) also point out that higher-resolution reanalysis products better represent high-threshold events.

Figure 6 compares the distribution of hourly precipitation accumulations (i.e. >= 0.2 mm) and dry (< 0.2mm) times between the reanalysis datasets at two observing stations. Generally, the reanalysis products overestimate the hourly precipitation less than 3 – 3.4 mm and underestimates the precipitations greater than these values, except for BARRA-R, which estimates the high accumulations more accurately compared with observational data. This is particularly evident for Wellington (Figure 6a, left panel). At most locations ERA products do not capture well the frequency of high hourly and daily accumulations (daily results are not shown).

Regarding the frequency of dry (< 0.2 mm) hours, the ERA reanalyses predict fewer number of hours. BARRA-R, however, generally provides a much better estimation of dry periods across most sites (Figure 6, right panels).

3.2. Temperature

The statistical scores for minimum and maximum daily temperatures in each season over New Zealand between observations and reanalyses are shown in Figure 7. With the exception of ERA-Interim, the different reanalyses have similar performance with only minor differences. During winter (JJA), the reanalyses show slightly lower and more scattered correlation (Figure 7a), and higher RMSE and biases (Figure 7a) for the minimum daily temperature. In the case of maximum daily temperature (Figure 7b), during summer (DJF) and winter (JJA), the models show weaker and more scattered scores. The bias values for the minimum and maximum temperatures generally range from –2°C to 2°C and –4°C to 0.5°C, respectively. Compared to the ERA-5, BARRA-R generally exhibits better mean Pearson's Correlation and Bias scores across

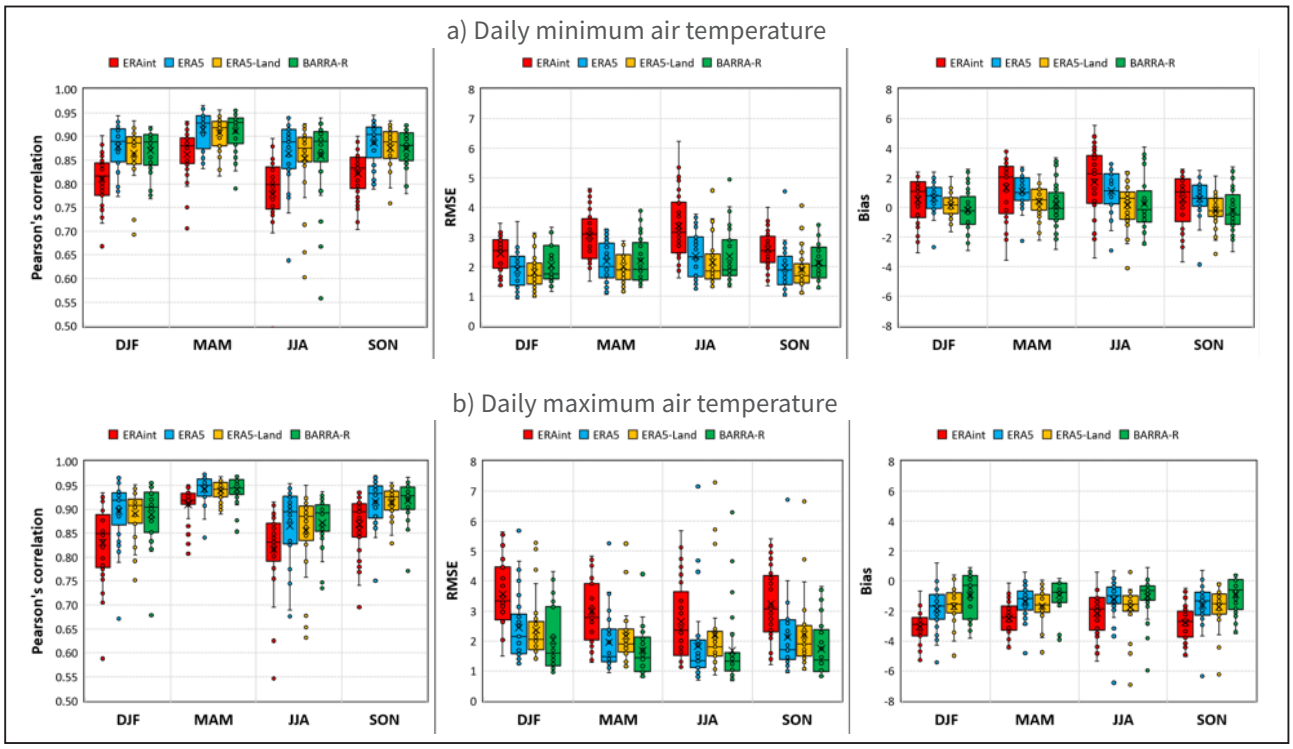

Figure 7: Box and Whisker plots showing the distribution of reanalysis products' evaluation scores relative to the stations in each season using observation data as reference for: (a) daily minimum air temperature; (b) daily maximum air temperature.

all seasons, but much more closely matched with ERA5-Land. This is most likely due to their similar horizontal resolutions of 12 and 9 km respectively, compared to the 31 km resolution of ERA5 and 80 km for ERA-Interim (Muñoz-Sabater et al., 2021).

Monthly mean differences of the reanalyses in daily maximum and minimum temperature with respect to VCSN over the period 2014 – 2018 averaged over all of New Zealand are shown in Figure 8. The highest inter-seasonal variations were seen for ERA-Interim and ERA5-Land maximum and minimum temperature, respectively, with a value of about 2°C. All the models show negative and positive average biases for the maximum and minimum daily temperatures, respectively. BARRA-R depicts lowest average bias values (–1°C and 0.5°C for maximum and minimum temperatures, respectively) and variations of around 1°C, followed by ERA5, which performs equally well for maximum temperature but is almost a degree warmer than BARRA-R for the minimum temperature. For BARRA-R maximum daily temperature, biases are reduced (i.e. closer to zero) during warmer months (i.e. Nov – Mar) while during colder months (May – Sep) BARRA-R shows larger negative biases. This trend is almost reversed in ERA5 and ERA-Interim estimates.

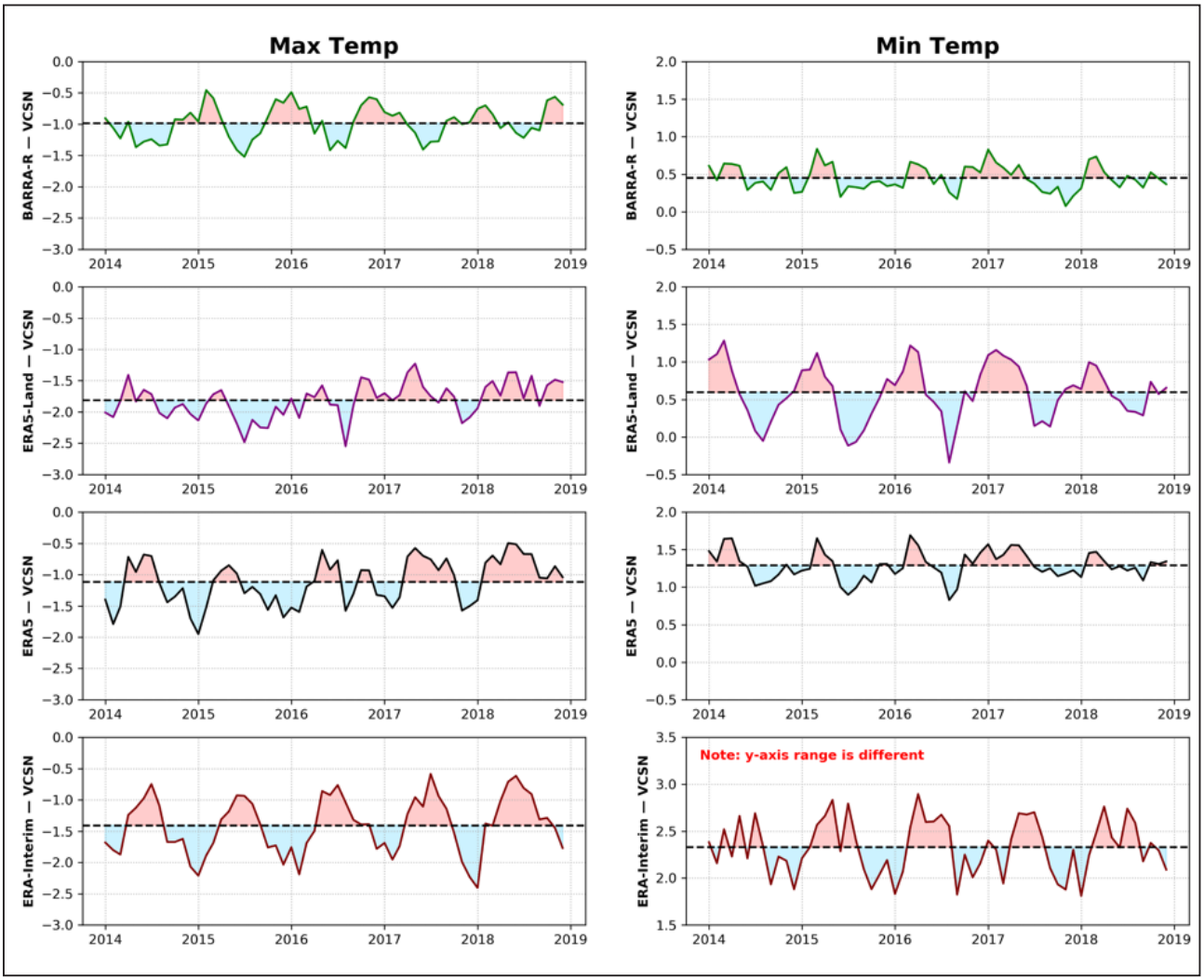

Figure 8: Monthly mean difference in daily maximum (left column) and minimum (right column) temperatures averaged over New Zealand with respect to VCSN. Black dashed lines are the mean values during 2014 – 2018. Note that ERA-Interim daily minimum temperature has different y-axis range.

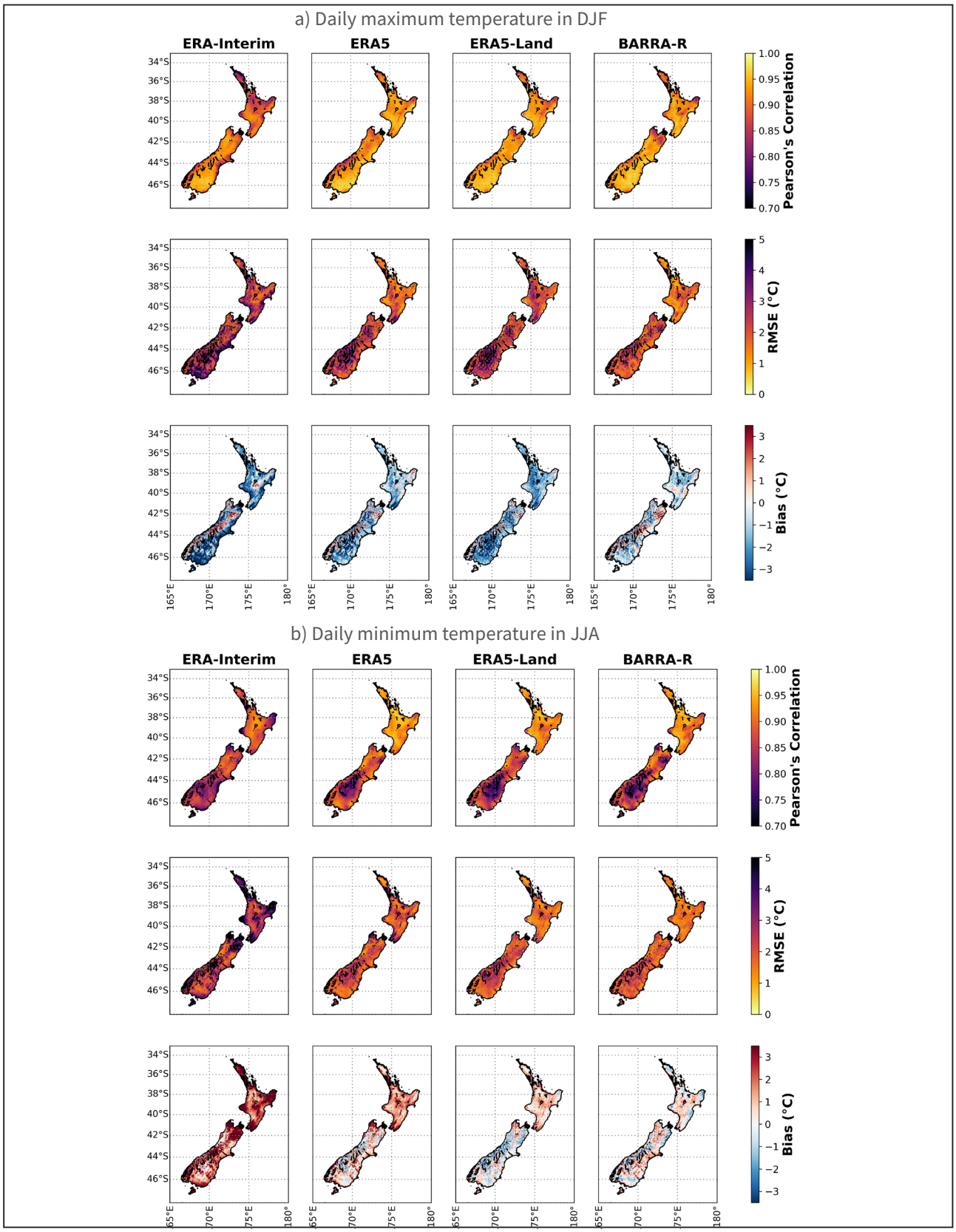

Figure 9: Statistical results calculated between VCSN and reanalyses for: (a) daily maximum temperature in DJF; (b) daily minimum temperature in JJA. First, 2nd, and 3rd rows are Pearson's correlation coefficients, RMSE and bias, respectively. The reanalyses are re-gridded onto the VCSN grid using the linear interpolation method.

The spatial variability of the reanalyses' performance, calculated with respect to VCSN, for maximum and minimum daily temperatures in summer (Dec to Feb, DJF) and winter (Jun to Aug, JJA) are shown in Figures 9a and 9b, respectively. For maximum daily temperature (Figure 9a), ERA-Interim has the lowest correlation overall and highest RMSE and bias (negative) values. BARRA-R generally outperforms the two ERA5 reanalyses at most locations, particularly over areas of complex terrain such as the Southern Alps and Central Plateau, but struggles in the Marlborough region. BARRA-R has the lowest biases ranging from –1°C to 1°C over the NI and most parts of the SI. There is a generally cool bias in the maximum temperature over most New Zealand for all models with biases typically colder than –1°C.

Pearson Correlation scores are significantly lower for all reanalysis products for minimum temperature (Figure 9b), especially over high orography such as the Southern Alps. Compared to the warm bias of BARRA-R, ERA5-Land is generally too cold over the SI and too warm over the NI. ERA5 and ERA5-Land display a more marked warm bias over the NI compared to the SI. ERA-Interim is too warm over all of NZ and coupled with its maximum temperature bias (Figure 9a), it suggests that this reanalysis is not capturing the full range of observed seasonal temperature ranges. It is evident that BARRA-R outperforms its driving model, ERA-Interim, and shows considerably smaller negative (positive) bias values for maximum (minimum) daily temperatures.

3.3. Mean and gust wind speed

For the five NZ regions (Figure 1), Figure 10 depicts the seasonal cycles, defined as the monthly averages of mean wind speed (Figure 10a) and maximum daily gust wind speeds (Figure 10b), for the point-based observations and all the considered reanalysis datasets.

ERA-Interim considerably overestimates the seasonal cycles of mean wind speed (Figure 10a) in all the wind regions (except for NZ3), by up to about 2 m/s (NZ1 and NZ2) and 5 m/s (NZ4). For regions NZ1 and NZ2-North, ERA5, ERA5-Land and BARRA-R estimate monthly average mean wind speeds that are closer to the observations. In these two regions, ERA5 tends to slightly overestimate the seasonal cycle by about 0.5 m/s during Apr to Sep and during the rest of the months its predictions

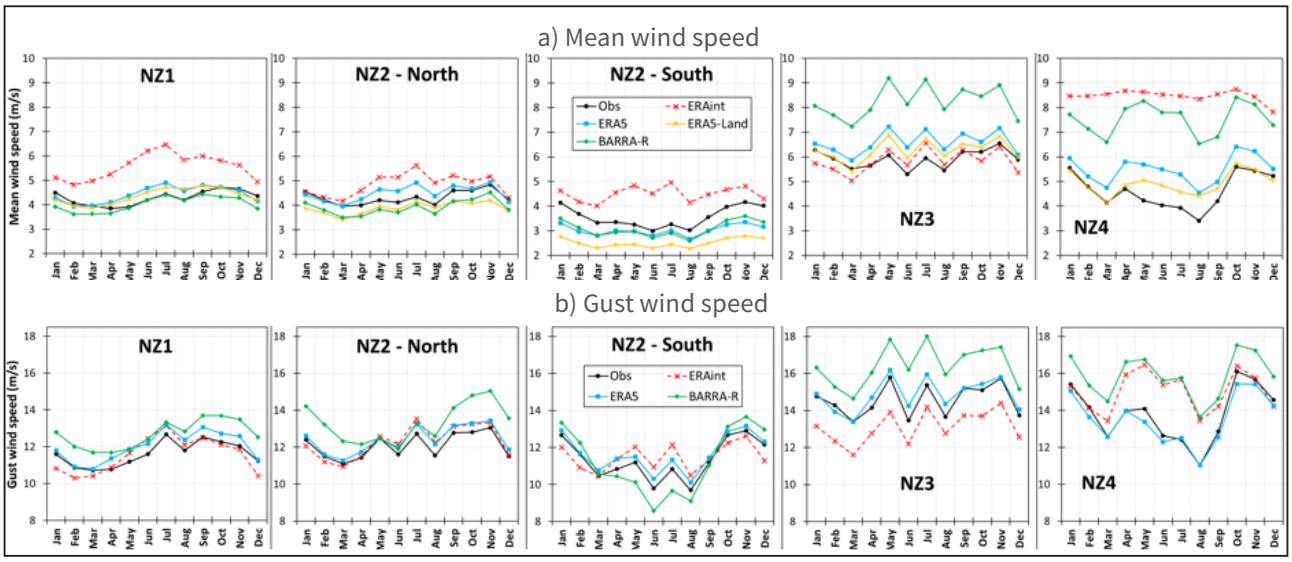

Figure 10: Average monthly cycle of mean wind speeds computed from observations and different reanalysis products for the five New Zealand wind regions for 2014 – 2018.

match the observations. Over the NZ2-South region, the estimates of BARRA-R and ERA5 are very close to one another and both slightly (about 0.5 m/s) underestimate the monthly averages. For NZ3 and NZ4, BARRA-R significantly overestimates (up to 4 m/s) the monthly averages of mean wind speed, while ERA5 and ERA5-Land provide better predictions, which are generally within 1 m/s of the observations. Overestimation of BARRA-R in this coastal region is likely to be because the closest grid point is not a land point as shown in Figure 2.

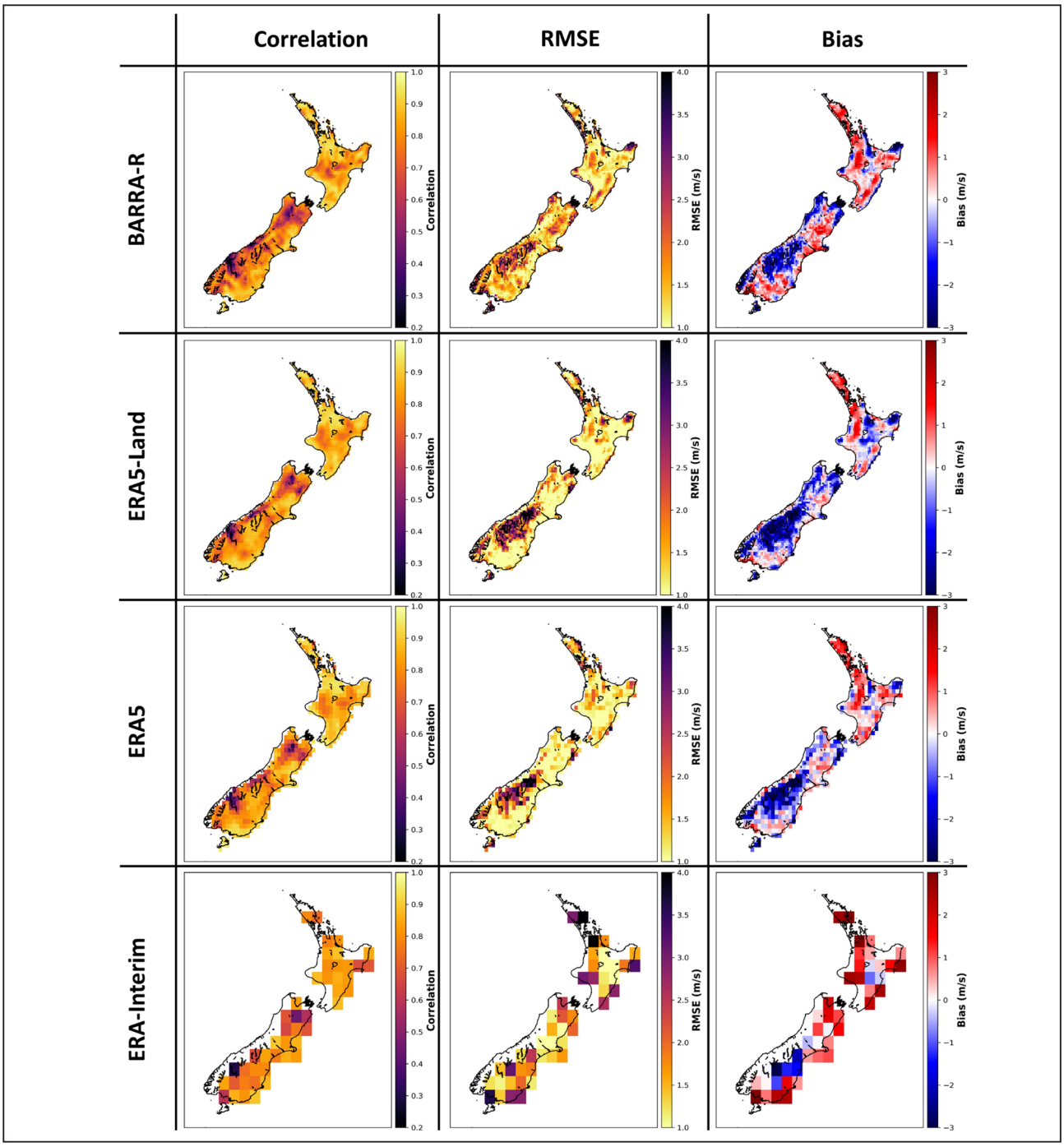

Figure 11: Statistical results calculated between VCSN and reanalysis data for mean wind speed for 2014 – 2018. First, 2nd, 3rd and 4th rows show the comparison between VCSN and BARRA-R, ERA5-Land, ERA5 and ERA-Interim, respectively. Also, the left, middle and right columns are Pearson's correlation coefficients, RMSE and bias, respectively.

As can be seen in Figure 10b, in all the wind regions, ERA5 estimated the seasonal cycles of gust wind speeds more accurately. ERA-Interim also showed acceptable predictions of the seasonal cycles in regions NZ1, NZ2-North and NZ2-South, with differences being around 0.5 m/s reaching to 1 m/s in NZ2-South region during Apr to Jul. However, ERA-Interim performs poorly in NZ3 (underestimate) and NZ4 (overestimate) regions. BARRA-R continues to perform poorly in the coastal NZ3 and NZ4 regions, overestimating the seasonal gust wind speeds in all months by up to 2 – 2.5 m/s. In region NZ1, BARRA-R overestimates the monthly means by about 1 m/s and 1.5 – 2 m/s during Jan to Apr and Sep to Dec, respectively. Similar trends can also be seen for NZ2-North, with slightly larger differences. However, in NZ2-South this trend is reversed with BARRA-R agreeing well with observations during Apr to Aug, while for the other months the difference increases to 2 m/s.

As for precipitation and temperature above, VCSN provides a spatially complete observation-based records that can be used for the verification of the simulated wind speed in the reanalysis datasets. Figure 11 shows statistical results computed between VCSN and the reanalysis data for mean wind speed. Generally, higher correlation scores occur over areas of relatively flat terrain (e.g. north of NI, east and southeast regions of SI). This is very likely a result of validating against VCSN which relies on New Zealand's observation station network with very few sites located in areas of high altitude, and is therefore heavily reliant on the interpolation and spline methods used to create a complete surface (Tait et al., 2012).

Figure 12 compares the frequency of daily gust wind speeds exceeding 25 m/s. Unlike ERA-Interim, ERA5 and BARRA-R, due to their higher spatial resolutions, better estimate the higher gust wind speeds, and consequently higher occurrence frequencies, which appear more realistic in comparison with the predictions of New Zealand's high-resolution (1.5 km) convective scale model (Safaei Pirooz et al., 2020b). This is particularly evident over the mountains of the SI and NI as well as high wind speeds in Cook Strait. It is noteworthy that BARRA-R, unlike ERA5, does not capture the high gust wind speeds over the more southern mountains of the SI, but does produce higher gust speeds in the lower NI.

To further investigate and verify the performances of the reanalysis products against observations, Figure 13 illustrates correlations between the reanalysed and observed maximum daily gust wind speeds as well as their distributions for a selection of stations. As can be seen, in most cases, BARRA-R overestimates the maximum daily gust wind speeds (see also Figure 10b) resulting

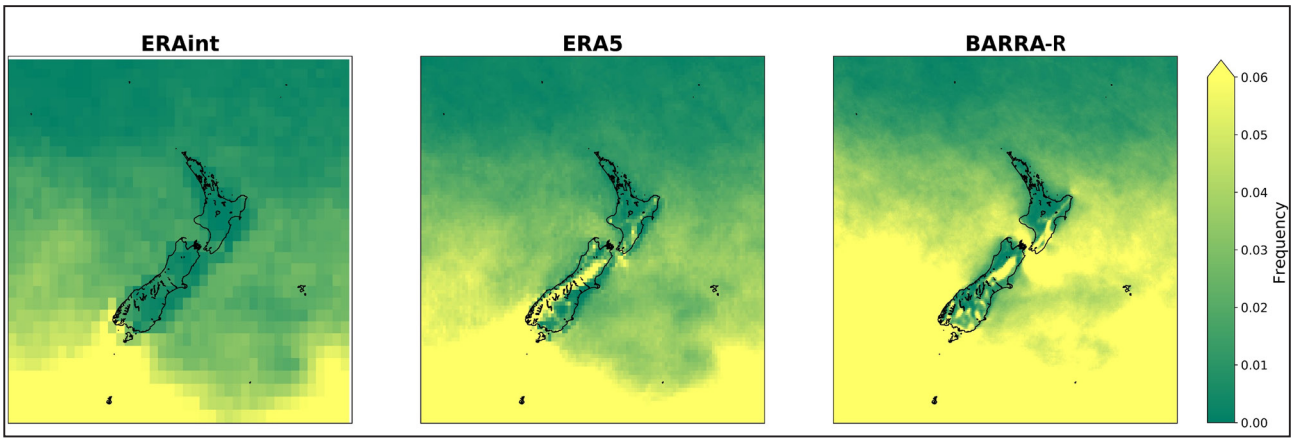

Figure 12: Proportion of gust wind speeds greater than 25 m/s over New Zealand for the period 2014 – 2018. (left) ERA-Interim, (middle) ERA5 and (right) BARRA-R.

in skewness of BARRA-R distributions towards higher gust wind speeds. This shift in the distributions can be clearly seen in stations such as Auckland, Wellington, and Christchurch. This overestimation of gust wind speeds can influence future studies that are mainly based on the upper tail of the distribution, such as extreme value analysis for the estimation of design wind speeds, or the investigation of trends in frequency and magnitude of extreme winds.

On the other hand, ERA-Interim generally tends to underestimate the gust wind speeds. However, ERA5 seems to represent the distribution of gust wind speeds more accurately, particularly in terms of the location of the peak of the distribution. It should also be noted that in regions near complex terrain (e.g. Middlemarch), or high-wind locations (e.g. Cook and Foveaux Straits), the discrepancies between the observation and reanalyses increases, resulting in more scattered correlations.

3.4. Summary point-based results

Figure 14 summarises the distribution of statistical metrics calculated for reanalysis variables against point-based station observations within each region. Note that in regions NZ3 and NZ4, the number of stations is limited, and stations are located close to each other. This leads to less scattered statistical scores and may make results in these regions less robust.

For mean and gust wind speeds, Figures 14a and 14b show that ERA-Interim generally has lower mean Pearson's coefficients, and higher RMSE and bias (generally positive) values at most station locations. BARRA-R generally shows better agreement with the observation data, except in regions NZ3 and NZ4, NZ's windiest regions climatologically, where BARRA-R's bias and RMSE values are higher than those of ERA5 and ERA5-Land. Also, in the NZ2-North region, BARRA-R shows a more scattered RMSE and bias distributions, while its average RMSE and bias values are close to ERA5 and

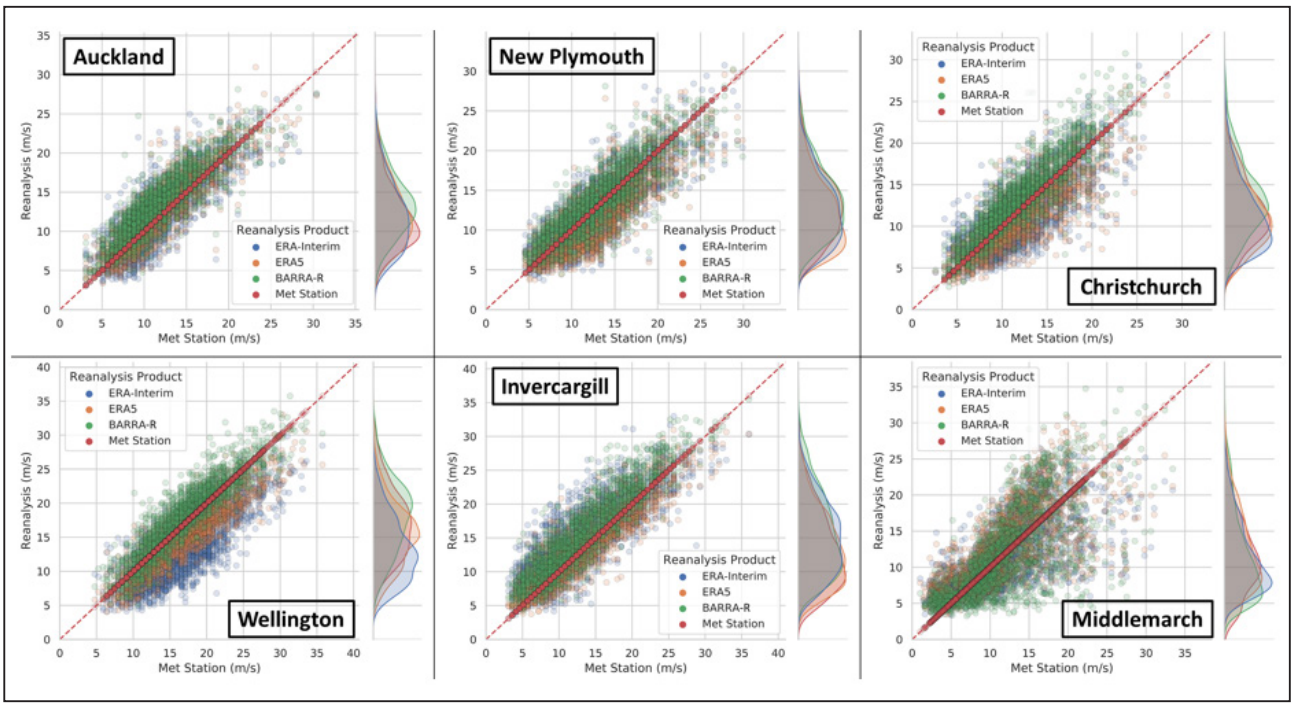

Figure 13: Plots of linear correlation between the observed and reanalysed maximum daily gust wind speeds along with the distribution of each dataset for a selected number of stations.

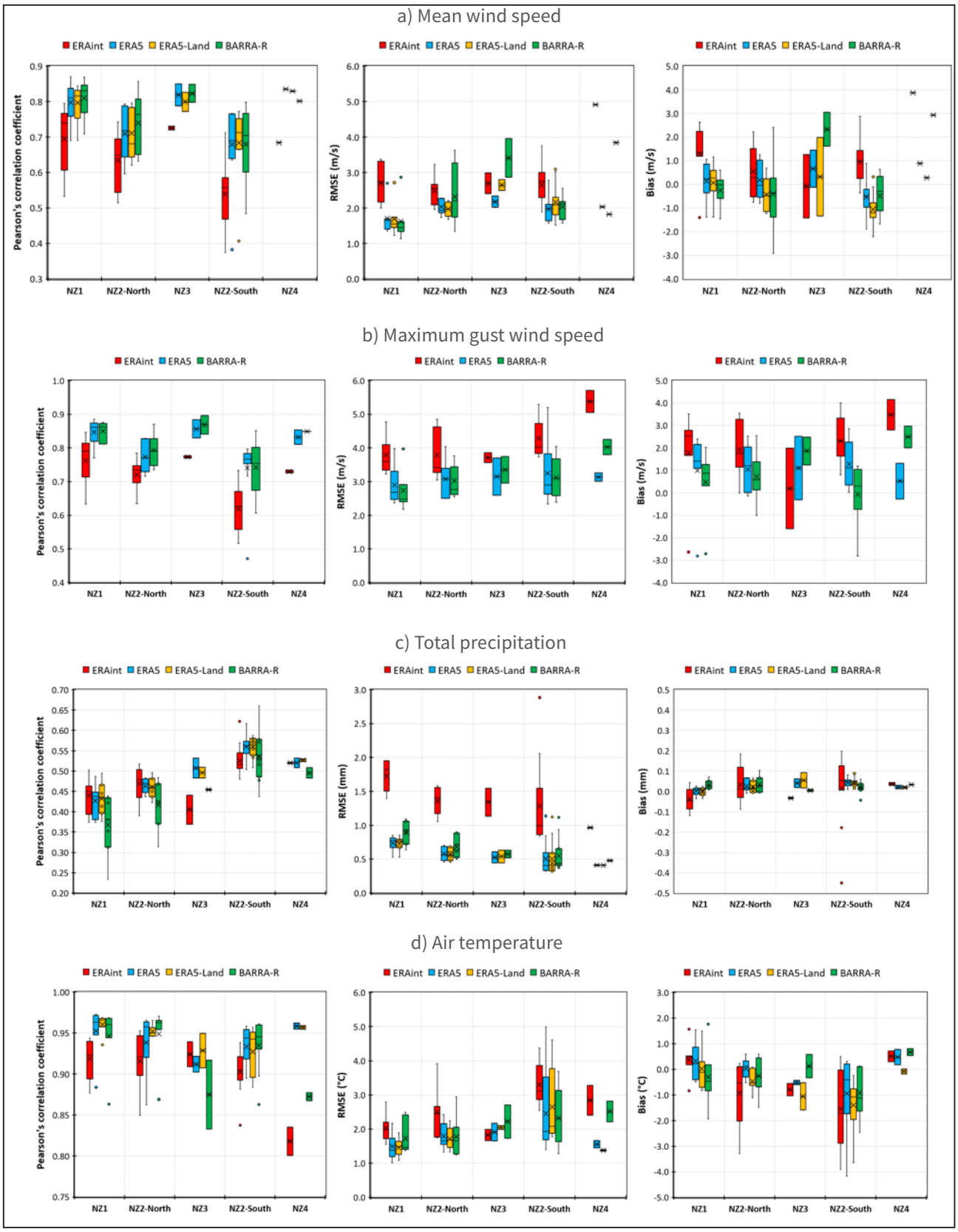

Figure 14: Box and Whisker plots showing the distribution of reanalysis products evaluation scores using hourly (3-hourly for ERA-Interim) data for: (a) mean wind speed; (b) daily gust wind speed; (c) total precipitation; (d) air temperature.

ERA5-Land. It should be noted that ERA5-Land does not provide gust wind speed data.

For total precipitation (Figure 14c), although ERA-Interim depicts the highest RMSE values with respect to the point observations in all the regions, its Pearson's coefficients and bias values are relatively close to those of the other reanalyses. ERA5, ERA5-Land and BARRA-R show quite similar scores, such that the average and median values of the scores are close across the New Zealand regions. However, in some cases, ERA5 and ERA5-Land depict better performance. For instance, in NZ1 region, BARRA-R shows more scattered correlations and higher RMSE and bias values. Similarly, for NZ2-North region, BARRA-R has slightly higher RMSE and bias. On the other hand, BARRA-R depicts lower RMSE and bias values in regions NZ3 and NZ2-South. ERA5 and ERA5-Land generally show higher correlations and lower RMSE values compared with BARRA-R, particularly over NI. In terms of mean bias, all the three products are positively biased at most station locations. Over SI, BARRA-R depicts slightly lower bias values, while in NI, especially at Hicks Bay and northern part of the island, BARRA-R has higher bias values. The overall performances of BARRA-R, ERA5 and ERA5-Land are quite similar (as also seen in Figure 7 of Su et al., 2021). However, at some locations, for example Auckland, Taupo (centre of NI), Cape Reinga (North of the NI) and Hicks Bay, ERA5 and ERA5-Land show slightly better scores.

The statistical metrics calculated using hourly air temperature between station observations and the reanalyses for each region in New Zealand are shown in Figure 14d. ERA-Interim shows the lowest correlations and more scattered RMSE and bias values. ERA5, ERA5-Land and BARRA-R depict correlations of higher than 0.9 and around 0.95, except for in regions NZ3 and NZ4, where BARRA-R's average correlations drop to 0.87. However, a possible explanation for lower correlation in NZ3 by BARRA-R could be that the closest BARRA-R grid point to one of the two stations in this region (i.e. Paraparaumu) is on water. In the NZ2-South region (mountainous region) all the reanalysis products show scattered RMSE and bias values. The bias and RMSE values of the reanalyses generally range from −1°C to +1°C and 1°C to 3°C, except in region NZ2-South, respectively.

4. Conclusion

The ability and accuracy of three global and one regional reanalysis products to capture the meteorological variability of New Zealand were evaluated using point-based and gridded observational data. ERA-Interim was outperformed by all the other reanalyses considered in this study. ERA5 and ERA5-Land generally showed a similar performance with slight discrepancies, which could be attributed to several factors. Although ERA5-Land has a higher spatial resolution, unlike ERA5, it uses indirect data assimilation of observational data and also lacks atmosphere coupling. The performance of all the models investigated here decayed over complex and mountainous regions.

The statistical and climatological metrics used in this study demonstrate that the higher resolution regional reanalysis model, BARRA-R, presents a significant improvement compared to the global reanalyses studied. Most notably, BARRA-R, unlike the ERA datasets, successfully captured the high rainfall characteristics over the western parts of the SI, including more accurately simulating the frequency of very high rain days. It was shown that the slightly weaker statistical scores of BARRA-R in coastal areas could be attributed to the land-sea masks and the representation of part of the land as sea points. The results demonstrate that BARRA-R not only outperforms its driving model, ERA-Interim, but generally it performs better than ERA-Interim's successor, i.e. ERA5.

Su et al. (2021) showed that further downscaling of BARRA-R to 1.5 km horizontal resolution adds significant value over its coarser resolution driving model. Such a long-term high-resolution dataset does not currently exist

for NZ. The National Institute of Water and Atmospheric Research (NIWA) Ltd is currently preparing the New Zealand Reanalysis (NZRA) to create just such a dataset. Forced by BARRA data the NZRA will be available for the period 1991 to 2018 at 1.5 km horizontal resolution and cover all of New Zealand's land mass and coastal waters.

References

Ackerley, D., Dean, S., Sood, A., Mullan, A.B., (2012). Regional Climate Modelling in New Zealand: Comparison to Gridded and Satellite Observations. Weather and Climate, 32, 3-22.

Avila-Diaz, A., Benezoli, V., Justino, F., Torres, R., Wilson, A., (2020). Assessing current and future trends of climate extremes across Brazil based on reanalyses and earth system model projections. Climate Dynamics, 55, 1403-1426. https://doi.org/10.1007/s00382-020-05333-z

Cliflo, (2020). New Zealand's National Climate Database. https://cliflo.niwa.co.nz. Accessed in Sep 2020.

Davies, T., Cullen, M.J.P., Malcolm, A.J., Mawson, M.H., Staniforth, A., White, A.A., Wood, N., (2005). A new dynamical core of the Met Office's global and regional modelling of the atmosphere. Quarterly Journal of the Royal Meteorological Society, 131, 1759-1782. https://doi.org/10.1256/qj.04.101

Dee, D.P., Uppala, S.M., Simmons, A.J., Berrisford, P., Poli, P., Kobayashi, S., Andrae, U., Balmaseda, M.A., Balsamo, G., Bauer, P., Bechtold, P., Beljaars, A.C.M., van de Berg, L., Bidlot, J., Bormann, N., Delsol, C., Dragani, R., Fuentes, M., Geer, A.J., Haimberger, L., Healy, S.B., Hersbach, H., Hólm, E.V., Isaksen, L., Kållberg, P., Köhler, M., Matricardi, M., McNally, A.P., Monge-Sanz, B., Morcrette, J.J., Park, B.K., Peubey, C., de Rosnay, P., Tavolato, C., Thépaut, J.N., Vitart, F., (2011). The ERA-Interim reanalysis: configuration and performance of the data assimilation system. Quarterly Journal of the Royal Meteorological Society, 137, 553-597. https://doi.org/10.1002/qj.828

Di Virgilio, G., Evans, J.P., Di Luca, A., Olson, R., Argüeso, D., Kala, J., Andrys, J., Hoffmann, P., Katzfey, J.J., Rockel, B., (2019). Evaluating reanalysis-driven CORDEX regional climate models over Australia: model performance and errors. Climate Dynamics, 53, 2985-3005. https://doi.org/10.1007/s00382-019-04672-w

Essou, G.R.C., Brissette, F.o., Lucas-Picher, P., (2017). The Use of Reanalyses and Gridded Observations as Weather Input Data for a Hydrological Model: Comparison of Performances of Simulated River Flows Based on the Density of Weather Stations. Journal of Hydrometeorology, 18, 497-513. https://doi.org/10.1175/jhm-d-16-0088.1

Frank, C.W., Wahl, S., Keller, J.D., Pospichal, B., Hense, A., Crewell, S., (2018). Bias correction of a novel European reanalysis data set for solar energy applications. Solar Energy, 164, 12-24. https://doi.org/10.1016/j.solener.2018.02.012

GLOBE Task Team, (1999). The Global Land One-kilometre Base Elevation (GLOBE) Digital Elevation Model, Version 1.0, in: Hastings, D.A., Dunbar, P.K., Elphingstone, G.M., Bootz, M., Murakami, H., Maruyama, H., Masaharu, H., Holland, P., Payne, J., Bryant, N.A., Logan, T.L., Muller, J.P., Schreier, G., John, S.M. (Eds.). National Oceanic and Atmospheric Administration, National Geophysical Data Center, 325 Broadway, Boulder, Colorado 80305-3328, U.S.A.

Hersbach, H., Bell, B., Berrisford, P., Hirahara, S., Horányi, A., Muñoz-Sabater, J., Nicolas, J., Peubey, C., Radu, R., Schepers, D., Simmons, A., Soci, C., Abdalla, S., Abellan, X., Balsamo, G., Bechtold, P., Biavati, G., Bidlot, J., Bonavita, M., De Chiara, G., Dahlgren, P., Dee, D., Diamantakis, M., Dragani, R., Flemming, J., Forbes, R., Fuentes, M., Geer, A., Haimberger, L., Healy, S., Hogan, R.J., Hólm, E., Janisková, M., Keeley, S., Laloyaux, P., Lopez, P., Lupu, C., Radnoti, G., de Rosnay, P., Rozum, I., Vamborg, F., Villaume, S., Thépaut, J.-N., (2020). The ERA5 global reanalysis. Quarterly Journal of the Royal Meteorological Society, 146, 1999-2049. https://doi.org/10.1002/qj.3803

Jermey, P.M., Renshaw, R.J., (2016). Precipitation representation over a two-year period in regional reanalysis. Quarterly Journal of the Royal Meteorological Society, 142, 1300-1310. https://doi.org/10.1002/qj.2733

Miao, H., Dong, D., Huang, G., Hu, K., Tian, Q., Gong, Y., (2020). Evaluation of Northern Hemisphere surface wind speed and wind power density in multiple reanalysis datasets. Energy, 200, 117382. https://doi.org/10.1016/j.energy.2020.117382

Minola, L., Zhang, F., Azorin-Molina, C., Pirooz, A.A.S., Flay,

R.G.J., Hersbach, H., Chen, D., (2020). Near-surface mean and gust wind speeds in ERA5 across Sweden: towards an improved gust parametrization. Climate Dynamics, 55, 887-907. https://doi.org/10.1007/s00382-020-05302-6

Mo, H.M., Hong, H.P., Fan, F., (2015). Estimating the extreme wind speed for regions in China using surface wind observations and reanalysis data. Journal of Wind Engineering and Industrial Aerodynamics, 143, 19-33. https://doi.org/10.1016/j.jweia.2015.04.005

Muñoz-Sabater, J., Dutra, E., Agustí-Panareda, A., Albergel, C., Arduini, G., Balsamo, G., Boussetta, S., Choulga, M., Harrigan, S., Hersbach, H., Martens, B., Miralles, D.G., Piles, M., Rodríguez-Fernández, N.J., Zsoter, E., Buontempo, C., Thépaut, J.N., (2021). ERA5-Land: A state-of-the-art global reanalysis dataset for land applications. Earth System Science Data Discussion, 2021, 1-50. https://doi.org/10.5194/essd-2021-82

Muñoz Sabater, J., (2019). ERA5-Land hourly data from 1981 to present. https://doi.org/10.24381/cds.e2161bac.

Safaei Pirooz, A.A., Flay, R.G.J., Minola, L., Azorin-Molina, C., Chen, D., (2020a). Effects of sensor response and moving average filter duration on maximum wind gust measurements. Journal of Wind Engineering and Industrial Aerodynamics, 206, 104354. https://doi.org/10.1016/j.jweia.2020.104354

Safaei Pirooz, A.A., Flay, R.G.J., Turner, R., (2020b). New Zealand design wind speeds, directional and lee-zone multipliers proposed for AS/NZS 1170.2:2021. Journal of Wind Engineering and Industrial Aerodynamics, 208. https://doi.org/10.1016/j.jweia.2020.104412

Su, C.H., Eizenberg, N., Jakob, D., Fox-Hughes, P., Steinle, P., White, C.J., Franklin, C., (2021). BARRA v1.0: kilometre-scale downscaling of an Australian regional atmospheric reanalysis over four midlatitude domains. Geoscientific Model Development, 14, 4357-4378. https://doi.org/10.5194/gmd-14-4357-2021

Su, C.H., Eizenberg, N., Steinle, P., Jakob, D., Fox-Hughes, P., White, C.J., Rennie, S., Franklin, C., Dharssi, I., Zhu, H., (2019). BARRA v1.0: the Bureau of Meteorology Atmospheric high-resolution Regional Reanalysis for Australia. Geoscientific Model Development, 12, 2049-2068. https://doi.org/10.5194/gmd-12-2049-2019

Tait, A., Henderson, R., Turner, R., Zheng, X., (2006). Thin plate smoothing spline interpolation of daily rainfall for New Zealand using a climatological rainfall surface. International Journal of Climatology, 26, 2097-2115. https://doi.org/10.1002/joc.1350

Tait, A., Sturman, J., Clark, M., (2012). An assessment of the accuracy of interpolated daily rainfall for New Zealand. Journal of Hydrology (NZ), 51, 25-44.

Tait, A., Turner, R., (2005). Generating Multiyear Gridded Daily Rainfall over New Zealand. Journal of Applied Meteorology, 44, 1315-1323.

Tetzner, D., Thomas, E., Allen, C., (2019). A Validation of ERA5 Reanalysis Data in the Southern Antarctic Peninsula—Ellsworth Land Region, and Its Implications for Ice Core Studies. Geosciences, 9, 289. https://doi.org/10.3390/geosciences9070289

Turner, R., Safaei Pirooz, A.A., Flay, R.G.J., Moore, S., Revell, M., (2019). Use of High-Resolution Numerical Models and Statistical Approaches to Understand New Zealand Historical Wind Speed and Gust Climatologies. Journal of Applied Meteorology and Climatology, 58, 1195-1218. https://doi.org/10.1175/JAMC-D-18-0347.1

Uppala, S.M., KÅllberg, P.W., Simmons, A.J., Andrae, U., Bechtold, V.D.C., Fiorino, M., Gibson, J.K., Haseler, J., Hernandez, A., Kelly, G.A., Li, X., Onogi, K., Saarinen, S., Sokka, N., Allan, R.P., Andersson, E., Arpe, K., Balmaseda, M.A., Beljaars, A.C.M., Berg, L.V.D., Bidlot, J., Bormann, N., Caires, S., Chevallier, F., Dethof, A., Dragosavac, M., Fisher, M., Fuentes, M., Hagemann, S., Hólm, E., Hoskins, B.J., Isaksen, L., Janssen, P.A.E.M., Jenne, R., Mcnally, A.P., Mahfouf, J.-F., Morcrette, J.-J., Rayner, N.A., Saunders, R.W., Simon, P., Sterl, A., Trenberth, K.E., Untch, A., Vasiljevic, D., Viterbo, P., Woollen, J., (2005). The ERA-40 re-analysis. Quarterly Journal of the Royal Meteorological Society, 131, 2961-3012. https://doi.org/10.1256/qj.04.176

World Meteorological Organisation, (2014). Guide to meteorological instruments and methods of observations, 8th ed. WMO, Geneva, Switzerland.

Xu, H., Lin, N.A.m.a., Huang, M.A.m.a., Lou, W.P., (2020). Design Tropical Cyclone Wind Speed when Considering Climate Change. Journal of Structural Engineering (United States), 146. https://doi.org/10.1061/(ASCE)ST.1943-541X.0002585

Simulations of seasonal snowpack duration and water storage across New Zealand

J. Conway[1], T. Carey-Smith[2], C. Cattoën-Gilbert[3], S. Moore[2], P. Sirguey[4] and C. Zammit[3]

[1]NIWA-Taihoro Nukurangi, SH 85, Lauder, Aotearoa New Zealand
[2]NIWA-Taihoro Nukurangi, 301 Evans Bay Parade, Ākautangi, Hātaitai, Wellington, Aotearoa New Zealand
[3]NIWA-Taihoro Nukurangi, 10 Kyle Street, Riccarton, Christchurch, Aotearoa New Zealand
[4]School of Surveying, University of Otago, Dunedin, Aotearoa New Zealand

Correspondence: Jono.Conway@niwa.co.nz

Key words: snow, snowmelt, MODIS, numerical weather prediction

Abstract

Seasonal snow dramatically alters surface-atmosphere exchanges of heat and moisture, particularly in the South Island of New Zealand. Despite this, detailed simulations of seasonal snow and comparisons to remotely sensed snow observations are lacking in New Zealand, partly due to uncertainties in near-surface meteorology in mountainous areas with sparse in-situ observations. Here we simulate seasonal snow cover and water storage across New Zealand on a 250 m x 250 m grid over a 3-year period (April 2017 to March 2020) with a simple snow model and near-surface meteorology extracted from the New Zealand Convective Scale Model (NZCSM). Simulations are validated against snow cover derived from MODerate Resolution Imaging Spectroradiometer (MODIS) satellite remote sensing observations. While NZCSM near-surface meteorology is generally colder and wetter than observations, we find that the spatial patterns and elevation distribution of simulated snow cover duration (SCD) agrees well with MODIS observations. Biases in SCD are found in areas, particularly the ranges east of the main divide, where simulated snow cover persists longer than observed. In contrast, alternate simulations using daily gridded observations of near-surface meteorology show a poor fit to MODIS SCD, with large areas having little or no simulated snow cover. The simulated seasonal cycle of New Zealand-wide total snow water storage shows a peak around 1 September equating to around half the long-term average monthly total rainfall for the South Island. The correspondence between simulated and MODIS snow covered area is found to be sensitive to the threshold used to define simulated snow cover, particular in early winter when widespread thin snow cover is common. To improve estimates of snow cover and water storage, future work should exploit new remote sensing products for validation and assimilation as well as disentangle uncertainties in snow model parameters and meteorological input using detailed meteorological and snow observations.

1. Introduction

The growth and recession of the seasonal snowpack dramatically changes surface-atmosphere exchanges of heat and moisture, as well as altering the seasonal distribution of streamflow. Satellite observations show that, on average, 20% of New Zealand is covered in snow throughout winter[1]. Despite this, analysis of published simulations of the distribution and seasonality of New Zealand's seasonal snowpack and comparison to remotely sensed snow cover are lacking. Fitzharris and Garr (1995) simulated the snowpack of the main hydroelectric catchments within the South Island, showing large interannual variability in total water storage. Clark et al.

Submitted: 16 August 2021
Accepted: 19 November 2021

[1]Average snow covered area between 1 June and 31 August
https://www.otago.ac.nz/surveying/potree/pub/mrc/projects/snotago/modis-snow-cover

(2009) presented simulations for the South Island of New Zealand, with a focus on model parameter sensitivity and validation against catchment water balance and point snow measurements. Hendrix et al. (2012) made simulations for all New Zealand with a focus on patterns of peak snow water equivalent (SWE). Kerr (2013) simulated the contribution of snowmelt to river flows across the South Island by calculating the fraction of precipitation falling as snowfall in each catchment. The Statistics NZ water accounts (Henderson et al., 2011) provide national- and regional-level estimates of total snow storage changes between 1st July each year, with the most recent accounts also including regional storage changes in quarterly periods, but no maximum storage values are given (Griffiths et al., 2021).

The paucity of simulations is partly due to the lack of near-surface meteorological observations in mountainous regions of New Zealand, despite recent efforts to install automatic weather stations at high elevations (Hendrix and Harper, 2013). The lack of observations hampers efforts to produce interpolated surface meteorology products and produces large uncertainties in the precipitation and temperature inputs that are critical to snow simulations (Tait et al., 2012; Tait and Macara, 2014). Lundquist et al. (2019) posit that meso-scale meteorological models are becoming more skilful in estimating mountain precipitation compared to traditional observational networks. In mountainous areas, meso-scale models greatly improve the representation of near-surface meteorology compared to reanalysis products (e.g. Alonso-González, E. et al. 2021). The New Zealand Convective Scale Model (NZCSM) is a meso-scale numerical weather prediction model with 1.5 km horizontal grid spacing that covers all of New Zealand and has produced weather forecasts since its operationalisation in 2014. The archive of NZCSM forecasts provides hourly near-surface meteorology fields that can be used as input to simulations of seasonal snowpack across New Zealand. At the same time, the availability of remotely sensed snow cover products has increased, and these products can be used to assess the reliability of simulations in areas without *in-situ* snowpack observations (e.g. Quéno et al., 2016).

Despite recent advances in observing snow cover, snow models provides a means to bridge the gap between routinely collected remotely sensed snow cover information (e.g. Redpath et al., 2019), which has good spatial and temporal coverage, but no snow depth or SWE information, and the site-specific snow depth and SWE data available at a limited number of sites (e.g. Porhemmat et al., 2020; 2021). Gridded snow information can also inform surface boundary conditions in meteorological models, snowpack state for rain-on-snow flooding, and quantify snow storage and melt in specific catchments. Therefore, improved simulations of seasonal snow cover will improve forecasts of streamflow, snow hazard and near-surface climate.

The aims of this paper are to 1. assess if NZCSM output has value as input to snow simulations, 2. evaluate national-scale model simulations against remotely sensed snow cover on common grid, and 3. present the timing and elevational distribution of simulated snow storage. Remotely sensed snow cover derived from MODerate Resolution Imaging Spectroradiometer (MODIS) satellite observations (Hall and Riggs, 2016) will be used to evaluate the quality of the simulations. There will be a focus on the typical snow cover dynamics as well as snow storage.

2. Methodology

The snow simulations were performed on a 250 m x 250 m square grid using the Clark et al. (2009) snow model. This empirical model requires only temperature and precipitation as input and calculates snowpack storage (in mm water equivalent (w.e.)) as the sum of snowfall and snowmelt over an hourly timestep. Snowfall is defined as precipitation falling below an air temperature threshold (Tacc). Snow melt occurs when air temperature exceeds a melt threshold (Tmelt), with the rate of melt depending on air temperature, season, time since snowfall and occurrence of rain-on-snow. Default values were used for all parameters (Table 1.; Clark et al., 2009).

Previous studies have identified that simulated snow is particularly sensitive to the temperature threshold for snowfall (e.g. Clark et al, 2009). The default value (1 °C) used here represents the most commonly used threshold in NZ modelling studies (Anderson et al., 2021; Conway and Cullen, 2016; Clark et al., 2009) and is congruent with physically based estimates of equal rain-snow partitioning (Harder and Pomeroy, 2013) for air close to saturation (90% relative humidity).

The air temperature and precipitation input were derived from the NZCSM forecast archive in two steps. In the first, archived surface meteorology was concatenated to form a continuous hourly timeseries from 1 April 2017 to 30 March 2020. Output from forecast hours 7 to 12 was used to avoid the reduced convective precipitation that occurs in the first few hours of each forecast (Cattoën et al., 2016). Earlier forecasts (April 2014 to March 2017) were not used as to avoid the discontinuity in surface meteorology introduced by a major update to the dynamics and physics schemes within NZCSM in mid-2017.

The second step was to reproject and bilinearly interpolate the surface meteorology from the NZCSM grid (a rotated pole projection with ~1.5 km horizontal grid spacing) to the snow model grid (250 m x 250 m square grid on New Zealand Transverse Mercator (NZTM) projection. The model grid was chosen to match the grid of the MODIS snow cover observations, as catchment-based spatial units (e.g. those NZ Water Model used in Statistics NZ water accounts) make direct validation against remotely sensed snow cover challenging. Differences in grid elevation were accounted for by lapsing NZCSM temperature down to sea level, bilinearly interpolating to the snow model grid, then lapsing back up to the snow model elevation. The interpolation was performed on-the-fly within the snow model using a constant lapse rate of 0.005 K m-1 which equates to the annual mean lapse rate from Norton (1985). Hourly snowfall and rainfall totals from NZCSM were combined into total precipitation, then bi-linearly interpolated without adjustment for elevation.

Simulations were made for three hydrological years (1 April – 30 March) ending in 2018, 2019 and 2020. Note the hydrological years are named by the year they end in, so most snow accumulation occurs in the calendar year before the name of the hydrological year.

Simulated snowpack was validated against daily MODIS MOD10A1 Collection 6 snow cover product (Hall and Riggs, 2016) that had been reprojected and cloud-gap filled. The reprojection from the original sinusoidal grid (SIN) to the NZTM snow model grid was performed using nearest neighbour interpolation. The 250 m x 250m grid was chosen for resampling MODIS observations as it better preserves the original data given the large distortion between SIN and NTM projection. The 250 m x 250m grid is also preferable to the NZCSM grid (~1.5 km

Table 1: Mean bias in near-surface air temperature from NZCSM to observed air temperature at all stations shown in Figure 1 and the 12 SIN sites. Bias shown here as (NZCSM minus observed).

Sites	Season	Daily min. air temperature	Daily max. air temperature	Mean air temperature
All stations	MAM	0.98	-1.55	-0.02
(n=343)	JJA	0.76	-1.34	-0.02
	SON	0.51	-1.48	-0.36
	DJF	0.62	-1.76	-0.45
SIN stations	MAM	-0.98	-1.52	-1.15
(n=12)	JJA	-1.25	-1.91	-1.21
	SON	-0.87	-1.68	-1.09
	DJF	-0.77	-1.29	-1.05

x 1.5km) for simulations as larger grid sizes will smooth terrain and change the hypsometry. The normalised difference snow index (NDSI) values from MOD10A were converted to fractional snow-covered area using Hall et al. (2007). Following Redpath et al. (2019), the cloud-gap filling implements the approach of temporal filtering proposed by Dozier et al. (2008) whereby a temporal smoothing spline is fitted through the valid data points for each grid point to produce a continuous record in time.

To compare the simulations to MODIS observations, binary snow cover maps were created for simulated and observed snow cover for each day. To derive simulated snow cover maps, a 30 mm w.e. threshold was used to define a binary snow cover from the modelled SWE at noon each day (Gascoin et al., 2015; Queno et al. 2016). Following Sirguey et al. (2009), a threshold of 50% fractional snow-covered area was used to classify MODIS observations as snow covered. The snow cover duration (SCD) in the MODIS and model products is simply the number of days classed as snow cover in each year for a given grid point. Similarly, the snow-covered area (SCA) is defined as the total area of grid points defined as having snow cover on each day. Grid points over water were excluded from the analysis by creating a mask from the MODIS data with a grid point being masked if it was flagged as ocean or inland water within the study period.

To test the sensitivity of the snow model output to a -1 °C bias in air temperature, a second 'Sensitivity' simulation was performed with Tacc = 0 °C and Tmelt = -1 °C. This is a reduction of 1 °C from those in the 'Default' simulation (Tacc = 1 °C and Tmelt = 0 °C) and simulates correcting a -1 C bias in air temperature input. The sensitivity of the model SCD to the model SWE threshold is also assessed by reanalysing the results with a 5 mm w.e. threshold, which equates to 5 cm fresh snow (at density of 100 kg m^{-3}) or 1 cm spring snow (at density of 100 kg m^{-3}). By comparison, 30 mm w.e. equates to 30 cm fresh snow or 6 cm spring snow.

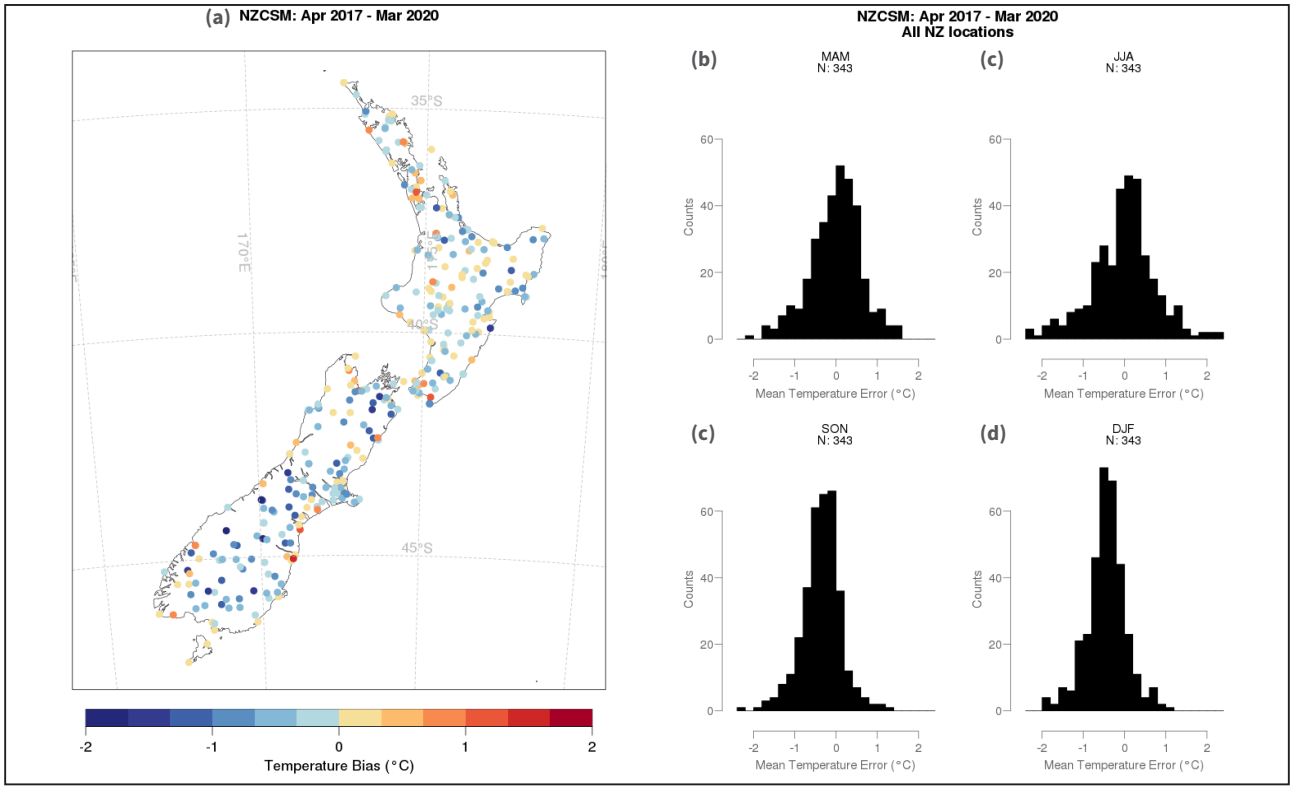

Figure 1: Comparison of near-surface air temperature from NZCSM to observations at selected sites (n=343): (a) mean bias April 2017 - March 2020, (b-e) histograms of biases at all stations by season.

3. Results

3.1 Comparison of NZCSM near-surface meteorology to observed climate

Comparison of NZCSM near-surface air temperature to a climate station records (Table 1, Figure 1b) shows biases are centred around zero for autumn and winter but show negative biases (model less than observations) in spring and summer. High-elevation SIN sites have more negative bias around -1 °C in all seasons (Table 1) and some sites have annual air temperature biases up to -2 °C in the central Southern Alps. We note these biases are similar to meso-scale model output used in similar snow model efforts internationally (e.g. Alonso-González et al. 2021). The larger negative bias at the SIN sites compared with all stations appears to be due to differences in the negative daily minimum temperature bias. The minimum temperature bias at SIN sites is quite different from the overall minimum temperature bias which is positive when averaged over all stations. The cause of this difference isn't clear but may be due to poor representation of surface-atmosphere exchange processes at high elevations, particularly during the night.

Precipitation totals from NZCSM are generally higher than observations, with biases of a few 10s of percent across much of the inland areas of the South Island (Figure 2a). A distinct west-east gradient is also apparent, with precipitation totals at sites on the West Coast, upwind of prevailing westerly airflow, being lower than observations and sites to the east above normal. A cluster of sites in Central Otago have the largest percentage differences from observations, where low precipitation totals make

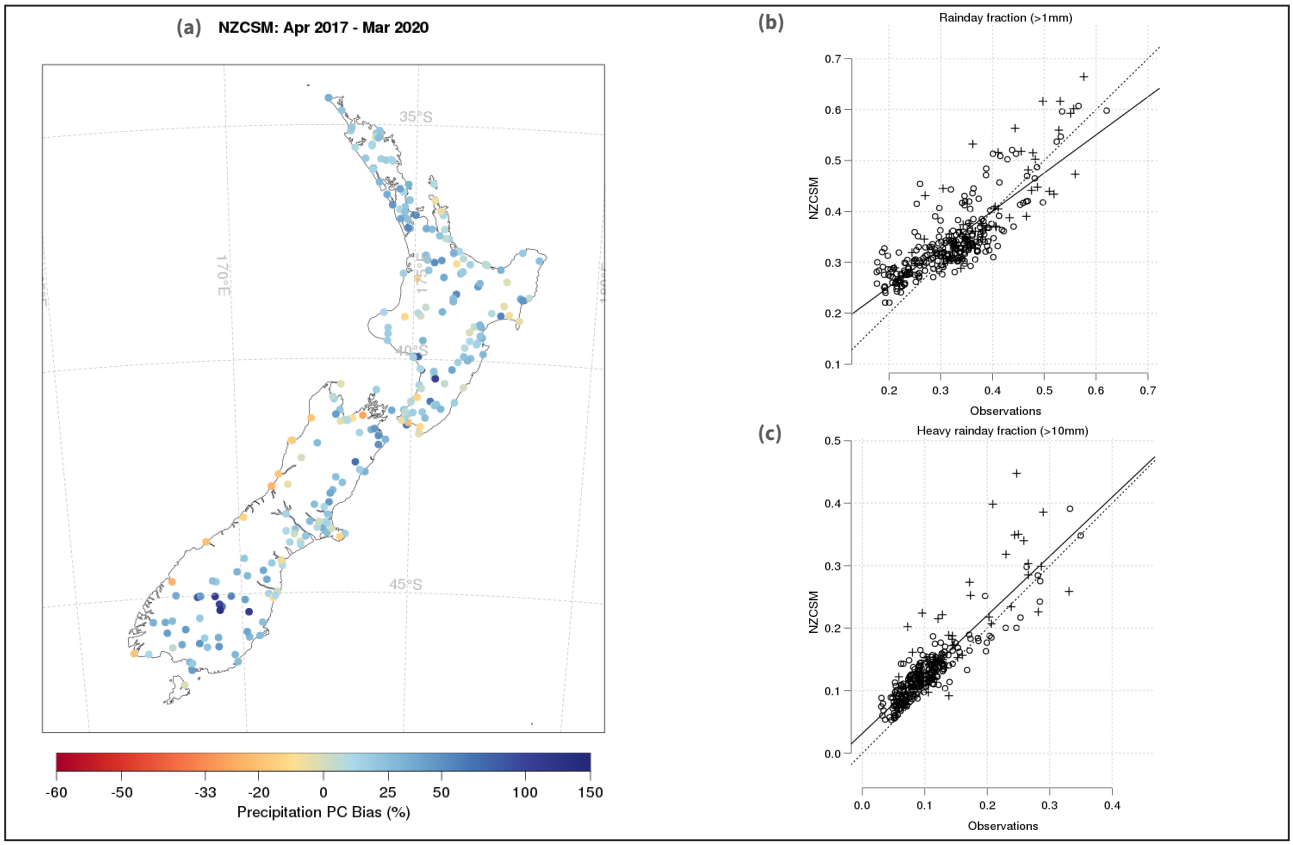

Figure 2: Comparison of total precipitation from NZCSM to observed rainfall at selected sites: (a) percent bias in total precipitation (n=267), (b) rainday (daily totals > 1mm) fraction and (c) heavy rainday (daily totals >10 mm) fraction, with sites > 500 m a.s.l. (n=51) shown as crosses. SIN sites are not included in the precipitation comparison, as the observations are unreliable during winter due to freezing.

percentage differences comparatively large. The fraction of heavy-rain days (daily totals >10 mm) in NZCSM is consistent with observations (Figure 2c). The higher fraction of rain days (daily totals >1 mm) in NZCSM at drier sites indicates too frequent light rain in NZCSM, a pattern often seen in numerical weather prediction model output (Blacutt et al., 2015).

3.2 Snow cover duration

The pattern of simulated mean annual snow cover duration (SCD) illustrates the stark contrast between snow cover in the North and South Islands (Figure 3). SCD greater than 1 or 2 months is widespread within the South Island, even outside the Southern Alps, while significant snow cover is limited to the tops of the ranges in the Lower North Island. MODIS observations show similar patterns (Figure 4c, d) but with longer SCD in low elevation areas within Fiordland and the West Coast (Figure 4e). The simulations show longer SCD in some of the more eastern mountain ranges in Otago and Southland, particularly the Takitimu and Remarkables/Hector Mountains, as well as areas within the Nelson Lakes and Kaikōura Ranges. It is likely that small values of SCD across patchy areas in Coastal Otago, Fiordland and the West Coast are a result of cloud shadows that appear to be often misclassified as partial snow cover within MODIS products. This feature is quite apparent in the North Island as a low bias in SCD in areas outside the main ranges (Figure 4f). Within the North Island, the spatial patterns of snow cover are represented well by the model, albeit being more clearly defined by topography compared to MODIS. Note that east of Mt Ruapehu (area of maximum SCD at centre top of Figure 4b), a large area has been masked as water (grey colouring) due to spurious inland water points within MODIS.

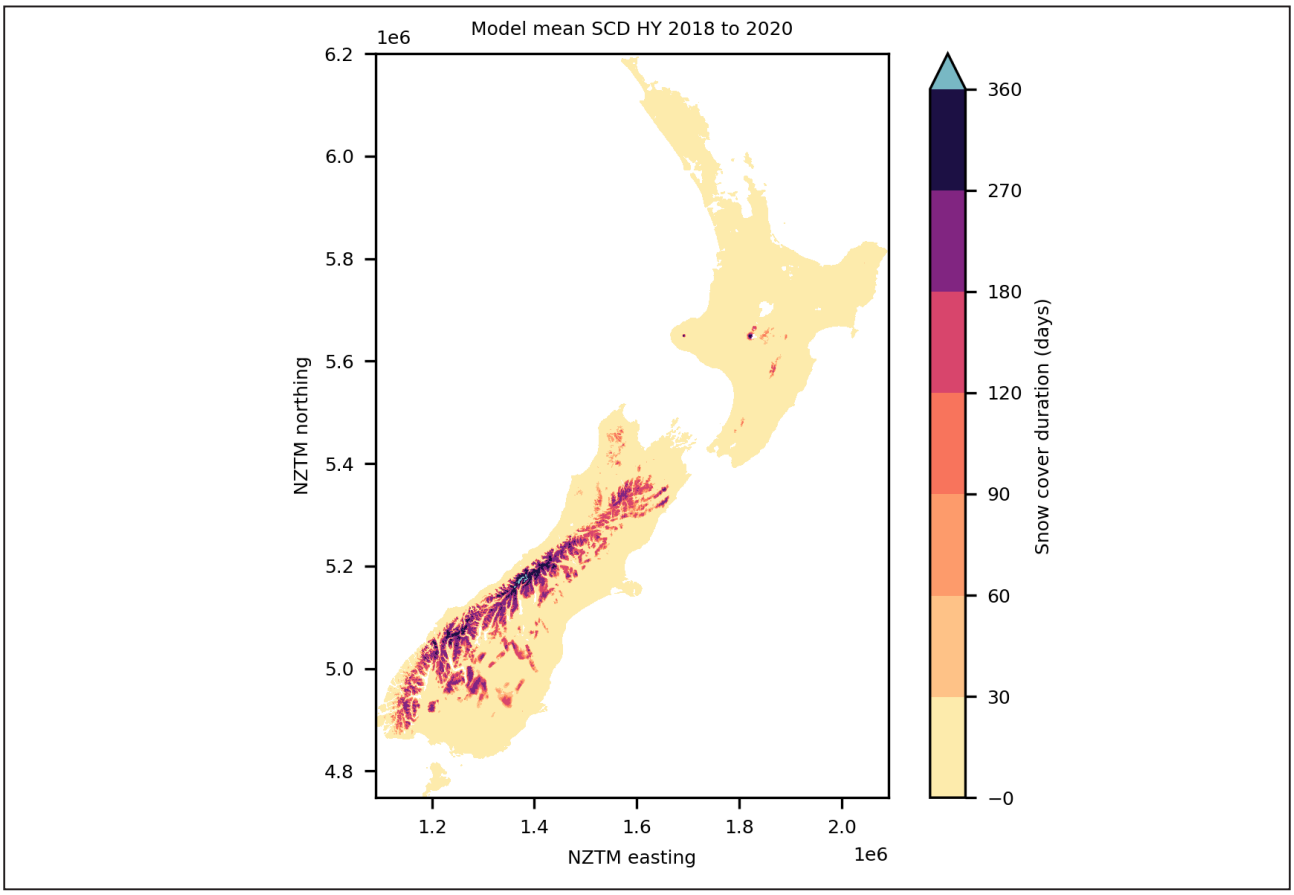

Figure 3: Annual mean simulated snow cover duration (SCD), 1 April 2017 – 30 March 2020.

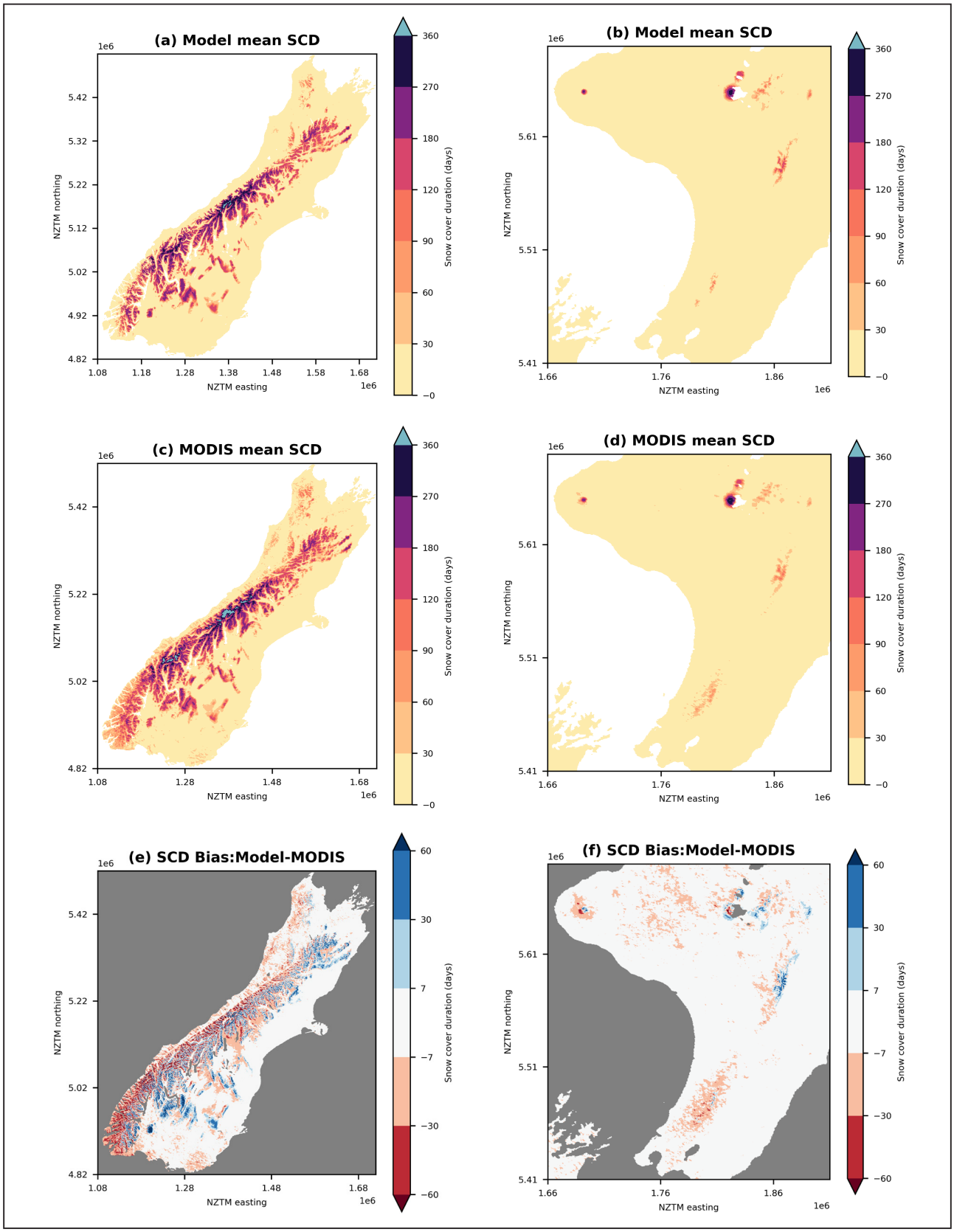

Figure 4: Comparison of simulated and observed annual mean SCD for the South and North Islands of NZ, for hydrological years 2017-18 to 2019-20.

Table 2: Snow cover duration statistics for Default and Sensitivity runs and for different SWE thresholds.

Model options	**SWE threshold** (mm w.e.)	**Mean SCD** *(all points weighted equally)* (days)	**Mean bias** (*all points weighted equally*) (days)	**MAE** (*all points weighted equally*) (days)	**SCD macro-averaged in 200m elevation bin** (days)	**Bias of SCD macro-averaged in 200m elevation bins** (days)
MODIS	-	21.7	-	-	200.4	-
Default run	30	15.0	-6.69	9.14	195.3	-5.1
	5	21.3	-0.32	9.18	205.2	4.8
Sensitivity run	30	10.2	-11.50	11.88	183.0	-17.4
	5	15.1	-6.60	9.04	192.7	-7.7

The average SCD bias across all points is 6.69 days with mean absolute error (MAE) < 10 days for default options (Table 2). To better understand the sensitivity of the results to model parameters and analysis threshold, the SCD was calculated using both 30 and 5 mm w.e. SWE thresholds for both Default (Tacc = 1 °C, Tmelt = 0 °C) and Sensitivity (Tacc = °0 C, Tmelt = -1 °C) runs. When a 5 mm w.e. threshold is used to define snow cover from the simulations, SCD increases and the mean bias is close to 0 days. The Sensitivity run with a 5 mm w.e. threshold shows very similar bias and error as the default settings, while the Sensitivity run with 30 mm w.e. threshold has much shorter snow cover than observations. Further discussion is made after elevational patterns of SCD are presented.

Closer inspection of a 30 km x 30 km domain reveals a pattern of ragged edges within MODIS SCD, while the model closely follows the contours of the topography (Figure 5). This pattern is an artefact of the reprojection from the sinusoidal grid that MOD10A1 is distributed on. Over New Zealand, the nominal 500m sinusoidal pixels are distorted into parallelograms with a diagonal of 2 km running ENE – WSW. When this distorted grid is resampled to a regular 250m grid with nearest neighbour to retain the integrity of the data, the MODIS

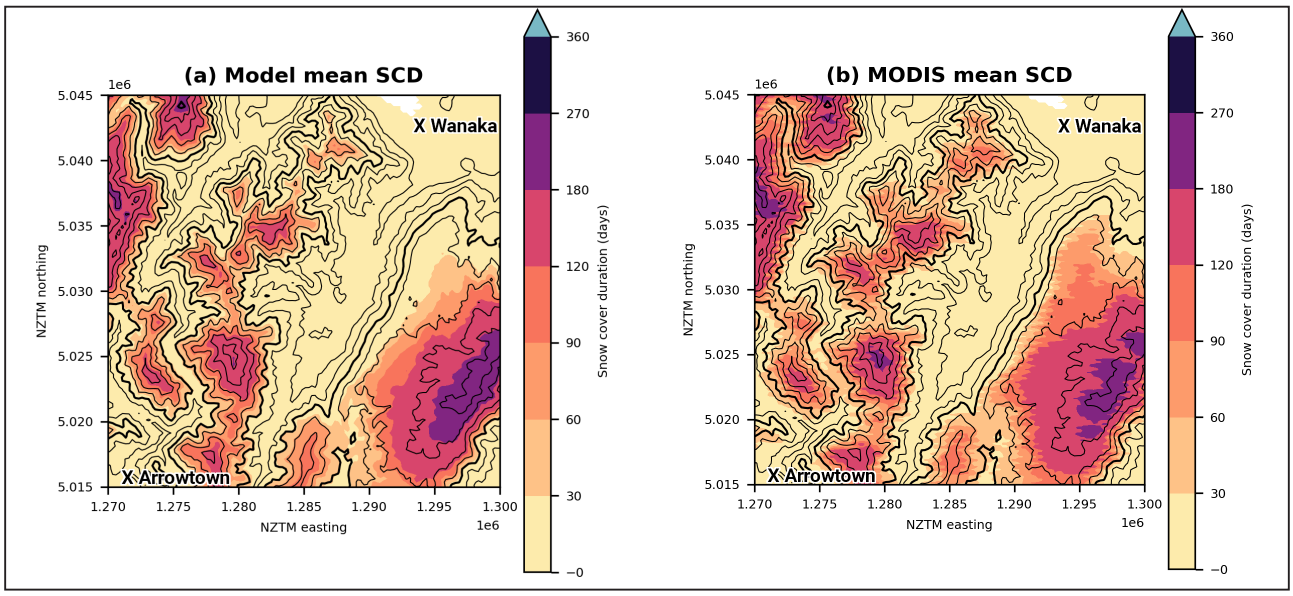

Figure 5: Detailed view of simulated and observed mean SCD for 30 km x 30 km domain centred on the Cardrona Valley for hydrological years 2017-18 to 2019-20. 200 m elevation contours are shown for reference, with 1000 m contour bolded.

data is smeared across elevation bands, principally in the longitudinal direction. In complex topography, this smearing results in signal from high-elevation areas with snow cover being smeared to lower elevations. Future work should look to process the MODIS data from swath direct to an NZTM grid to avoid such artefacts.

The relationship between elevation and SCD across the South Island shows the expected positive relationship in both the model and MODIS (Figure 6a, b). Under 800 m, < 30 days snow cover dominates in both model and MODIS (Figure 6a,b), with the model showing very little snowpack with longer SCD. The mode of MODIS SCD shows a non-linear relationship to elevation. From 1000 to 1400 m the SCD increases rapidly from < 30 days to > 120 days, then increases more slowly, reaching 210-240 days between 2000 and 2200 m. Above this, the mode of SCD jumps to > 360 days, indicative of areas of permanent snow. The mode of model SCD is consistent with the MODIS SCD mode in most bins, though has a more linear relationship to elevation, resulting in larger SCD simulated between 1800 and 2200 m. Figure 6c shows that, between 1000 and 1500 m, MODIS has a more pixels with SCD between 40 and 150 days, while the model has more pixels with no snow cover. Between 1500 and 2000 m, there is a broad range of SCD in MODIS that is well represented by the model, except for a tendency to underestimate the small area with the longest SCD. These points include areas with permanent snow and glaciers that show up in MODIS as a subtle peak in SCD > 360 days above 1600 m (Figure 6b). This feature is not seen in the model SCD as SWE is reset to 0 at the beginning of simulations (1 April), so permanent snow areas below 2200 m show up as SCD of 330 to 360 days (Figure 6a). Between 2000 and 2500 m, areas of permanent snow create a bi-modal distribution of SCD in MODIS observations, which is also apparent in the model distribution, albeit shifted to longer SCD (Figure 6c).

The sensitivity of the results is illustrated by the elevation profile of mean SCD. While a 5 mm threshold shows a smaller mean bias compared to the 30 mm threshold for the Default run (Table 2), this is only because it is closer to the MODIS observations over the large area of land below 1000 m elevation, while overestimating SCD at most elevations (Figure 6d). To give a better representation of the fit, the SCD bias can be macro averaged by elevation bins (i.e. by equally weighting mean bias over each 200 m elevation bin). When macro averaged, the two thresholds give similar results, with the 5 mm w.e. threshold showing a positive bias and the 30 mm w.e. threshold a negative bias (Table 2), in agreement with visual assessment of mean SCD in Figure 6d. The Sensitivity run with the 5 mm w.e. threshold shows a similar fit to the Default run, while Sensitivity run the 30 mm w.e. threshold produces average SCD that is much shorter than observations at all elevations (Figure 6d) and a large negative macro-averaged bias (Table 2). Aside from the changes in bias, the spatial patterns of SCD are similar in all model analyses (not shown). We note the purpose of this analysis is to illustrate the sensitivity of the results, rather than selecting a 'best' simulation. A better simulation of snow would be made using an ensemble snow model, once the model parameter space has been evaluated at sites where the meteorology and snowpack dynamics are well known. This would allow a more robust validation against observation and potential for assimilating snow covered area in the future.

In contrast to simulations using NZCSM as input, simulations using daily gridded climate observations as input show much shorter snow cover duration than MODIS observations, and large areas of negative bias across most of the areas with snow cover (Appendix A). While a thorough diagnosis of the reasons for poor model performance with gridded observations is beyond the scope of this paper, it is likely that both air temperature and precipitation biases along with model parameter errors lead to the underestimation of snowfall, and therefore to a reduced length of snow cover. In addition, the extra

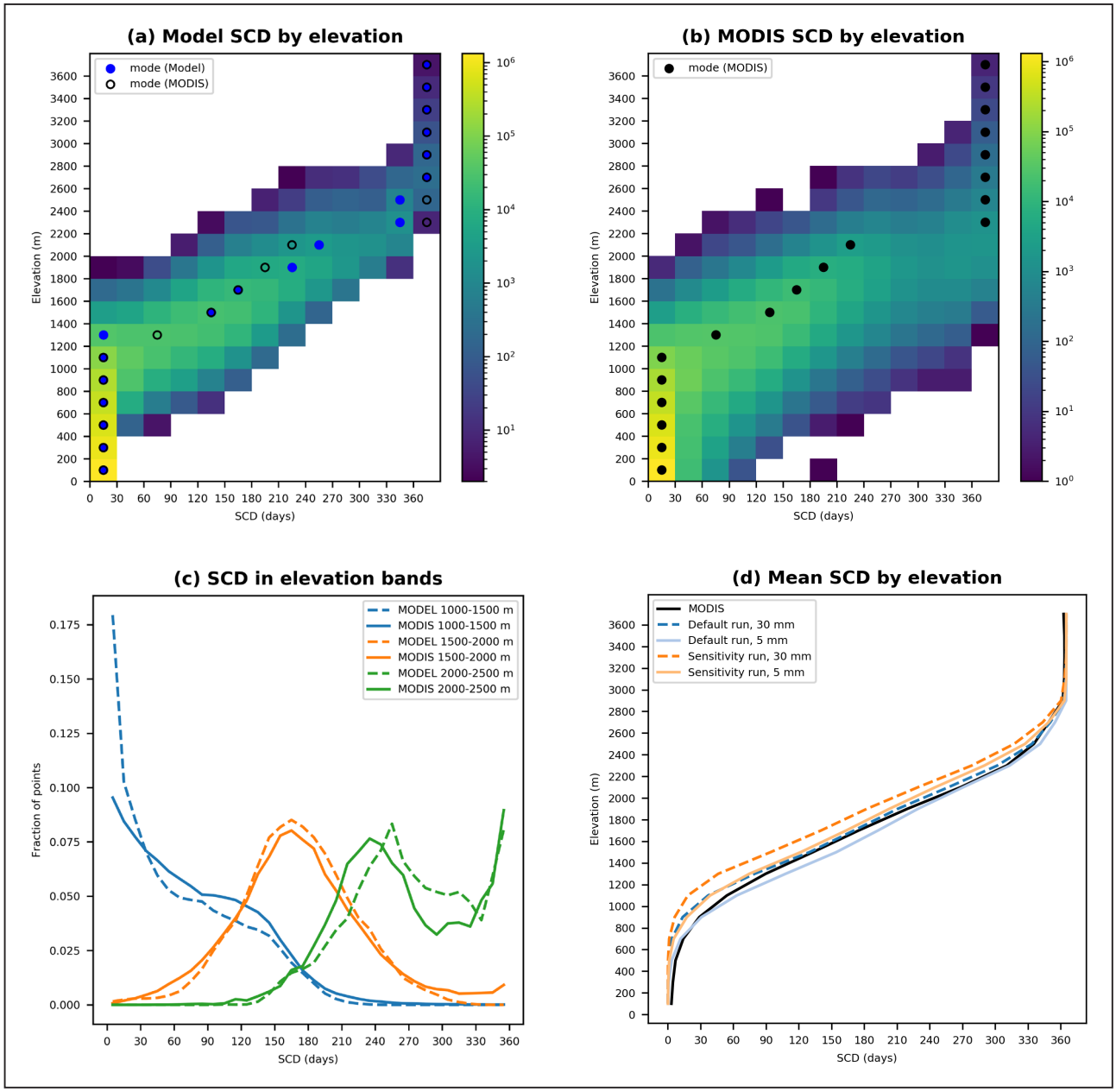

Figure 6: 2D histogram of (a) simulated (Default run) and (b) observed annual mean snow cover duration (SCD) for New Zealand in 200 m elevation bins and 30-day SCD bins. Note the log scale of bin frequency in panels (a) and (b). The mode for each elevation bin is shown as points. (c) simulated (Default run) and observed SCD distribution in 500 m elevation bins (d) mean SCD for Default and Sensitivity runs with 30 and 5 mm w.e. SWE thresholds.

step to convert the input data from daily to hourly will also introduce uncertainty. The poor performance of the model with daily gridded climate observations highlights the need for a thorough investigation of model parameter ranges and sensitivity at sites with observed meteorology and snow storage, to disentangle uncertainties in model parameters and climate input. While the snow model is sensitive to air temperature, it is encouraging that both the Default and Sensitivity run with NZCSM input are closer to the MODIS observations than those using gridded daily climate observations, giving confidence that the combination of snow model parameters and climate input are producing a more reasonable simulation of snow cover.

3.3 Seasonal evolution of snow covered area and snowpack water storage

Figure 7 shows the seasonal progression of snow covered area (SCA) across New Zealand. The time of peak SCA varies widely in both model and MODIS (from June through September) and depends on the occurrence of low-level snowfall events. During winter, the model SCA is very sensitive to the threshold used to define snow cover from SWE (compare Figure 7a and 7b), and this may contribute to the generally lower modelled values of SCA in winter. A low threshold of 5 mm w.e. produces similar snow covered area as MODIS in the early season, whereas the early season peaks in SCA are too low for a threshold of 30 mm w.e.. Through spring, the timing and rate of depletion of MODIS SCA is well captured by the model with most areas being snow free by the end of December, and the model SCA is less sensitive to the threshold chosen. While the extent of individual low-level snowfall events is not always captured by the model (e.g. July 2017-18), the occurrence of most significant accumulation events through each season are captured. The interannual variability is also well matched between the model and MODIS, with 2017-18 having lower SCA early and later in the season, 2018-19 peaking earlier than other years, and 2019-20 peaking later and remaining higher later into the spring and summer.

We present snow storage values here to compare with previous studies but also to highlight the sensitivity to model settings and provide some insights into the relationship between simulated snow cover and storage. The simulated snow storage (Figure 8) shows a smoother increase and decrease through the season than SCA. In the default simulation, storage increases throughout winter to peak around 1 September at 14 to 15 km^3 w.e.. The Sensitivity run shows a very similar pattern, but with peak of storage around 9 km^3 w.e.. For context, the long-term average monthly total rainfall for the South Island is 25 to 30 km^3 (Henderson et al., 2011), so the peak storage simulated here approaches half one months total precipitation. The total seasonal snow storage is much smaller than the total stored in glaciers (42.1 km^3 +/- 8.4 km^3 w.e. in 2019; Carrivick et al., 2020), but large compared the annual mass changes (+1.2 to -3.4 km^3 w.e.; Salinger et al., 2019) over the last few decades.

Published estimates of the total seasonal snow storage are scarce and show a large variation in magnitude. Fitzharris and Garr (1995) provided an early estimate of peak total

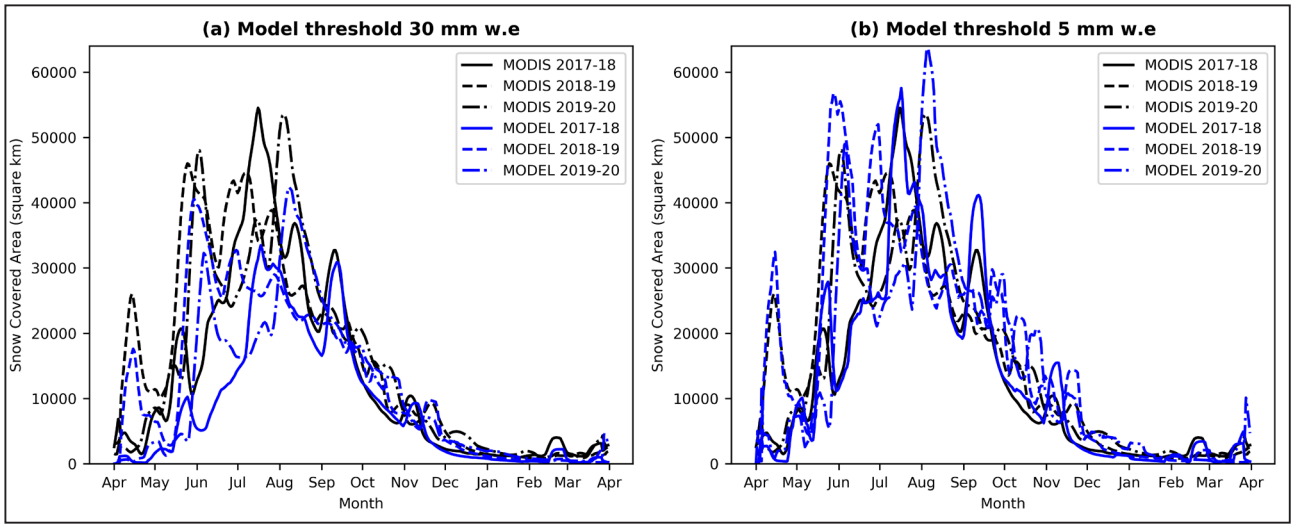

Figure 7: Seasonal progression of simulated and observed SCA across New Zealand using different SWE thresholds for classifying modelled grid points as snow covered. Both timeseries are smoothed with 11-day rolling mean.

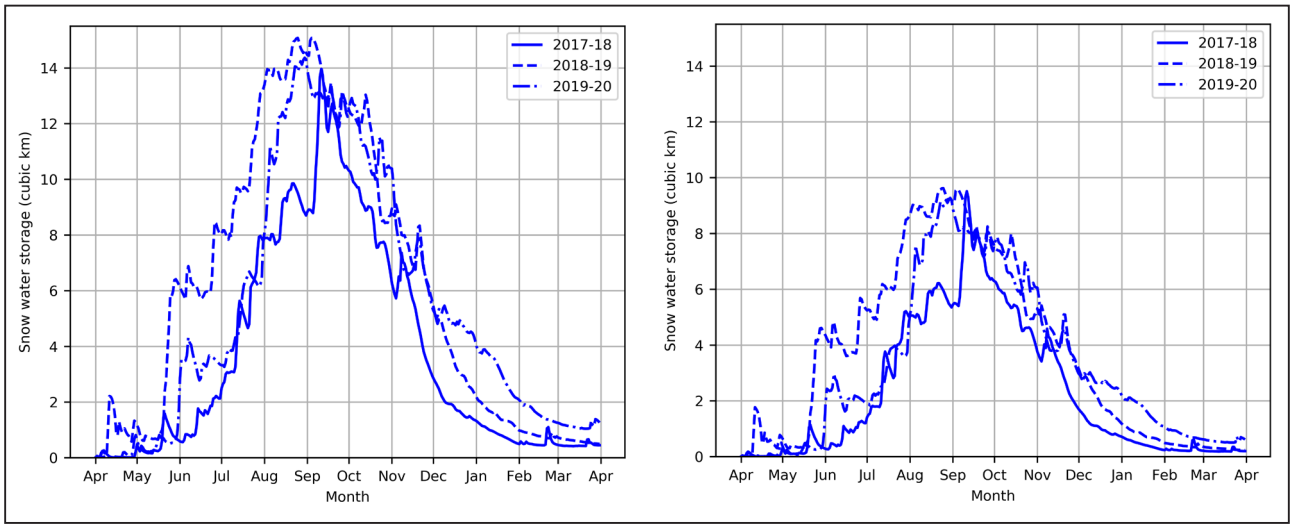

Figure 8: Progression of simulated seasonal snow water storage across New Zealand for (a) Default run, and (b) Sensitivity run.

snow storage for the major hydroelectric catchments from Manapouri to Tekapo at around 6 km³ w.e. during October. The NZ water accounts (Henderson et al., 2011) estimate year-to-year changes in snow storage across New Zealand on 1 July of -4 to +2 km³ w.e., which is similar to the differences in 1st July values presented here. The tables associated with the most recent NZ water accounts (Griffiths et al., 2021) estimate mean total snow storage increases by 9.5 +/- 2.9 km³ w.e between 1 April and 30 September, though we note that some melt of permanent snow will be included in these values. The mean value of AMJ storage change (5.1 +/- 2.1 km³ w.e.) in the NZ water accounts is half that first reported by Fitzharris (2004) who put total snow storage on 1 July at 10.8 +/- 3.2 km³ (mean value between 1994-95 and 2000-01) for the South Island only. NZ Water Accounts storage values on 1 September for the years presented here are 7.8, 7.7 and 8.3 km³ w.e., respectively, with less accumulation occurring during April, May, June (AMJ) (mean of 3.3 km³ w.e.) than July, August, September (JAS) (mean of 4.7 km³ w.e.). The smaller values obtained from the Sensitivity run are more congruent with the NZ water accounts numbers, while the Default run is closer to the values in Fitzharris et al. (2004). Given the general overestimation of precipitation by NZCSM across areas to the east of the main divide, the values simulated with NZCSM input are likely to be an overestimate, but will depend on (i) how this is balanced by underestimated precipitation in western areas and (ii) to what extent model parameter uncertainty is compensating for input data biases, given the good fit of SCD. Given the similar fit of Default and Sensitivity runs to MODIS SCD (for a range of plausible SWE thresholds), further data beyond MODIS observations should be used as validation of future simulations of snow storage (e.g. satellite snow depth, *in-situ* SWE measurements). More detailed analysis of snow cover and snow storage in major catchments is possible using these results but is beyond the scope of paper.

Total storage depletes rapidly through spring, indicating widespread melt, then slows through summer, particularly in 2019-20 where significant snowfall in December prolonged the storage of snow through summer. To investigate this further the total simulated storage in different elevation bands within the South Island is shown for each month through spring (Figure 9). The slowing rate of total melt during summer in the model is a function of the increase in the average elevation of the remaining snowpack. At the start of spring, most storage lies between 1200 and 2400 m elevation, with the mode around 1600 m. This pattern is caused by the interaction of increasing snow storage and decreasing land area

with elevation. Only 0.75% of land in the South Island (~1100 km²) is > 2000 m elevation, and only 0.05% (~70 km²) is > 2500 m. Through spring the average elevation of the storage increases as lower elevation snow melts and higher elevations continue to accumulate snow (e.g. compare 1 Sept and 1 Oct at 1400-1600 m and 1800-2000 m). By 1 December the average elevation of storage lies around 2000 m, and most storage below 1600 m is depleted within the model.

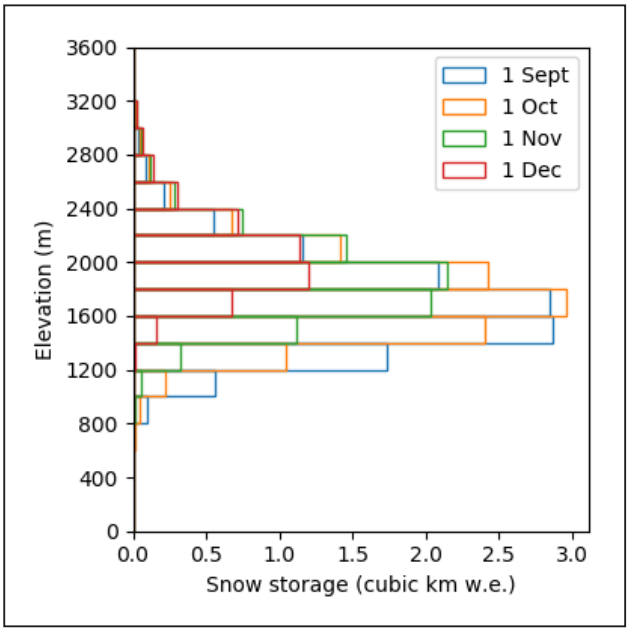

Figure 9: Progression of total simulated snow storage for the South Island during spring in 200 m elevation bins. Data are averages from the three years.

4. Limitations and directions for future research

This work has many limitations that centre on the accumulation of uncertainties from each step in the model process. Firstly, it is apparent the NZCSM fields used as input meteorology contain systematic biases that would ideally be bias-corrected before snow simulations were performed. The fact that the model shows a good fit to the observed snow cover duration dynamics suggests that snow model parameters may be acting to counter or mask the biases in NZCSM input. Future research should work to separate the uncertainties in snow model parameters and input data. Validation of precipitation in alpine areas continues to be problematic as direct validation of winter precipitation is limited to 3 sites with solid precipitation measurements and large spatial and temporal variability. Additional rainfall sites at low elevations within mountainous areas that are not in the National Climate Database may be useful for further validation.

Secondly, the snow model is a relatively simple model that reduces the many physical processes controlling the rate of snow accumulation and melt into a few tuneable parameters. Here we use a limited range of parameters, but future work should look to assess the range of appropriate model parameters using independent datasets such as meteorological and snow information from high-altitude weather stations (e.g. Porhemmat et al, 2020; 2021). A thorough assessment of the model parameters should also assess parameter transferability between sites and include comparison to more sophisticated snow models to diagnose what processes may be responsible for poor model performance. A better understanding of parameter ranges will aid in assessing the reliability of simulations with different input data in areas without climate observations. Snow simulations at SIN sites could also be used as validation of NZCSM precipitation if observed air temperature is used as model input and model parameters are properly constrained. These point simulations would also be useful in assessing snow storage estimates using NZCSM input. Ensemble model techniques may also be useful in capturing uncertainty (in e.g. catchment average snowpack storage) and enabling assimilation of satellite derived snow information (e.g. Alonso-González et al. 2021). Model parameters will need to be more tightly constrained to avoid compensating for input biases when assimilating.

Thirdly, the comparison of simulated SWE to MODIS NDSI involves transfer functions that are largely unknown.

These functions can introduce large uncertainty at times, e.g. the sensitivity of simulated SCA to the SWE threshold during winter. While we know that MODIS does detect fractional snow cover within a pixel, the model has no explicit or implicit fractional snow cover, and the effect of a simulated fractional snow cover on the comparison to MODIS has not been assessed. Future work should look to resolve the relationship between snow depth, SWE, SCA and MODIS NDSI using more sophisticated snow models and new remote sensing products (e.g. Deschamps-Berger et al., 2020) that enable snow depth to be retrieved at finer spatial scales. This work could include directly simulating fractional snow cover area using sub-grid snow depth parameterisations (e.g. Clark et al, 2011) to compare to MODIS fractional snow cover area (Alonso-González et al. 2021). Future simulations may also benefit from explicit simulation of 2D snow processes such as mass transport by wind (preferential deposition and redistribution) and gravity (avalanches).

Perhaps the most significant limitation of this work is the short length of the simulations. The observed variability of SCA over the 20-year MODIS record is much greater than that over our 3-year study period[2]. Therefore, we would expect much greater variation in the timing and magnitude of snow cover and snow storage over longer simulations. When improved gridded near-surface meteorological products such as high-resolution reanalysis datasets are available, longer model simulations in concert with direct analysis of MODIS snow cover (e.g. Redpath et al., 2019) will enable a much greater understanding of interannual variability and trends in seasonal snow cover. Alternatively, efforts to improve gridded observational products such as VCSN may improve the ability to use these products for reliable simulation. Improvements being investigated include higher spatial and temporal resolutions (500 m and hourly, respectively), better mean rainfall surfaces for interpolation, and/or the inclusion of data from rain gauges outside the National Climate Database (i.e. from regional councils and other providers).

5. Conclusions

While three years of simulation are insufficient for an authoritative climatology, they can inform future work to improve the estimation of seasonal snow at national scale by allowing a first detailed analysis of snow cover duration patterns in relation to remote sensing snow cover and estimate of the seasonal cycle of total storage of water within New Zealand's seasonal snowpack. While surface meteorology fields from NZCSM forecasts are generally colder and wetter than observations, we find them a reasonable input for simulating seasonal snow with simple snow model at national scale, particularly in comparison to simulations using gridded daily climate observations as input. The interannual variability in seasonal snow covered area patterns is captured by the NZCSM meteorology, including the most significant snowfalls in each season, thus, NZCSM output could be used to develop near-real time or forecasted state of the snowpack solutions. Biases against MODIS SCD are found in some areas, particularly to east of main divide where modelled snow cover persists longer than observed, likely due to the general wet bias in the NZCSM total precipitation east of the main divide. On average, we find a good fit to MODIS SCD with elevation, though the model is more tightly constrained to elevation. Between 1000-2000m, the model shows a correct pattern of SCD, except for a tendency to underestimate the longest duration snow cover. At lower elevations, the model has a greater proportion of grid points with very short SCD compared to MODIS. This underestimation of MODIS SCD at lower elevations could stem from model errors or from artefacts of the MODIS snow cover processing for New Zealand. It is likely that model parameters are compensating for biases in NZCSM and exacerbating potential biases in gridded observed climate data, but it is difficult to disentangle input data and model parameters uncertainty using MODIS observations at this scale. The model SCD and SCA is very sensitive to SWE threshold within the winter accumulation season, and caution is

[2] *https://www.otago.ac.nz/surveying/potree/pub/mrc/projects/snotago/modis-snow-cover; retrieved 5 Aug 2021.*

warranted when validating snow storage estimates solely on MODIS observations. Nonetheless, the simulations provide a useful view of the patterns of snow cover across New Zealand as well as highlighting the need for more nuanced use of MODIS observations and alternate remotely sensed products to directly validate and/or derive appropriate relationships between MODIS observations and model simulations.

Over the three years of simulations, the peak seasonal snow storage occurs around 1 September, following the period of peak snow covered area, which varies between June and September. While substantial uncertainty still exists, the estimated total seasonal snow storage is a similar order of magnitude as half the long-term average monthly total rainfall for the South Island. Longer simulations are likely to reveal substantial interannual variability in this storage, based on the observed variability of MODIS SCA over the last 20 years.

Future work should look to independently address uncertainties in meteorological input data, snow model parameters (including accumulation, melt and sub-grid snow processes), and relationships between snow depth, SWE, SCA and MODIS NDSI to inform future estimates of snow cover and water storage. Alongside this, efforts to evaluate ensemble modelling efforts and assimilation of remotely sensed snow information will lead to more reliable estimates of snow storage and melt across New Zealand, which will benefit end users interested in future mountain climate, snow hazards and streamflow from alpine areas.

Acknowledgements

This research was funded by NIWA under the Resilience to Hazards Research Programme SSIF (2019/20 and 2020/21). The authors wish to acknowledge the contribution of NeSI to the results of this research. New Zealand's national compute and analytics services are supported by the New Zealand eScience Infrastructure (NeSI) and funded jointly by NeSI's collaborator institutions and through the Ministry of Business, Innovation and Employment. URL http://www.nesi.org.nz. Snow model output is available for further analysis on request. The authors thank the editor and two anonymous reviewers whose comments greatly improved the manuscript.

Appendix A: Snow simulations using gridded observations as input

As a comparison to simulations using NZCSM meteorology as input, further simulations were performed for the South Island domain using Virtual Climate Station Network (VCSN) data as input. The methods used were identical to the NZCSM simulations, with the addition step to transform the daily VCSN data to hourly fields. This was undertaken following Clark et al. (2009) with hourly air temperature obtained by fitting a sine function to daily minimum and maximum air temperature and hourly precipitation created from daily total precipitation using random cascade method.

Maps for snow cover duration (SCD) show that the VSCN simulations produce much shorter duration snow cover than observed (Figure A1, A2). As with the NZCSM input, the results depend on the SWE threshold chosen, but the smaller SWE threshold (5 mm w.e.) does not resolve the issue that not enough snow accumulates at most elevations, particularly moderate elevations (1000 to 2000 m) and areas in the east (Figures A3, A4). A timeseries of snow-covered area (Figure A5) shows some low-level snowfalls in the VCSN simulations, but the total area is much lower than observed. While a thorough diagnosis of the reasons for poor model performance is beyond the scope of this paper, it is likely that both air temperature and precipitation biases along with snow model parameter errors lead to the underestimation of snowfall and therefore to a reduced length of snow cover. The extra step to convert the input data from daily to hourly will also introduce uncertainty.

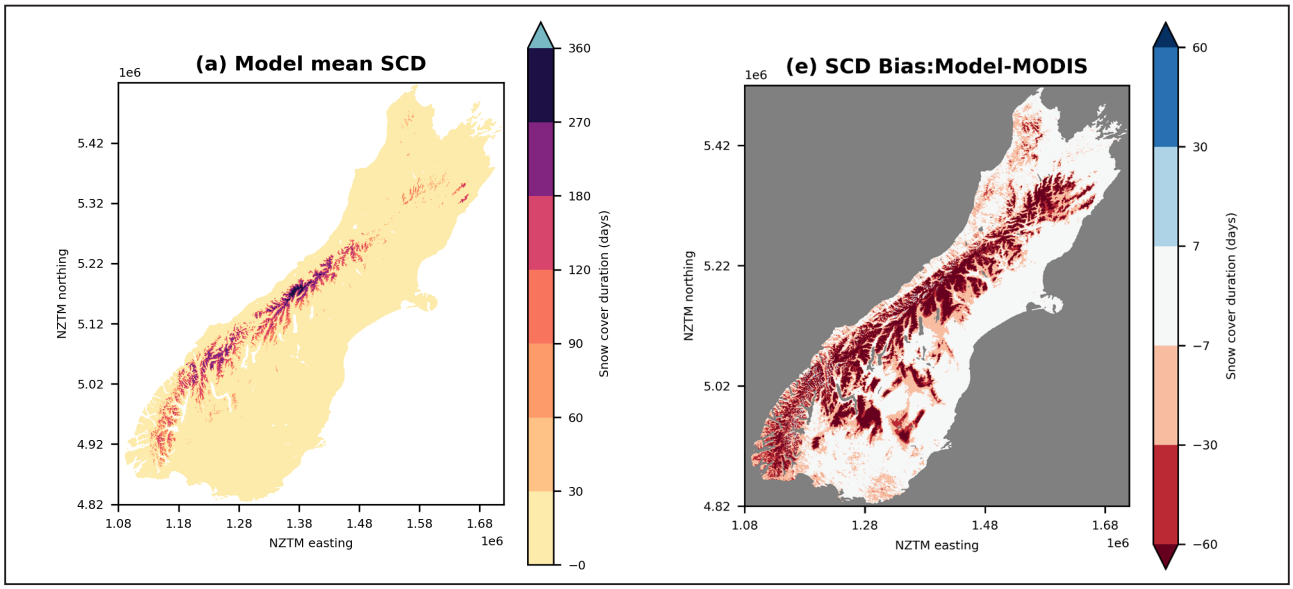

Figure A1: As for Figure 4a, e but for simulations using VCSN as input (30 mm SWE threshold).

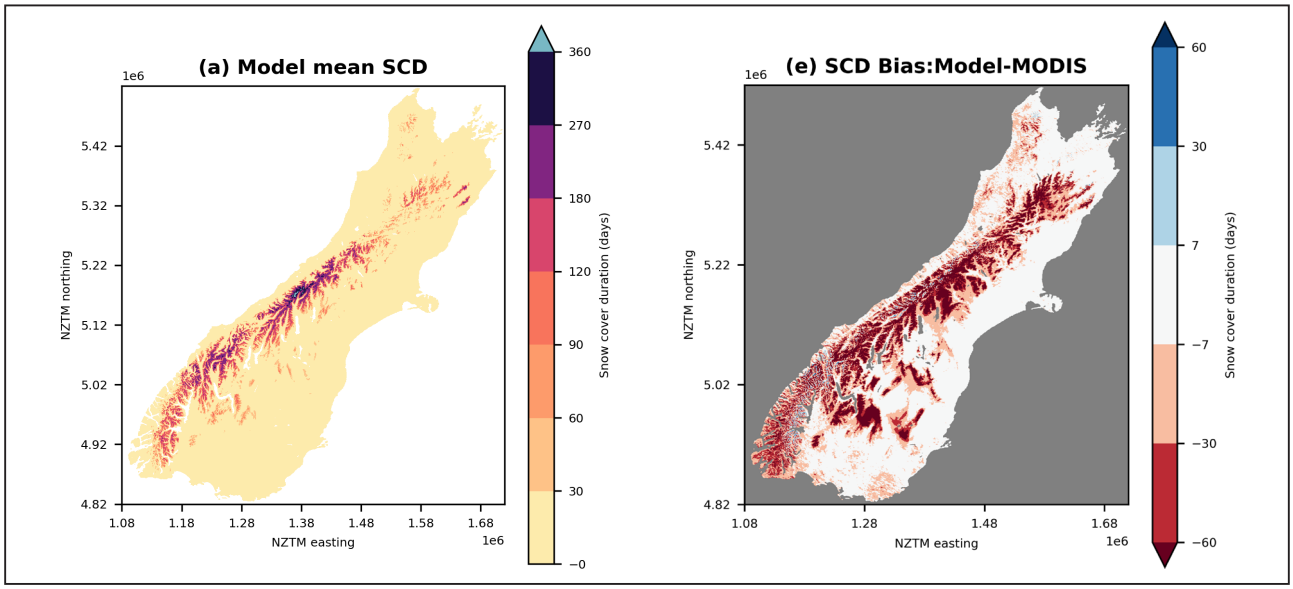

Figure A2: As for Figure A1 but for 5 mm SWE threshold.

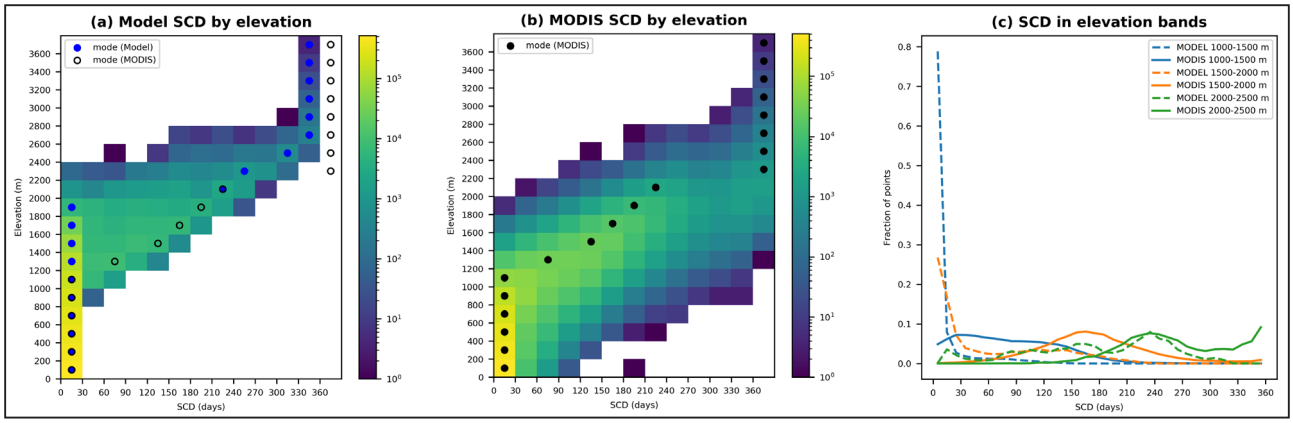

Figure A3: As for Figure 6 but for South Island simulations using VCSN as input (30 mm w.e. threshold).

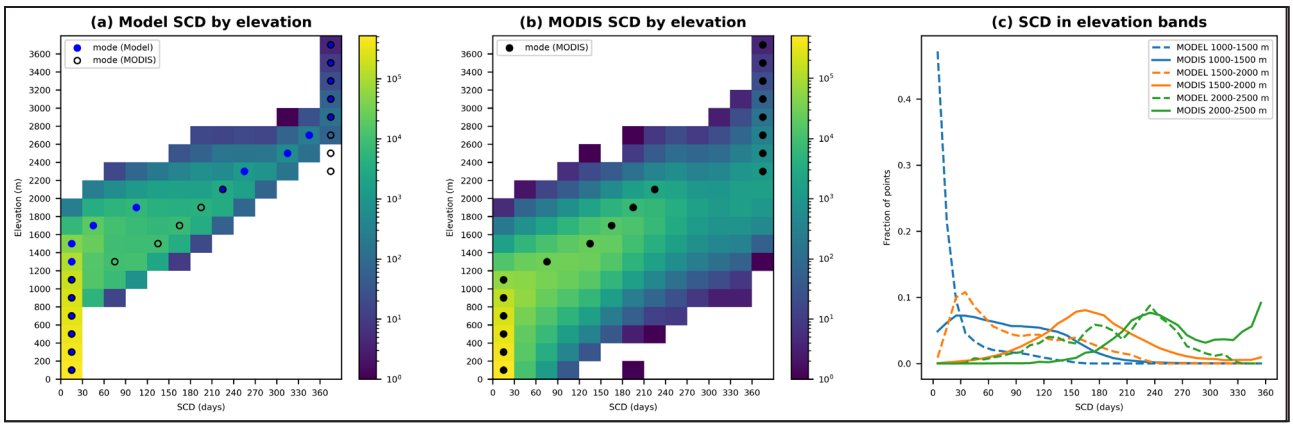

Figure A4: As for Figure A3 but 5 mm w.e. threshold.

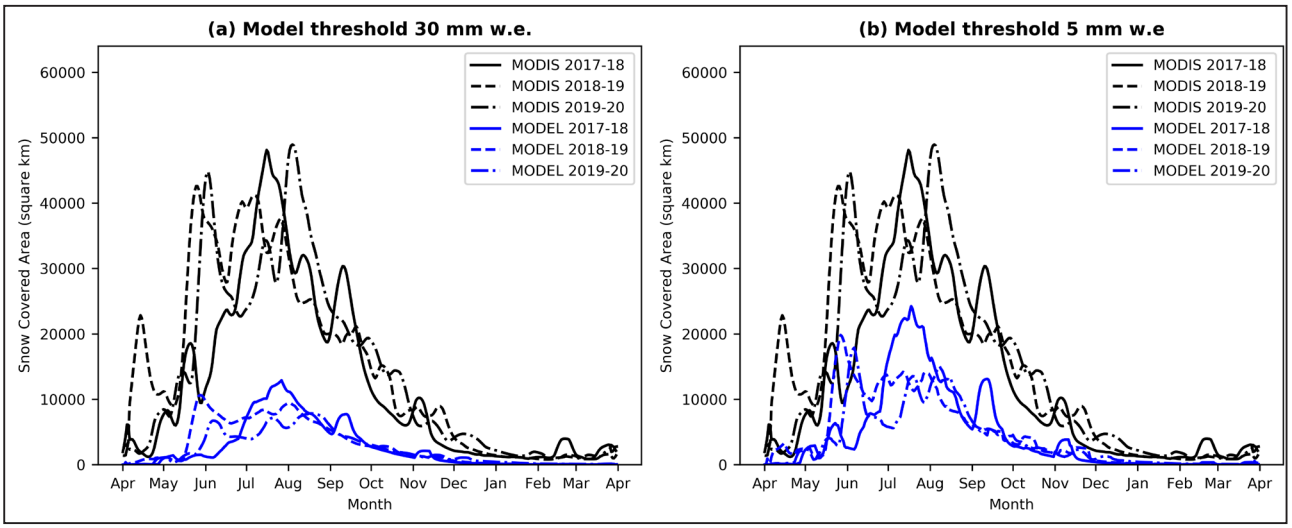

Figure A5: As for Figure 5 for South Island simulations using VCSN as input.

References

Alonso-González, E., Gutmann, E., Aalstad, K., Fayad, A., Bouchet, M. and coauthors 2021. Snowpack dynamics in the Lebanese mountains from quasi-dynamically downscaled ERA5 reanalysis updated by assimilating remotely sensed fractional snow-covered area. Hydrology and Earth System Sciences, 25, 4455-4471.

Anderson, B., Mackintosh, A. N., Dadić, R., Oerlemans, J., Zammit, C. and coauthors 2021. Modelled response of debris-covered and lake-calving glaciers to climate change, Kā Tiritiri o te Moana/Southern Alps, New Zealand. Global and Planetary Change, 205.

Blacutt, L.A.; Herdies, D.L.; de Gonçalves, L.G.G.; Vila, D.A.; Andrade, M. 2015: Precipitation comparison for the CFSR, MERRA, TRMM3B42 and Combined Scheme datasets in Bolivia. Atmospheric Research, 163: 117-131

Carrivick, J. L., James, W. H. M., Grimes, M., Sutherland, J. L. & Lorrey, A. M. 2020. Ice thickness and volume changes across the Southern Alps, New Zealand, from the little ice age to present. Scientific Reports, 10, 13392.

Cattoën, C., McMillan, H. & Moore, S. 2016. Coupling a high-resolution weather model with a hydrological model for flood forecasting in New Zealand. Journal of Hydrology (NZ), 55, 1-23

Clark, M., Hreinsson, E., Martinez, G., Tait, A., Slater, A. G. and coauthors 2009. Simulations of seasonal snow for the South Island, New Zealand. Journal of Hydrology (NZ), 48, 41-58.

Clark, M. P., Hendrikx, J., Slater, A. G., Kavetski, D., Anderson, B. and coauthors 2011. Representing spatial variability of snow water equivalent in hydrologic and land-surface models: A review. Water Resources Research, 47, 1-23.

Conway, J. P. & Cullen, N. J. 2016. Cloud effects on surface energy

and mass balance in the ablation area of Brewster Glacier, New Zealand. The Cryosphere, 10, 313-328.

Deschamps-Berger, C., Gascoin, S., Berthier, E., Deems, J., Gutmann, E. and coauthors 2020. Snow depth mapping from stereo satellite imagery in mountainous terrain: evaluation using airborne laser-scanning data. The Cryosphere, 14, 2925-2940.

Dozier, J., Painter, T. H., Rittger, K. & Frew, J. E. 2008. Time-space continuity of daily maps of fractional snow cover and albedo from MODIS. Advances in Water Resources, 31(11), 1515-1526.

Fitzharris, B. & Garr, C. E. 1995. Simulation of past variability in seasonal snow in New Zealand. Annals of Glaciology, 22.

Gascoin, S., Hagolle, O., Huc, M., Jarlan, L., Dejoux, J. F. and coauthors 2015. A snow cover climatology for the Pyrenees from MODIS snow products. Hydrology and Earth System Sciences, 19, 2337-2351.

Griffiths, J, Zammit, C, Wilkins, M, Henderson, R, Singh, S, Lorrey, A, Shankar, U, Vargo, L, Anderson, B, & Purdie, H 2021. New Zealand water accounts: Update 2020. NIWA report prepared for Stats NZ Tatauranga Aotearoa. Retrieved from www.stats.govt.nz.

Hall, D. K. & Riggs, G. A. 2007. Accuracy assessment of the MODIS snow products. Hydrological Processes, 21, 1534-1547.

Hall, D. K. & Riggs, G. A. 2016. MODIS/Terra Snow Cover Daily L3 Global 500m SIN Grid, Version 6. Boulder, Colorado USA. NASA National Snow and Ice Data Center Distributed Active Archive Center.

Harder, P. & Pomeroy, J. 2013. Estimating precipitation phase using a psychrometric energy balance method. Hydrological Processes, 27, 1901-1914.

Henderson, R. D., Woods, R., Singh, S. & Zammit, C. 2011. Surface water components of New Zealand's National Water Accounts, 1995-2010. Christchurch: NIWA.

Hendrikx, J. & Harper, A. 2013. Development of a National Snow and Ice Monitoring Network for New Zealand. Journal of Hydrology (NZ), 52.

Hendrikx, J., Hreinsson, E. Ö., Clark, M. P. & Mullan, A. B. 2012. The potential impact of climate change on seasonal snow in New Zealand: part I—an analysis using 12 GCMs. Theoretical and Applied Climatology, 110, 607-618.

Kerr, T. 2013. The contribution of snowmelt to the rivers of the South Island, New Zealand. Journal of Hydrology (NZ), 52, 61-82.

Kerr, T., Clark, M., Hendrikx, J. & Anderson, B. 2013. Snow distribution in a steep mid-latitude alpine catchment. Advances in Water Resources, 55, 17-24.

Lundquist, J., Hughes, M., Gutmann, E. & Kapnick, S. 2019. Our Skill in Modeling Mountain Rain and Snow is Bypassing the Skill of Our Observational Networks. Bulletin of the American Meteorological Society, 100, 2473-2490.

Norton, D. A. 1985. A multivariate technique for estimating New Zealand temperature normals. Weather & Climate, 5, 64-74.

Porhemmat, R., et al. 2020. The influence of atmospheric circulation patterns during large snowfall events in New Zealand's Southern Alps. International Journal of Climatology 41: 2397-2417.

Porhemmat, R., et al. 2021. Moisture transport during large snowfall events in the New Zealand Southern Alps: The role of Atmospheric Rivers. Journal of Hydrometeorology 22: 425-444

Quéno, L., Vionnet, V., Dombrowski-Etchevers, I., Lafaysse, M., Dumont, M. and coauthors 2016. Snowpack modelling in the Pyrenees driven by kilometric-resolution meteorological forecasts. The Cryosphere, 10, 1571-1589.

Redpath, T. A. N., Sirguey, P., & Cullen, N. J. 2019. Characterising spatio-temporal variability in seasonal snow cover at a regional scale from MODIS data: the Clutha Catchment, New Zealand. Hydrology and Earth System Sciences, 23, 3189-3217.

Salinger, M. J., Fitzharris, B. B. & Chinn, T. 2019. Atmospheric circulation and ice volume changes for the small and medium glaciers of New Zealand's Southern Alps mountain range 1977–2018. International Journal of Climatology, 39, 4274-4287.

Sirguey, P., Mathieu, R. & Arnaud, Y. 2009. Subpixel monitoring of the seasonal snow cover with MODIS at 250 m spatial resolution in the Southern Alps of New Zealand: Methodology and accuracy assessment. Remote Sensing of Environment, 113, 160-181.

Tait, A. & Macara, G. 2014. Evaluation of interpolated daily temperature data for high elevation areas in New Zealand. Weather and Climate, 34, 36-49.

Tait, A., Sturman, J. & Clark, M. 2012. An assessment of the accuracy of interpolated daily rainfall for New Zealand. Journal of Hydrology (NZ), 51, 25-44.